

## ABSTRACT

CHEN, KE. Middle Atlantic Bight Shelfbreak Circulation Dynamics and Biophysical Interactions. (Under the direction of Dr. Ruoying He).

The Middle Atlantic Bight (MAB) shelfbreak is a quite dynamic region off northeast US coast. The shelfbreak front and jet controls the coastal transport and exchange of water mass, nutrient and carbon which are key components of coastal environment and ecosystem. The shelfbreak region is also famous for its high productivity, which is known as “shelfbreak enhancement”. Using state-of-art numerical models, this study extensively investigated the physical and biological characteristics of the shelfbreak front and jet.

A high resolution ocean circulation model is first constructed to investigate the circulation dynamics at the MAB shelfbreak. On average, the shelfbreak jet is about 40km wide and 100m deep, transporting ca. 0.4 Sv equator ward. It is found that the shelfbreak jet and boundary convergence reach their maximum intensities in the spring, at which time the foot of the front also migrates to its farthest offshore position. The dominant mode of shelfbreak circulation is the strong shelfbreak jet while offshore eddies also play an important role in modulating the shelfbreak circulation dynamics. The cross-shore transport at the MAB shelfbreak region is characterized by small means and large standard deviations, indicating the intermittent feature of shelf/slope exchange process.

A multi-nutrient, size-structured ecosystem model is then coupled with the high resolution ocean circulation model to investigate the physical and biogeochemical processes at the MAB shelfbreak. It is found that the domain-wide upper water column nutrient content peaks in late winter-early spring. The phytoplankton spring bloom starts 1–2 months later, followed by a zooplankton bloom in early summer. Seasonal and interannual variability in hindcast shelfbreak nutrient supply is controlled by three processes: (1) local mixing that deepens the mixed layer and injects deep ocean nutrients into the upper water column; (2) alongshore nutrient transport by the shelfbreak jet and associated currents; and (3) nutrient upwelling associated with shelfbreak bottom boundary layer convergence.

Incremental Strong-constraint 4-dimensional Variational (IS4DVAR) data assimilation technique is further applied to explore the impact of Gulf Stream Warm Core Ring (WCR) on the MAB shelfbreak and shelf circulation and related shelf/slope exchange process. The model assimilates satellite observed sea surface height and sea surface temperature, in-situ temperature and salinity profiles from expendable bathythermograph, Argo floats, CTD stations and glider transects. Two-month continuous assimilation experiment is performed over April-May 2006, with the focus on the great WCR, which is one of the largest in recent history. Data assimilation significantly improves model skill in both observational space and remote areas.

It is found the great WCR significantly changed the circulation in MAB continental slope and shelf. The mean cross-shelf transport induced by the WCR is estimated at 0.28 Sv offshore, and balances the mean along-shelf transport by the shelfbreak jet. Instantaneous streamer transport is up to 2.1 Sv, suggesting dramatic shelf/slope exchange. During the first week of May 2006, when the WCR was impinging upon the shelfbreak, large heat/salt flux with peak value of  $-8900 \text{ Watt m}^{-2} / -4 \times 10^{-4} \text{ Kg m}^{-2} \text{ s}^{-1}$ , which are 6-9 times larger than the mean value, is observed, indicating significant entrainment of cold/fresh shelf water by the WCR.

© Copyright 2011 by Ke Chen

All Rights Reserved

Middle Atlantic Bight Shelfbreak Circulation Dynamics and Biophysical Interactions

by  
Ke Chen

A dissertation submitted to the Graduate Faculty of  
North Carolina State University  
in partial fulfillment of the  
requirements for the Degree of  
Doctor of Philosophy

Marine Science

Raleigh, North Carolina

2011

APPROVED BY:

---

Gerald Janowitz

---

Daniel Kamykowski

---

Ping-Tung Shaw

---

Glen Gawarkiewicz

---

Ruoying He  
Chair of Advisory Committee/Advisor

## **BIOGRAPHY**

Ke Chen was born and raised in Qingdao, a very beautiful coastal city in China. The memories of the ocean since his childhood led his fascination with oceanography. Upon graduation from Chengyang No.1 high school in 2001, he went to Ocean University of China and enrolled in a competitive program specialized in marine science. Three years into this special program, Ke got his Bachelor of Science degree in marine science and was recommended to graduate study in physical oceanography. In graduate school, Ke joined Dr. Dexing Wu's group and worked on the interannual variability of the Pacific Ocean and its role in climate change. Three-year's study in the graduate program had trained Ke with knowledge of oceanography and practical programming skills. The experience of several laboratory experiments and cruises also increased his interest being an oceanographer. After he earned Master of Science degree in 2007, Ke pursued his PhD study at North Carolina State University under the advisement of Dr. Ruoying He. At NC State, Ke developed strong interests in coastal oceanography as well as numerical modeling techniques. Ke's doctoral research focused on the ocean circulation and biophysical interactions at the Middle Atlantic Bight shelfbreak frontal region. Using latest numerical model and data-assimilation techniques, Ke's research expands the understanding of this important coastal system.

## ACKNOWLEDGEMENTS

I express my sincerest gratitude to everyone who has made this work possible. First of all, I am indebted to my advisor, Dr. Ruoying He, for his guidance and support throughout my time at NC State. His enthusiasm and conscientiousness to science deeply impressed me and his encouragement and understanding greatly helped my work and life. He took me as a student and treated me as a friend. From him, I learned not only academic knowledge but also the attitude being a scientist and a noble person. Being the first PhD student of him, I would say it is very fortunate having Ruoying as advisor and also a friend.

I would like to express my sincere appreciation to Dr. Glen Gawarkiewicz, for his support and thoughtful advice on my research. I benefited a lot from his inspiring inputs and his kindness and generosity always make it a pleasure talking with him. I would also thank my other advisory committee members, Dr. Jerry Janowitz, Dr. Dan Kamykowski and Dr. Ping-Tung Shaw, for their helpful comments and constant support to my research. The classes I took from them also greatly expanded my knowledge and make my thinking of the ocean more comprehensive.

I am very grateful to Dr. Andrew Moore, Dr. Hernan Arango and Dr. Brian Powell for leading me in the study of 4DVAR data assimilation. Brian's kind help and brilliant ideas greatly improved my understanding and promoted my research progress.

I would also thank other faculty members at NC State, including Dr. Dave DeMaster, Dr. Paul Liu and Dr. William Showers, from whose lectures I learned much multi-disciplinary knowledge of marine science.

I am grateful to all people (past and present) in the MEAS department for providing such a good environment for my study. Particularly, I want to thank folks (past and present) in our group: Dr. Mingkui Li, Dr. Yue Wang, Dr. Kyun Hoon Hyun, Dr. Zuo Xue, Travis Miles, Joseph Zambon, Yizhen Li, Hui Qian, Jill Nelson, Yanlin Gong, Zhigang Yao and Yao Zhao. The time spent with you all makes my work at NC State joyful.

I also want to thank all my friends at NC State, for all the good time we had. I also thank Carmichael Gym and several workout buddies there. Spending one hour with you every day is fun and beneficial and it had become part of my daily routine.

Finally, my special gratitude goes to my family. Thanks to my parents Zhengmin Chen and Sujuan Cao for your unfailing love, support and encouragement through every step of my progress. Thanks to my wife Jie Zhang for your accompanying, understanding and sacrifice. With you, my life is delightful!

## TABLE OF CONTENTS

LIST OF TABLES.....	ix
LIST OF FIGURES.....	x
CHAPTER 1: INTRODUCTION.....	1
1. Hydrography and General Circulation.....	2
2. Shelfbreak System .....	4
3. Research Motivations and Objectives.....	10
4. Dissertations outline.....	12
References .....	14
CHAPTER 2: NUMERICAL INVESTIGATION OF THE MIDDLE ATLANTIC BIGHT SHELFBREAK FRONTAL CIRCULATION USING A HIGH-RESOLUTION OCEAN HINDCAST MODEL.....	18
Abstract.....	19
1. Introduction .....	20
2. Model.....	22
2.1. Open boundary and Initial Conditions.....	23
2.2. Surface Forcing.....	24
3. Results .....	25
3.1. Model Data Comparisons .....	25
<i>A. Sea Surface height comparison .....</i>	<i>25</i>
<i>B. Shelfbreak hydrography comparison .....</i>	<i>26</i>
<i>C. Decorrelation scale comparison .....</i>	<i>27</i>
3.2. Model Analysis.....	28
<i>A. Mean shelfbreak frontal structures .....</i>	<i>28</i>
<i>B. Bimonthly mean shelfbreak jet structures .....</i>	<i>29</i>
<i>C. Bimonthly mean bottom boundary layer detachment.....</i>	<i>30</i>
<i>D. Cross-shelf migration of shelfbreak front .....</i>	<i>31</i>

4. Discussion.....	32
4.1. Vorticity and momentum balance.....	32
4.2. Cross shelf transport and flux.....	34
4.3. Dominant Modes of shelfbreak jet.....	37
5. Summary.....	39
Acknowledgement.....	41
Tables.....	46
Figures.....	47

**CHAPTER 3: SEASONAL AND INTERANNUAL VARIABILITY OF PHYSICAL AND BIOLOGICAL DYNAMICS AT THE SHELFBREAK FRONT OF THE MIDDLE ATLANTIC BIGHT: NUTRIENT SUPPLY MECHANISMS ..... 59**

Abstract.....	60
1. Introduction.....	60
2. Methods.....	62
2.1. The circulation model.....	62
2.2. The biological model.....	63
3. Model-Data Comparisons.....	63
4. Discussions.....	66
4.1 Seasonal and interannual variability of biological dynamics.....	66
<i>A. Seasonal variability</i> .....	66
<i>B. Interannual variability</i> .....	67
<i>C. Dominant modes of variability</i> .....	67
4.2. Physical control on nutrient delivery.....	69
4.3. Nutrient budget diagnostics.....	71
5. Summary and Conclusion.....	73
Acknowledgments.....	75
Figures.....	81

CHAPTER 4: DATA ASSIMILATIVE MODELING INVESTIGATION OF GULF STREAM WARM CORE RING INTERACTION WITH CONTINENTAL SHELF AND SLOPE, PART 1: METHOD.....	94
Abstract.....	95
1. Introduction.....	95
2. Model and Configuration.....	96
3. 4D Variational Data Assimilaton.....	99
3.1. ROMS-IS4DVAR.....	99
3.2. Observational data.....	101
3.3. Data Assimilation Setup.....	103
3.3.1. Covariance modeling.....	103
3.3.2. Assimilation cycle.....	104
4. Results.....	105
4.1. Cost function behavior.....	105
4.2. Assimilation Statistics.....	106
4.2.1. Surface Performance.....	106
4.2.2. Subsurface Performance.....	108
4.3. Independent data comparison.....	110
4.4. Evolution of the Warm Core Ring in 2006.....	112
5. Discussions and Summary.....	113
Reference.....	116
Figures.....	119
CHAPTER 5: DATA ASSIMILATIVE MODELING INVESTIGATION OF GULF STREAM WARM CORE RING INTERACTION WITH CONTINENTAL SHELF AND SLOPE, PART 2: DYNAMICS.....	132
Abstract.....	133
1. Introduction.....	133
2. Data Assimilative Model.....	134

3. The Evolution of the Warm Core Ring.....	136
4. Shelf/slope exchange .....	139
5. Vorticity Analysis .....	142
6. Discussions and summary .....	143
Appendix A: Depth Averaged Momentum and Vorticity Equation .....	146
Appendix B: Derivation of JEBAR term.....	147
Figures .....	153
CHAPTER 6: SUMMARY AND CONCLUSIONS.....	166

## LIST OF TABLES

### Chapter 2

Table 1. Comparisons of state variable de-correlation scales derived from in-situ survey in July 1996 ( <i>Gawarkiewicz et al.</i> 2004, JGR) and from the shelfbreak model hindcast results in July 2006.....	46
--	----

## LIST OF FIGURES

### CHAPTER 2

- Figure 1. The high resolution shelfbreak model domain (box) and the location of Nantucket transect discussed in the manuscript (dashed line). Also shown is the satellite track (solid line), along which the sea surface height anomaly data were sampled. The curve and dots along the 200 m isobath and their associated numbers indicate the along-isobath distance downstream from the model's northeastern boundary.....47
- Figure 2. Hovmoller diagrams of satellite observed and model simulated sea surface height anomaly (SSHA) along the cross-shelf transect for the period from January 2004 to December 2007 (upper panels) and the comparison of spectra of satellite observed (dashed line) and model simulated (solid line) sea surface height anomaly in the MAB shelfbreak region (lower panel).....48
- Figure 3. The bi-monthly mean temperature transect comparison between the model solutions (left panels) and the climatology (right panels) of *Linder and Gawarkiewicz (1998)*.....49
- Figure 4. The bi-monthly mean salinity transects comparison between the model solutions (left panels) and the climatology (right panels) of *Linder and Gawarkiewicz (1998)*.....50
- Figure 5. Model simulated mean temperature, salinity, along-shelf velocity and cross-shelf velocity fields along the Nantucket transect.....51
- Figure 6. Simulated bi-monthly mean along-shelf velocity fields and their associated net equatorward transport. The black contour lines are the 34.5 isohaline of the respective bimonthly salinity field to indicate the location of shelfbreak front.....52
- Figure 7. Bi-monthly Accumulated Theta Change (ATC) fields along the Nantucket transect. The ATC calculation is based on modeled bi-monthly density fields. The purple lines are the isopycnals, and the color shading stands for the intensity of ATC. The upward tilted, low-value ATC (indicated by arrows) is an indication of the BBL convergence and detachment.....53
- Figure 8. Monthly migrations of the shelfbreak frontal foot (left) and the histogram showing the corresponding depth of the frontal foot in each month.....54
- Figure 9. The comparison between simulated (left) and observed (right, adopted from *Fratantoni et al., 2001*) mean vorticity fields at the shelfbreak. Both fields are scaled by the local Coriolis parameter.....55
- Figure 10. The mean cross-shelf momentum balance. From top to bottom and left to right are the Coriolis force, the Pressure Gradient force (PGF), the residual of Coriolis plus PGF terms (i.e., ageostrophic term), the viscosity term, the residual of ageostrophic term plus viscosity, the nonlinear advection term, the residual of ageostrophic plus viscosity and advection terms, and the local rate of change term.....56

Figure 11. The cross-shelf volume transport along the 200 m isobath inside the shelfbreak ROMS domain. The x-axis is the along-isobath distance starts from zero (off the Nantucket shoal) to 300-km (off the Hudson Canyon). The solid curve is the mean cross-shelf volume transport over the 4-year period, and the gray area stands for its standard deviation.....57

Figure 12. The first two EOF modes of simulated shelf break circulation, and their corresponding principle components. U (V) is the alongshore (cross-shelf) velocity component along the Nantucket transect.....58

### CHAPTER 3

Figure 1. The shelfbreak model domain (box) and the location of Nantucket transect discussed in the following sections (solid line). Also shown is a satellite (Jason1) sub-track (dotted line). The thick line along the northeastern boundary defines the location of the upstream nutrient input calculation. Local isobaths are also shown in light gray.....81

Figure 2. Monthly domain-averaged surface chlorophyll from the shelfbreak model (red) and Aqua-MODIS data (blue, with one standard deviation).....82

Figure 3. Taylor Diagram for domain-averaged surface chlorophyll concentrations from 2004 to 2007. Radial distance represents the ratio of simulated to observed standard deviations, and azimuthal angle represents model-data correlation. Green arcs represent centered root mean square difference between model and data.....83

Figure 4. Seasonal surface chlorophyll comparisons based on simulated and observed 4-year mean results. Shown in the left column are model results and those in the right column are MODIS observed results, with the model domain overlaid (black box). 100 and 200 m isobaths are also shown (white curves).....84

Figure 5. Monthly mean time series of nutrient, phytoplankton and zooplankton components simulated by the model.....85

Figure 6. Inter-annual evolution of domain-averaged nutrient concentration (upper panel) and phytoplankton concentration (lower panel) at the MAB shelfbreak.....86

Figure 7. Inter-annual variability of nutrient concentration. Shown in the left from top to bottom are the spring mean upper water column (upper 50 m average) nutrient field averaged over 2004-2007, and the corresponding nutrient anomaly fields in springs 2004 through 2007 relative to their 4-year mean. Shown in the right from top to bottom are the spring mean nutrient field along the Nantucket transect, and the corresponding across-shelf nutrient anomaly fields in springs 2004 through 2007 relative to their 4-year mean. Also shown in the left panels are the location of the Nantucket transect, and 100 and 200 m isobaths (white curves).....87

Figure 8. EOF analyses of upper water column (averaged over the upper 50 m) nutrient, phytoplankton and zooplankton fields. Mean fields are shown in the top panels, the first EOF modes with the variance they account for (also shown in the brackets are percentages of 2<sup>nd</sup> mode variance) are shown in the middle panels and their corresponding

1<sup>st</sup> principle components are shown in the bottom panels. Also shown are isobaths (gray curves) with 200 m isobath highlighted in white.....88

Figure 9. EOF analyses of nutrient, phytoplankton and zooplankton along the Nantucket transect. Their temporal mean fields are shown on the top panels, the first EOF modes are shown in the middle panel with the variance they account for (also shown in the brackets are percentages of 2<sup>nd</sup> mode variance) and the corresponding 1<sup>st</sup> principle components are shown at the bottom panels.....89

Figure 10. Monthly means of domain-averaged upper 50 m nutrient concentration (solid line), the upstream nutrient influx (dashed line), and mixed layer depth from 2004 to 2007. Both N-influx and local N time series are normalized, whereas the domain-averaged, monthly mean MLD is not and has unit of meter.....90

Figure 11. Spatial correlations between the bottom convergence and NO<sub>3</sub> concentration in the upper 50 m. Also shown are isobaths (gray curves) with 100 and 200 m isobaths highlighted in white.....91

Figure 12. Inter-annual variability of total kinetic energy (TKE: left column) and shelfbreak jet (right column). The top two panels show the spring mean TKE and shelfbreak jet velocity (across the Nantucket transect; positive means westward flow) averaged over 2004-2007. The following panels show the anomaly fields of TKE and shelfbreak jet in springs 2004 through 2007 relative to their respective 4-year means. Also shown in the left hand panels are 100 and 200 m isobaths (white curves) and location of Nantucket transect (black line).The mean  $\langle u \rangle$  and anomaly  $u'$  alongshelf transport values are given in the right-hand panels.....92

Figure 13. Term-by-term diagnostic analysis of nutrient equation. Shown from left to right are the local rate of change ( $\partial N/\partial t$ ), horizontal advection (HADV), vertical advection (VADV), vertical diffusion (VDIFF), and biological source/sink (SmS) terms averaged over the early spring season (February-March-April) in year 2004 (top panels) and 2007 (bottom panels). The unit for all these terms is  $\text{mmol N}\cdot\text{s}^{-1}$ .The 34.5 isohaline is also shown in each figure as black curve to indicate the position of the shelfbreak front. Two gray vertical lines indicate the locations of 100 and 300m isobaths, between which the shelfbreak jet net nutrient budget terms are computed.....93

**CHAPTER 4**

Figure1. Mid Atlantic Bight and Gulf of Maine model domain. The bathymetry of this region is shown in color. The Endurance line along which gliders are flied is denoted in thick black line. Line-W Oceanus CTD stations are shown in black stars. ECOMON CTD stations in May 2006 are shown in black dots.....119

Figure2. Comparison of mean sea surface height from the forward model (MABGOM) and AVISO observations.....120

Figure 3. A schematic showing the assimilation cycles. Shaded columns represent overlaps between cycles.....121

Figure4. Super observations of sea surface height (SSH, upper left), sea surface temperature (SST, upper right), in-situ temperature profiles (lower left), in-situ salinity profiles (lower right). Only SST and SSH on Apr1st, 2006 are shown while all profiles collected during the assimilation period (Apr1st, 2006 to May 31st, 2006) are shown...122

Figure 5. temporal distributions of super observations. SSH, SST, in-situ temperature profiles, in-situ salinity profiles, Endurance line glider T/S observations, and Line-W Oceanus CTD T/S observations are shown in blue, yellow, red, and cyan, magenta and green, respectively.....123

Figure 6. Cost function in first window and last window. Shown on the left column are evolutions of cost functions versus the number of inner loops during the first and last assimilation windows while on the right are changes of total cost function with respect to the inner loops. Total cost function are shown in solid while background cost functions are shown in dash-dot. The theoretical minimum value of total cost functions are shown in dashed lines. Crosses represent the value of nonlinear cost function.....124

Figure 7. Root Mean Square error of assimilated sea surface height. Spatial distribution of RMSE between forward model and observation is shown on the upper left. RMSE between model posterior and observations is shown on the upper right. Time series of spatial averaged RMSE of assimilated SSH are also shown in the bottom panel.....125

Figure 8. Root Mean Square error of assimilated sea surface temperature. Spatial distribution of RMSE between forward model and observation is shown on the upper left. RMSE between model posterior and observations is shown on the upper right. Time series of spatial averaged RMSE of assimilated SST are also shown in the bottom panel.....126

Figure 9. Bias of assimilated in-situ temperature and salinity on the continental shelf. Vertical distribution of biases of temperature and salinity over the assimilation period are shown in the top two panels, with biases from the forward model, 4DVAR prior and posterior denoted in dashed, dotted and solid lines. Time series of assimilated temperature and salinity biases are also shown.....127

Figure 10. Comparison of temperature and salinity profiles from ECOMON in-situ observation, MABGOM forward model and 4DVAR posterior.....128

Figure 11. One to one plot of ecomon observed versus modeled temperature (left) and salinity (right). Temperature (salinity) from the forward model is shown in gray while temperature (salinity) from DA posterior is shown in black. Slope and intercept are also shown in the parenthesis, respectively.....129

Figure12. Bi-weekly Evolution of sea surface height during the assimilation period. Showing in the first column are satellite observations while MABGOM forward model and 4DVAR posterior results are shown in the second and third column.....130

Figure13. Bi-weekly Evolution of sea surface temperature during the assimilation period. Showing in the first column are satellite observations while MABGOM forward model and 4DVAR posterior results are shown in the second and third column.....131

## CHAPTER 5

- Figure 1. Mid Atlantic Bight and Gulf of Maine model domain. The bathymetry of this region is shown in color. 1000m isobath along which the cross-shelf transport and fluxes are calculated is shown in white curve. The relative along-isobath distance with respect to the starting point are also labeled.....153
- Figure 2. Surface height, surface temperature, surface salinity and surface vorticity on April 2nd, 2006. Also shown are streamfunction contours (gray) and e-folding value (thin white contour) of maximum streamfunction. The center of the meander/ring is shown by black star while its track is shown every 3 day in black dots. The thick white curve is isohaline 34.5 and the thin black curve is 200m isobaths. Two cross-shelf transects are depicted in black line segment.....154
- Figure 3. Same as figure 2 but on April 22nd, 2006.....155
- Figure 4. Cross-section view of temperature, salinity and velocity along cross-shelf directional transect at the center of WCR on April 22nd, 2006.....156
- Figure 5. Same as figure 2 but on May 2nd, 2006.....157
- Figure 6. Same as figure 2 but on May 9th, 2006.....158
- Figure 7. Same as figure 4 but on May 9th, 2006.....159
- Figure 8. Same as figure 2 but on May 30th, 2006.....160
- Figure 9. cross-shelf volume transport along 1000m isobath. Mean values (April 22nd to May 18th) are shown in solid black curve while standard deviation are shown in blue. Negative values stand for onshore transport while positive values stand for offshore transport.....161
- Figure 10. Cross-shelf eddy heat/salt fluxes during WCR period.....162
- Figure 11. Depth averaged relative vorticity and its source and sink terms during the WCR impinging period. (a) and (b) Depth averaged relative vorticity on May 1st and May 7th 2006, respectively, with horizontal colorbar. Sea surface height are shown in gray contours. (c) Time rate change of depth averaged relative vorticity (rate). (d) Advection of potential vorticity (APV). (e) Joint Effect of Baroclinicity and Bottom Relief (JEBAR). (f) Residual of JEBAR and APV. (g) Nonlinear advection of relative vorticity (ADV). (h) Total effect of JEBAR, APV and ADV. (i) Residual of JEBAR, APV, ADV and rate terms. All source and sink terms are scaled with the vertical colorbar. In each panel, the 200m and 1000m isobaths are shown in black curves. ....163
- Figure 12. Cross-section view of mean temperature, salinity, along-shelf velocity along west transect and east transect from April 22<sup>nd</sup> to May 18<sup>th</sup> .....164
- Figure 13. Mean temperature and velocity before WCR impingement (April 1<sup>st</sup> to 20<sup>th</sup>, left column) and during WCR impingement (May 1<sup>st</sup> to 7<sup>th</sup>, right column). Surface fields

are shown in the first row while subsurface (50m) fields are shown in the second row.  
Locations of two transects in Figure 12 are also shown.....165

## CHAPTER 1: INTRODUCTION

The northeastern coast of North America has a continental shelf extending over 5000km from Cape Chidley, in the mouth of Hudson Bay, to Cape Hatteras. The shelf width and depth are typically 100-200 km and 100-200m. From a basin-scale ocean circulation perspective, the coastal segment lies in the western boundary confluence zone of the North Atlantic Subpolar Gyre and North Atlantic Subtropical Gyre, with additional important influences imposed by geometry, inflow from the polar region and other local forcing factors. The study domain of this research, the Middle Atlantic Bight, sits right in the southern portion of this segment.

The MAB shelfbreak frontal region is an area subject to many dynamic oceanic processes. Despite several decades of efforts, we have rather incomplete understanding on the origins, energetics and consequences of many of these processes. Yet, the shelfbreak front is known to play a critical role as the gate keeper for the transfer of mass, heat, salt, and other dissolved or suspended materials between the shelf and deep-ocean (e.g., Lord et al., 1998; Flagg et al., 2006). In order to quantify the shelf/slope exchange of mass and tracers, we need to improve our understanding of ocean dynamics of this critical component of the MAB shelf system.

In this chapter, we will first briefly describe the general hydrographic and circulation conditions in the Northeast US coastal ocean. Then we will focus on the shelfbreak frontal system in the Middle Atlantic Bight. Details of research objectives and outline of the entire dissertation will be given in the end.

## **1. Hydrography and General Circulation**

The surface salinity in the Northeast US coastal ocean increases offshore. A low salinity band is distributed along the coast, reflecting direct influence of river runoff. The shelf-wide annual salinity variation ranges from 1 to 2 psu, reaching minimum in the summer as the result of maximum coastal runoff and sea ice melt in the spring time. Shelfwater surface temperature also shows substantial influence from ocean advection, but it has a strong annual variation associated with local air-sea interactions. The average SST ranges are 0-7°C in winter and 5-27°C in summer.

The regional coastal water stratification has a clear seasonal variation. Taking the New England shelf-slope region as an example, in August, the wind stress is weak, the net surface heat flux is positive, resulting in the development of a strong thermocline over the shelf at about 10 m depth. The shelfwater stratification then decreases from September to November in response to strong mixing associated with storm events, becoming essentially unstratified in mid-November. Beginning in mid-December, the near bottom water temperatures typically increases due to onshore displacement of relative warm shelf-slope front water, which in conjunction with cold near-surface water results in a substantial temperature inversion that can persist for much of the winter. Near-bottom temperature decreases in early spring as the water column becomes well mixed again. During March to June, wind stress magnitudes decreases and surface heating increased from March to June. Increasing surface temperatures and relatively constant near-bottom temperatures resulted in the development of thermal stratification and the winter remnant of shelf water is well known as the “cold pool” (Beardsley and Flagg, 1976; Houghton et al., 1982).

The mean circulation of the northeastern North America coastal ocean is equatorward (e.g., Loder et al, 1998; Fratantoni and Pickart, 2007). The inflow on the Scotian shelf has two interconnected origins, one from Cabot Strait outflow, and the other from Labrador Current water across Laurentian Channel. Downstream, the circulation in the Gulf of Maine is strongly steered by topography, with cyclonic flow around the inner basins and anticyclonic flow around outer banks. The shelf circulation returns to a more uniform pattern in the Middle Atlantic Bight with southwestward flow in the inner and outer shelves. This mean equatorward flow continues to Cape Hatteras, albeit with continually decreasing transport. It is worth noting that such a continuous but leaky equatorward flow conveys a subpolar influence to the shelf oceanographic regime throughout the northeastern North American coastal segment.

Recent studies (Loder et al, 1998). indicate the buoyancy is the primary forcing of upper-slope branches of Labrador Current, whereas the large-scale wind stress is the forcing of deep-water branch. Thus, it has been suggested that a suite of interacting physical processes allows modified remnants of the subpolar western boundary current to extend through the entire northeastern North American coastal segment.

Lagrangian drifter studies have provided supporting evidence for this equatorward mean flow pattern and also indicated that the southward shelf flow could hardly extend into the South Atlantic Bight in that most of the flows are entrained into Gulf Stream just north of Cape Hatteras. For example, the study by Gawarkiewicz and Linder (2006) suggests there are two types of entrainment into the Gulf Stream, abrupt and gradual. The events of abrupt drifter entrainment are characterized by a sharp change in drifter

direction with a rapid increase in speed, while drifter trajectories of the gradual entrainment events have a large radius of curvature and small increases in speed.

Compared to the along-shelf flow, dynamics involved in the across-shelf circulation are considerably more complex. Several processes have been identified as contributing factors to shelf-ocean exchange in the Middle Atlantic Bight, the most dramatic one being Gulf Stream ring interactions with the shelf water/Slope Water front (e.g., Joyce et al., 1992; Garfield and Evans, 1987). In addition,, the mid-depth intrusion (e.g., Gordon and Aikman, 1981), shelfbreak frontal eddies (e.g., Gawarkiewicz et al., 2001), topography (e.g., Chapman and Gawarkiewicz, 1995), and baroclinic instabilities (e.g., Lozier et al., 2002) all have varying influence on the cross-shelf exchange. As a result, robust estimates of cross-shelf transport are difficult to obtain.

## **2. Shelfbreak System**

Zooming in to the shelfbreak of the Middle Atlantic Bight (MAB), the shelfbreak front in the area is a persistent thermohaline front that separates relatively cold and fresh shelf waters from warm, salty waters on the continental slope. Coincident with the front is a narrow jet, which has been estimated to transport approximately 0.2–0.3 Sv of water equatorward south of New England (Linder and Gawarkiewicz, 1998). This shelfbreak frontal jet is part of a large-scale buoyancy driven coastal current system that originated from Labrador Sea (Chapman and Beardsley, 1989). The shelfbreak jet is an important component of the coastal environment in the northwest Atlantic. The front and jet represent a semi-permeable barrier that limits the exchange of waters between the shelf

and open-ocean. The cross-shelf exchange that does occur strongly impacts the spreading of coastal contaminants and is of leading importance in the freshwater budget on the shelf.

Intensive studies since the 1970s, all with the goal of understanding the dynamics of the front and the critical shelf and slope exchange processes, have been carried out using moorings and hydrographic surveys at various locations and for varying durations, such as NESDE (Beardsley and Flagg, 1976), NSFE (Beardsley et al., 1985), SEEP-I (Walsh et al., 1988), SEEP-II (Biscaye et al., 1994), OMP (Verity et al., 2002), and CMO/PRIMER (Dickey and Williams, 2001). In addition, there have been several smaller programs aimed at studying frontal meanders and eddies. The hydrography of the shelfbreak region has been described in a number of syntheses, and one of the latest is that by Linder and Gawarkiewicz (1998) based upon the Hydrobase dataset (Curry, 1996) for portions of the Middle Atlantic Bight.

It has been suggested that the formation of the shelfbreak front is a result of a complex interplay between upstream (Chapman, 1986; Loder et al., 1998) and nearshore sources of relatively buoyant equatorward flowing waters that form a bottom boundary layer with an offshore transport. This offshore, near-bottom transport ultimately breaks away from the bottom and upwells into the interior at an isobath that depends upon the total alongshore transport (Chapman, 1986, 2002; Chapman and Lentz, 1994, 1997; Gawarkiewicz and Chapman, 1991, 1992; Yankovsky and Chapman, 1997). The role of convergence in the front clearly plays a major role in the cross-frontal density contrast and the convergence within the bottom boundary layers from either side of the foot of the front has been well demonstrated by the dye release studies of Houghton (1995, 1997),

Houghton and Visbeck (1998) and the turbidity plume clearly visible in the SEASOAR sections of Barth et al. (1998, 2004). In the other part of the frontal zone, there is convergence as Gawarkiewicz et al (2001) clearly showed in a springtime cruise. This frontal convergence was also captured by Flagg et al (2006) over a larger time scale. Frantantoni et al. (2001) also observed an upper layer convergence and they attributed to the downstream convergence of the isobaths. Ou (2006) identified three regimes of horizontal mixing in the coastal ocean as one proceeds offshore: they are associated with tides, wind-driven motion, and meso-scale eddies, progressively. The first two are through oscillatory shear dispersion, the transition being due to their disparate forcing timescales; the last is merely conjectured as limited to the slope water. It is the minimum mixing between these regimes that gives rise to the tidal and shelfbreak fronts. The mechanistic unification of these two prominent but seemingly unrelated fronts lends support to this overlooked category of front-genesis that stems from spatial inhomogeneity in the horizontal mixing.

Flagg et al. (2006) studied the mean velocity field in the shelf-slope region using a decade of shipboard ADCP observations in the Middle Atlantic Bight (along the transect from Bermuda to Port Elisabeth). The results showed that alongshore velocities are all to the west, ranging from 0 to about 0.13 m/s in the center of the shelfbreak jet. The offshore velocity component ranged from near 0 over the shelf to 0.06 to 0.08 m/s offshore and at depth. The shelfbreak jet shows a surface intensified velocity structure, spanning the 80 to 150 m isobaths and centered over the 120 m isobath with a vertical extent of some 60 m and a mean width of about 30 km. Offshore of the jet for some 20 to 40 km and extending downward to the maximum range of the ADCP there exists a wide area of reduced

alongshore flow. Perhaps the most intriguing aspect of the mean velocity section, as the author mentioned is the broad area of southwestward flowing slope water extending down to roughly 300 m. Their study also showed that core of the shelfbreak jet lies just offshore of the 100 m isobath. There is also a region of relatively lower currents just offshore of the shelfbreak jet. Farther offshore lies the slope current with velocities nearly equivalent to those in the shelfbreak jet. The results also indicate a convergence region just offshore of the shelfbreak jet, which can also be verified by looking at the vertical profile of the cross-shelf velocity component.

The vertically integrated alongshore transports and their cumulative integral proceeding offshore provide another aspect of the shelfbreak current structure. The vertically integrated transport is about  $2 \text{ m}^2/\text{s}$  inshore of the shelfbreak jet but jumps up to  $7$  to  $8 \text{ m}^2/\text{s}$  in the core of the jet and then climbs to a maximum of  $37 \text{ m}^2/\text{s}$  in the center of the slope current. From the result of cumulative transport integral, the shelfbreak jet is responsible for approximately  $0.4 \text{ Sv}$  while the slope current adds another  $2.5 \text{ Sv}$  for a total alongshore transport between 14 and 400 m isobaths of nearly  $3 \text{ Sv}$ .

Another way to look at the characteristics of the shelfbreak jet is to attempt to track the core of the jet as it oscillates across the isobaths and occasionally changes its orientation. By setting up the “stream-wise” coordinate system, the following results were acquired by Frantantoni et al (2001). The maximum mean velocity of the jet is about  $0.35 \text{ m/s}$  in the  $8 \text{ m}$  bin centered at a depth of  $26 \text{ m}$  compared to the maximum Eulerian velocity of  $0.13 \text{ m/s}$ . The jet velocities taper symmetrically to each side with an e-folding distance of about  $15 \text{ km}$ , a width that is very similar to Eulerian field. The cross-jet

velocity structure also shows a coherent structure in the upper 40 to 50 m that reflects a strong convergence to the center of the jet.

Based on the Oleander observations, Flagg et al.,(2006) further depicted the seasonal and interannual variability of the shelf-slope current. In general, shelfbreak jet accelerates in the fall and becomes strongest in the winter months with a maximum mean speed of over 0.2 m/s and a width of some 20 to 30 km.

Inshore of the shelfbreak jet (i.e., the transecting distance less than 150 km from Ambrose Light), there is little seasonal variability. The maximum alongshore flow begins around year-day 320 and lasts through year-day 80, with a long hiatus during the spring and summer. About 250 km offshore there is a definite phase lag of the maximal southwestward alongshore flow of the slope current relative to the shelfbreak jet, suggesting that the slope current begins to accelerate earlier inshore. The on-offshore seasonal signal of the shelfbreak jet itself is rather small with slightly greater offshore components in the spring and fall. The slope current, shows a substantial on-offshore variability with onshore flow during the winter through summer and an offshore bias during the early fall.

Fratantoni et al. (2000) used EOF analysis to study the ensemble of velocity sections in order to identify the dominant modes of variability associated with the structure of the shelfbreak jet. The jet appears to systematically fluctuate between a bottom-reaching, convergent state (similar to the mean structure) and a more surface-trapped state with weaker, cross-stream velocities. The transition between the bottom-reaching and surface-trapped jet is correlated with a significant change in equatorward transport.

Fratantoni and Pickart (2003) also studied the meso-scale variability at shelfbreak region near Nantucket Shoals using bottom-mounted acoustic Doppler current profilers. While the flow is predominantly equatorward, the current is regularly interrupted by bursts of poleward flow. These are manifestations of a periodic full water column weakening of the shelfbreak current. Throughout most of the record, significant deceleration occurs more frequently and with greater intensity at the offshore site. Furthermore, the decelerations penetrate higher into the water column at the offshore mooring than at the inshore ADCP. Significant decelerations (and actual flow reversals) occur most often in the middle to lower portion of the water column. It is the origin of these fluctuations which is the focus of their analysis. Total kinetic energy spectra showed that energy at the offshore shelfbreak ADCP is sharply peaked at 13 days. The energy in this band decreases with depth. By contrast, a majority of the energy at the inshore ADCP is concentrated at shorter periods (8–11 days), and is more uniformly distributed over the depth of the water column. These two spectra suggest that different processes may be contributing to the variability at the inshore and offshore sites.

Indeed, numerous studies have shown that the shelfbreak jet is influenced by both external and internal forcing mechanisms. Theoretical studies (Flagg and Beardsley 1978; Gawarkiewicz 1991; Lozier et al., 2002) and observations (Linder and Gawarkiewicz 1998) have shown that the jet structure is inherently baroclinically unstable. This internal forcing may lead to finite-amplitude meanders that propagate along the axis of the jet (Halliwell and Mooers 1979) and occasionally develop into frontal eddies (Houghton et al. 1986; Garvine et al. 1988). In addition, the jet may be influenced by external forcing mechanisms such as local winds (Houghton et al. 1988) and upstream variations in the

source water (Chapman and Beardsley 1989; Petrie and Drinkwater 1993). Another important external influence on the jet is the circulation of the adjacent slope water. For instance, the close proximity of the Gulf Stream south of New England results in a fair number of anticyclonic Gulf Stream rings impinging on the continental slope in the MAB. It remains unclear what role Gulf Stream rings play in the variability at the shelfbreak. Beardsley et al. (1985) report that subtidal fluctuations forced by the passage of Gulf Stream rings over the upper continental slope are not correlated with fluctuations observed over the shelf, suggesting that the shelfbreak can be a transition region for forcing. Ramp et al. (1983) demonstrated that the presence of Gulf Stream rings enhances cross-shelf velocity gradients in the vicinity of the shelfbreak jet and can lead to the excitation of waves due to horizontal shear instabilities. Observations also suggest that the interaction of Gulf Stream rings with the shelfbreak jet may transport significant volumes of shelf water into the slope region (Joyce et al. 1992). However, it is unclear how often rings simply alter the path of the shelfbreak jet (e.g., Pickart et al. 1999) versus permanently exporting water from the shelf.

### **3. Research Motivations and Objectives**

While providing many valuable insights on the shelfbreak frontal dynamics, most of earlier studies mentioned above focused on event scales, and were limited by coarse temporal and spatial resolutions. This is especially true in light of work including *Garvine et al.* (1988), *Lozier et al.* (2002) and *Gawarkiewicz et al.* (2004), which showed that frontal instabilities and shelf-slope interactions are reoccurring features with fine temporal and spatial scales as small as 1-2 day and 8-15km, respectively. In addition to

in-situ data, remote sensing observations provide another means for shelfbreak circulation study (e.g., *Ryan et al.* 1999). While being useful for detecting shelfbreak temperature (SST) and optical variability (ocean color), they are unable to provide concurrent three-dimensional structures of shelfbreak circulation and water properties.

Because of these limitations, despite decades of research cruises and multi-year moorings and remote-sensing based observations, the understanding of the internal and external processes that control the dynamics and ecosystem interactions at the MAB shelfbreak front is still inadequate. Improved understanding of the MAB shelfbreak circulation and better quantification of its variations therefore require high-resolution, space and time continuous realizations of ocean state variables, from which detailed dynamics can be gleaned.

The overall objective of this research is to better understand the MAB shelfbreak circulation dynamics and biophysical interactions through a series of systematic numerical modeling investigations. The specific goals include:

- 1) Better characterizing the mean states and temporal and spatial variations of the MAB shelfbreak front and jet;
- 2) Quantifying the volume transport, salt and heat flux exchanges across the MAB shelfbreak and their transport pathways;
- 3) Investigating the biophysical interactions between the MAB shelfbreak circulation and nutrient and plankton distributions.
- 4) Understanding the influence of warm-core rings on the MAB shelf and shelfbreak circulation

#### **4. Dissertations outline**

In this dissertation, Chapter 2 focuses on the circulation dynamics at the MAB shelfbreak. The mean condition and variability of shelfbreak front and jet are discussed based on simulations from a high resolution circulation model, based on which, detailed dynamics of the shelfbreak frontal circulation are also diagnosed.

Coupled biophysical interactions at the MAB shelfbreak are next investigated in Chapter 3. A size-structured, multi-nutrient ecosystem model is coupled with the shelfbreak circulation model described in Chapter 2. Seasonal and interannual variations of both physical and biological variables are discussed. Detailed analyses are performed to address how the shelfbreak circulation and other physical environment factors control nutrient delivery and further affect plankton biomass distributions.

The influence of a large warm-core ring (WCR) on the MAB shelf and shelfbreak circulation is examined in Chapter 4 and Chapter 5. Due to the fact that the forward model has difficulty in accurately resolve the location and intensity of the Gulf Stream warm-core ring, an advanced variational data assimilation technique is used. Serving as the first part of this study, Chapter 4 introduces the state-of-art 4-dimensional variational (4DVAR) data assimilation method and its configuration in modeling the large WCR in April-May 2006. Extensive model-data validations are performed, showing the 4DVAR assimilation schemes works well in resolving the life history of this WCR and its strong interactions with the shelf/slope circulation. Based on these data assimilative circulation hindcast solutions, detailed ocean dynamic analyses and calculations of shelf/slope exchanges are presented in Chapter 5.

Finally Chapter 6 provides the summary and conclusions drawn from this dissertation research, as well as a discussion on future research.

## References

- Barth, J. A., D. Bogucki, S. D. Pierce, and P. M. Kosro, 1998: Secondary circulation associated with a shelfbreak front. *Geophysical Research Letters*, 25, 2761-2764.
- Barth, J. A., D. Hebert, A. C. Dale, and D. S. Ullman, 2004: Direct observations of along-isopycnal upwelling and diapycnal velocity at a shelfbreak front. *Journal of Physical Oceanography*, 34, 543-565.
- Beardsley, R. C. and C. N. Flagg, 1976: Water structure, mean currents, and shelf-water/slope-water front on the New England continental shelf. *Seventh Liege Colloquium on Ocean Hydrodynamics, Societe Royale des Sciences*, 209-226.
- Beardsley, R. C., D. C. Chapman, K. H. Brink, S. R. Ramp, and R. Schlitz, 1985: The Nantucket Shoals Flux Experiment (NSFE79). Part 1, A basic description of the current and temperature variability. *Journal of Physical Oceanography*, 15, 713-748.
- Biscaye, P. E., C. N. Flagg, and P. G. Falkowski, 1994: The Shelf Edge Exchange Processes experiment, SEEP-2: an introduction to hypohese, results and conclusions. *Deep-Sea Research Part 2*, 41.
- Chapman, D. C., J. A. Barth, R. C. Beardsley, and R. G. Fairbanks, 1986: On the continuity of mean flow between Scotian Shelf and the Middle Atlantic Bight. *Journal of Physical Oceanography*, 16, 758-772.
- Chapman, D. C. and R. C. Beardsley, 1989: On the origin of shelf water in the Middle Atlantic Bight. *Journal of Physical Oceanography*, 19, 384-391.
- Chapman, D. C. and S. J. Lentz, 1997: Adjustment of stratified flow over a sloping bottom. *Journal of Physical Oceanography*, 27, 340-356.
- Chapman, D. C., 2002: Sensitivity of a model shelfbreak front to the parameterization of vertical mixing. *Journal of Physical Oceanography*, 32, 3291-3298.
- Csanady, G. T. and P. Hamilton, 1988: Circulation of slope water. *Continental Shelf Research*, 8, 565-624.
- Curry, R. G., 1996: *HydroBase -- A database for hydrographic stations and tools for climatological analysis*, 44 pp.
- Dickey, T. D. and A. J. Williams, 2001: Interdisciplinary ocean process studies on the New England Shelf. *Journal of Geophysical Research*, 106, 9427-9434.
- Dong, S. and K. A. Kelly, 2003: Seasonal and interannual variations in geostrophic velocity in the Middle Atlantic Bight. *Journal of Geophysical Research*, 108, 3172.
- Flagg, C. N. and B. C. Beardsley, 1978: On the stability of the shelf-water/slope-water front south of New England. *Journal of Geophysical Research*, 83, 4623-4631.

- Flagg, C. N., M. Dunn, D.-P. Wang, H. T. Rossby, and R. L. Benway, 2006: A study of the currents of the outer shelf and upper slope from a decade of shipboard ADCP observations in the Middle Atlantic Bight. *Journal of Geophysical Research*, 111, doi:10.2029/2005JC003116.
- Fratantoni, P. S., R. S. Pickart, D. J. Torres, and A. Scotti, 2001: Mean Structure and Dynamics of the Shelfbreak Jet in the Middle Atlantic Bight during Fall and Winter. *Journal of Physical Oceanography*, 31, 2135-2156.
- Fratantoni, P. S. and R. S. Pickart, 2003: Variability of the shelfbreak jet in the Middle Atlantic Bight: Internally or externally forced? *Journal of Geophysical Research*, 108, 3166, doi:10.1029/2002JC001326.
- Fratantoni, P. S. and R. S. Pickart, 2007: The Western North Atlantic Shelfbreak Current System in Summer. *Journal of Physical Oceanography*, 37, 2509-2533.
- Garfield, N. and D. L. Evans, 1987: Shelf Water Entrainment by Gulf Stream Warm-Core Rings. *Journal of Geophysical Research*, 92, 13,003-13,012.
- Garvine, R. W., K.-C. Wong, G. G. Gawarkiewicz, R. K. McCarthy, R. W. Houghton, and F. Aikman, 1988: The morphology of shelfbreak eddies. *Journal of Geophysical Research*, 93.
- Gawarkiewicz, G. G., 1991: Linear stability models of shelfbreak fronts. *Journal of Geophysical Research*, 21, 471-488.
- Gawarkiewicz, G. G. and D. C. Chapman, 1991: Formation and maintenance of shelfbreak fronts in an unstratified flow. *Journal of Physical Oceanography*, 21, 1225-1239.
- Gawarkiewicz, G. G., F. Bahr, R. C. Beardsley, and K. H. Brink, 2001: Interaction of a Slope Eddy with the Shelfbreak Front in the Middle Atlantic Bight. *Journal of Physical Oceanography*, 31, 2783-2796.
- Gawarkiewicz, G. G., K. H. Brink, R. Beardsley, M. Caruso, J. F. Lynch, C. Chiu, 2004: A large-amplitude meander of the shelfbreak front during summer south of New England: Observations from the Shelfbreak PRIMER experiment, *Journal of Geophysical Research*, 109, C03006, doi:10.1029/2002JC001468.
- Gawarkiewicz, G. G. and C. A. Linder, 2006: Lagrangian Flow Patterns north of Cape Hatteras using Near-Surface Drifters. *Progress in Oceanography*, 70, 181-195.
- Gordon, A. L. and F. Aikman, 1981: Salinity maximum in the pycnocline of the Middle Atlantic Bight. *Limnology and Oceanography*, 26, 123-130.
- Halliwell, G. R. and C. N. Moores, 1979: The space-time structure and variability of the shelf water-slope water and Gulf Stream surface temperature fronts and associated warm-core eddies. *Journal of Geophysical Research*, 84, 7707-7725.
- Houghton, R. W., R. Schlitz, R. C. Beardsley, B. Butman, and H. L. Chamberlin, 1982: The Middle Atlantic Bight cold pool: Evolution of the temperature structure during summer 1979. *Journal of Physical Oceanography*, 12, 1019-1029.

- Houghton, R. W., D. B. Olson, and P. J. Celone, 1986: Observation of an anticyclonic eddy near the continental shelfbreak south of New England. *Journal of Physical Oceanography*, 16, 687-710.
- Houghton, R. W., F. Aikman, and H. W. Ou, 1988: Shelf-slope frontal structure and cross-shelf exchange at the New England shelfbreak. *Continental Shelf Research*, 8, 687-710.
- Houghton, R. W., 1995: The bottom boundary layer structure in the vicinity of the Middle Atlantic Bight shelfbreak front. *Continental Shelf Research*, 15, 1173-1194.
- Houghton, R. W., 1997: Lagrangian flow at the foot of the shelfbreak front using a dye tracer injected into the bottom boundary layer. *Geophysical Research Letters*, 24, 2035-2038.
- Joyce, T. M., J. K. B. Bishop, and O. B. Brown, 1992: Observations of offshore shelf water transport induced by a warm-core ring. *Deep-Sea Research*, 39A, S97-S113.
- Linder, C. A. and G. G. Gawarkiewicz, 1998: A climatology of the shelfbreak front in the Middle Atlantic Bight. *Journal of Geophysical Research*, 103, 18,405-18,423.
- Lord, J. W., G. Han, C. G. Hannah, D. A. Greenberg, and P. C. Smith, 1997: Hydrographic and baroclinic circulation in the Scotian Shelf region: winter vs summer. *Canadian Journal of Fisheries and Aquatic Sciences*, 54, 40-56.
- Lord, J. W., B. Petrie, and G. Gawarkiewicz, 1998: The coastal ocean off northeastern North America: A large-scale view. *The Sea*, A. R. Robinson and K. H. Brink, Eds., 105-133.
- Lozier, M. S., M. S. C. Reed, and G. G. Gawarkiewicz, 2002: Instability of a shelfbreak front. *Journal of Physical Oceanography*, 32, 924-944.
- Ou, H. W. and D. Chen, 2006: Wind-induced shear dispersion and genesis of the shelfbreak front. *Progress in Oceanography*, 70, 313-330.
- Petrie, B. and K. Drinkwater, 1993: Temperature and salinity variability on the Scotian Shelf and in the Gulf of Maine 1945-1990. *Journal of Geophysical Research*, 98, 20,079-20,089.
- Pickart, R. S., D. J. Torres, T. K. Mckee, M. J. Caruso, and J. E. Przystup, 1999: Diagnosing a meander of the shelfbreak current in the Middle Atlantic Bight. *Journal of Geophysical Research*, 104, 3121-3132.
- Ramp, S. R., R. C. Beardsley, and R. Legeckis, 1983: An observation of frontal wave development on a shelf-slope/warm core ring front near the shelf break south of New England. *Journal of Physical Oceanography*, 13, 907-912.
- Ryan, J. P., J. A. Yorder, J. A. Barth, and P. C. Cornillon, 1999: Chlorophyll enhancement and mixing associated with meanders of the shelf break front in the Mid-Atlantic Bight. *Journal of Geophysical Research*, 104, 23,479-23,493.
- Verity, P. G., J. E. Bauer, C. N. Flagg, D. J. DeMaster, and D. J. Repeta, 2002: The Ocean Margins Program: an interdisciplinary study of carbon sources, transformations, and sinks in a temperate continental margin system. *Deep-Sea Research part 2*, 49, 4273-3296.

Walsh, J. J., P. E. Biscaye, and G. T. Csanady, 1988: The 1983-1984 Shelf Edge Exchange Processes (SEEP) - 1 experiment hypotheses and highlights. *Continental Shelf Research*, 8.

Yankovsky, A. E. and D. C. Chapman, 1997: A simple theory for the fate of buoyant coastal discharges. *Journal of Physical Oceanography*, 27, 1386-1401.

CHAPTER 2: NUMERICAL INVESTIGATION OF THE MIDDLE ATLANTIC  
BIGHT SHELFBREAK FRONTAL CIRCULATION USING A HIGH-RESOLUTION  
OCEAN HINDCAST MODEL<sup>1</sup>

Ke Chen and Ruoying He

Department of Marine Earth and Atmospheric Sciences, North Carolina State University

---

<sup>1</sup> This chapter is published in *Journal of Physical Oceanography*, DOI: 10.1175/2009JPO4262.1

## **Abstract**

A nested high-resolution ocean model is used to hindcast the Middle Atlantic Bight (MAB) shelfbreak circulation from December 2003 to June 2008. The model is driven by tidal harmonics, realistic atmospheric forcing, and dynamically consistent initial and open boundary conditions obtained from the large-scale circulation model. Simulated shelfbreak sea levels and tracer fields compare favorably with satellite observations and available in-situ hydrographic climatology, demonstrating the utility of this nested ocean model for resolving the MAB shelfbreak circulation. The resulting time and space continuous hindcast solutions between January, 2004 and December, 2007 are used to describe the mean structures and temporal variations of the shelfbreak front and jet, the bottom boundary layer detachment, and the migrations of the shelfbreak front. It is found that the shelfbreak jet and boundary convergence reach their maximum intensities in the spring, at which time the foot of the front also migrates to its farthest offshore position. Vorticity analyses reveal that the magnitude ratio of the mean relative vorticity between the seaward and the shoreward portions of the shelfbreak front is about 2:1. The shelfbreak ageostrophic circulation is largely controlled by the viscosity in the boundary layers and by the nonlinear advection in the flow interior. Simulated three-dimensional velocity and tracer fields are used to estimate the transport, heat and salt fluxes across the 200 m isobath. Within the model domain, the total cross-shelf water transport, the total eddy heat flux and the total eddy salt flux are  $0.035 \pm 0.26$  Sv,  $1.0 \times 10^3 \pm 1.4 \times 10^4 W / m^2$ ,  $6.7 \times 10^{-5} \pm 7.0 \times 10^{-4} Kg / m^2 s$ . The Empirical Orthogonal Function (EOF) analysis on the 4-yr shelfbreak circulation hindcast solutions identifies two dominant modes. The first EOF mode accounts for 61% variance, confirming that the

shelfbreak jet is a persistent year-round circulation feature. The second mode accounts for 13% variance, representing the baroclinic eddy passages across the shelfbreak.

## **1. Introduction**

The shelfbreak front in the Middle Atlantic Bight (MAB) is the water mass boundary between the cold, fresh water on the MAB shelf and the warm, saline water of the Slope Sea. Associated with the front is a narrow shelfbreak jet, which has been estimated to transport approximately 0.2-0.3 sv of water equatorward south of the New England (*Linder and Gawarkiewicz, 1998*). This shelfbreak frontal jet is a part of the large-scale buoyancy driven coastal current system that originates from the Labrador Sea (*Chapman and Beardsley, 1989; Loder et al, 1998*). It exerts strong influence on the coastal environment in the northwest Atlantic, impacting cross-shelf exchanges of mass, heat, salt, the dispersion of coastal contaminants, and the nutrient supply to coastal ecosystems. For example, the shelfbreak front and jet are found to be important for many commercial fisheries because of the enhanced primary productivity associated with the front (e.g., *Marra et al., 1982, 1990; Ryan et al., 1999a, 1999b*).

Understanding the shelfbreak frontal dynamics has been the major topic of numerous earlier studies. Hydrographic surveys by *Beardsley and Flagg (1976)* and *Burrage and Garvine (1988)* provided synoptic snapshots that generally describe the thermocline structure of the front. Long-term mooring arrays, such as the Nantucket Shoals Flux Experiment (NSFE) (*Beardsley et al., 1985*), the Shelf Edge Exchange Process (SEEP) Experiment (*Aikman, 1988; Houghton et al., 1988*) and SEEP II Experiment (*Houghton et al., 1994; Flagg et al., 1994*) addressed the long-term statistics

of the velocity and temperature structure of the front. By area-averaging long-term hydrographic data, *Linder and Gawarkiewicz (1998)* offered climatological mean conditions of MAB shelfbreak frontal structures, the migration of the front bottom foot, and the associated geostrophic velocity fields. More recently, *Fratantoni et al. (2001)* studied the structure of shelfbreak jet based on two-year (1995 -1997) ADCP surveys. While providing many valuable insights on the shelfbreak frontal dynamics, these results are still limited by temporal and spatial resolutions and are subjected to the question how representative they are in describing the shelfbreak circulation dynamics. In particular, work including *Garvine et al., (1988)*, *Lozier et al., (2002)* and *Gawarkiewicz et al. (2004)* showed that frontal instabilities and shelf-slope interactions are reoccurring features with fine temporal and spatial scales as small as 1-2 day and 8-15km, respectively. Improved understanding of the MAB shelfbreak circulation and better quantification of its variations therefore require high-resolution, space and time continuous realizations of ocean state variables, from which detailed dynamics can be gleaned.

In this study, we approach this problem through a realistic circulation hindcast experiment. We will examine whether a high resolution, nested circulation model, driven by a complete suite of forcing functions, can reproduce known features of the MAB shelfbreak circulation. Unless the model gets the mean states of shelfbreak circulation correct, it is questionable that one can use the model to exam the high-frequency variability associated with the shelfbreak frontal circulation.

We start in Section 2 with a description of the shelfbreak ocean model utilized in this research. Section 3 presents model-data comparisons, the structures of simulated mean shelfbreak front and jet, and their temporal variations. More in-depth dynamical

analysis and cross-shelf transport and flux estimates are presented in Section 4, followed by the discussion and summary in Section 5.

## 2. Model

Our high resolution shelfbreak simulation was performed with the Regional Ocean Modeling System (ROMS), a free surface, hydrostatic, primitive-equation model. ROMS employs split-explicit separation of fast barotropic and slow baroclinic modes, and is formulated in vertically stretched terrain-following coordinates using algorithms described in details by *Shchepetkin and McWilliams* (2005). The ROMS computational kernel includes high-order advection and time-stepping schemes, weighted temporal averaging of the barotropic mode to reduce aliasing into the slow baroclinic motions, and conservative parabolic splines for vertical discretization. A redefinition of the barotropic pressure-gradient term is also applied in ROMS to reduce the pressure-gradient truncation error, which has previously limited the accuracy of terrain-following coordinate models (*Shchepetkin and McWilliams, 2005*).

The model domain encompasses the shelfbreak region offshore of Nantucket shoals in the northeast and Hudson Canyon in the southwest (**Figure 1**). Within the domain, the water depth ranges from 30 m to 3000 m. The model's horizontal resolution is 1 km. Vertically, there are 36 terrain-following levels in the water column with higher resolution near the surface and bottom to better resolve ocean boundary layers. The minimum (maximum) model vertical spacing is 0.8 m (211 m) in the boundary layer (the mid- water column).

## 2.1. Open boundary and Initial Conditions

To specify open boundary conditions for this shelfbreak model, we nested it inside the MABGOM (Middle Atlantic Bight and Gulf of Maine) ROMS described and validated by *He and Chen* (submitted). The MABGOM model itself was nested in the global circulation simulation provided by HyCOM/NCODA (Hybrid Coordinate Ocean Model together with NRL Coupled Ocean Data Assimilation scheme, *Chassignet et al.*, 2006). A one-way nesting approach was adopted in this setup to connect the ‘parent model’ (MABGOM ROMS) with the ‘child model’ (shelfbreak ROMS). Specifically, open boundary conditions (OBCs) were applied to tracers and baroclinic velocity following the method of *Marchesiello et al.* (2001), whereby Orlandi-type radiation conditions were used in conjunction with relaxation (with timescale of 0.5 days on inflow and 10 days on outflow) to MABGOM solutions. Free surface and depth-averaged velocity boundary conditions were specified using the method of *Flather* (1976) with the external subtidal values defined by MABGOM ROMS, plus  $M_2$  tidal harmonics from an ADCIRC (ADVANCED CIRCULATION MODEL FOR OCEANIC, COASTAL AND ESTUARINE WATERS) tidal simulation of the western Atlantic (*Luetich et al.* 1992). The latter  $M_2$  information provides needed tidal mixing, which is an important element of the regional circulation (*He and Wilkin*, 2006). We applied the method of *Mellor and Yamada* (1982) to compute vertical turbulent mixing, as well as the quadratic drag formulation for the bottom friction specification. Major advantages of this nesting configuration include: 1) it allows the “child model” to incorporate the upstream and deep-ocean forcing in a dynamically consistent and quantitatively accurate manner; and 2)

the higher resolution enables the shelfbreak ROMS to better resolve the frontal circulation dynamics underpinned in this research.

## 2.2. Surface Forcing

We utilized surface forcing from NOAA NCEP North America Regional Reanalysis (NARR), which has the spatial and temporal resolutions of 35-km and 3 hourly, respectively. Air-sea fluxes of momentum and buoyancy were computed by applying the standard bulk formulae (*Fairall et al. 2003*) to NARR marine boundary-layer winds, air temperature, relative humidity, air pressure, along with ROMS generated surface current. To further constrain the spatial pattern of the net surface heat flux, we implemented a thermal relaxation term following *He and Weisberg (2002)*, such that

$$K_H \frac{\partial T}{\partial Z} = \frac{Q}{\rho C_p} + c(T_{obs} - T_{mod}) \quad (1)$$

where  $K_H$  is the vertical eddy diffusivity,  $Q$  is the net surface heat flux,  $\rho$  and  $C_p$  are the water density and specific heat capacity.  $c = 0.5 \text{ day}^{-1}$ , and  $T_{obs}$  is the daily, blended cloud-free surface temperature field generated by NOAA Coast Watch.

The shelfbreak ROMS hindcast ran continuously from December, 2003 through January, 2008. Initial conditions were taken from the MABGOM ROMS simulation on December 1<sup>st</sup>, 2003.

### 3. Results

Standard circulation state variables (sea level, currents, temperature, and salinity) were archived at the daily interval. For model validations and analyses described below, we concentrated on the simulation over the period from January 1, 2004 to December 31, 2007. Limited by scarce shelfbreak in-situ observations, we used satellite observations and hydrographic climatology to gauge the model's performance.

#### 3.1. Model Data Comparisons

##### A. Sea Surface height comparison

Satellite altimeter data provide a useful means to examine the model's skill in reproducing sea surface height distribution. For the model validation purpose, we obtained  $1/3^\circ \times 1/3^\circ$  along-track SSHA product from French Group Archiving, Validation of Satellite Oceanographic Data [AVISO] (*Rio and Hernandez, 2004*). There are three satellite tracks inside our shelfbreak model domain. Among them, we focus on a cross-shelf track that is nearly aligned with the earlier PRIMER section (*Fratantoni et al., 2001*). Because that the along-track satellite data are only available every 9 days; we sampled our simulated subtidal sea surface height anomaly (SSHA) at the same time when altimeter observations were available.

The Hovmoller diagram of observed SSHA shows the sea levels along this cross-shelf transect are the highest (lowest) during the fall (spring) season (upper panel, **Figure2**). The observed absolute surface height variation is up to 0.25 m, which is a result of the combined effects of surface heating and horizontal advection. Such sea level responses were generally reproduced by the shelfbreak model. While the model is

missing some of the fine-scale sea level structures, it captures the seasonal and interannual variability reasonably well. Statistically, the overall correlation coefficient between simulated and observed SSHA is 0.53 with the 95% confidence level. The spectra comparison (lower panel, **Figure 2**) shows that the model reproduces observed annual cycle and other high frequency variations. We note because the altimeter data are only available every 9 days, some high frequency variability relevant to the MAB shelfbreak circulation are either aliased or not resolvable by satellite altimeter.

### *B. Shelfbreak hydrography comparison*

We next sampled the mean temperature and salinity along the Nantucket transect (see Figure 1) and compared them with early climatology averaged by *Linder and Gawarkiewicz* (1998) for the similar segment of the MAB shelfbreak. The Nantucket transect is nearly perpendicular to the local isobath, so the choice of this transect also allows us to directly examine the shelfbreak jet and its along-shelf transport. To be consistent with the *Linder and Gawarkiewicz* climatology, simulated bi-monthly mean temperature and salinity fields were averaged based on the 4-year hindcast solutions.

The bimonthly mean temperature fields (**Figure 3**) exhibit strong seasonal variability. During winter months (December to March), surface cooling together with enhanced mixing by convective overturning and storm events keep shelf waters weakly stratified. The thermocline starts to develop as the season progresses. By the spring to summer time (April to July), a strong thermocline has established, separating the warm upper layer from the cold bottom water. The latter becomes the so called MAB “cold pool” described by *Beardsley and Flagg* (1976) and *Houghton et al.*, (1982), among other

studies. Further offshore, both observation and simulation show an abrupt horizontal temperature gradient at the shelfbreak, known as the “shelfbreak front”. In fall (August-November), the shelf waters transition from vertically stratified to horizontally stratified. As a result, the shelfbreak temperature front becomes less pronounced by this time compared to its spring and summer conditions. The bimonthly salinity fields (**Figure 4**) exhibit relatively weaker seasonal variability. Unlike the temperature, both the simulation and observation show the shelfbreak salinity front is a persistent feature throughout the year, with a gradient of 1-2 psu difference over 10-20 km. We note the simulated mean temperature and salinity fields reported here are based on the 4-year shelfbreak hindcast, while the *Linder and Gawarkiewicz* climatology was produced by a time and space averaging of hydrographic data collected in the vicinity of MAB shelfbreak over nearly 100 years. Despite differences in the time span, and the temporal and spatial resolutions between the two, it is encouraging to see that the regional shelfbreak model is capable of reproducing essential features of shelfbreak temperature and salinity, and their respective seasonal evolutions. These general agreements verify the utility of the model, lending confidence for using its hindcast solutions to study the shelfbreak circulation dynamics.

### *C. Decorrelation scale comparison*

Based on ship observations in July 1996, *Gawarkiewicz et al.* (2004) provided a set of decorrelation scale estimations for the MAB shelfbreak circulation. While our model hindcast period did not include the year of 1996, we calculated the decorrelation scale using simulated circulation fields in July 2006, and made comparisons with their observational counterparts (Table 1). Depending on the state variable being examined, the

observation based analysis shows the decorrelation scale varies from 7 to 20 km. Our model based analyses are consistently larger (varying from 12 to 22 km) than those inferred from observations, but certainly in the comparable ranges. The shelfbreak circulation fields in July 1996 and July 2006 would be quite different, but the intrinsic dynamic scales of the system are expected to be similar. The general agreement between the observed and simulated scales suggests the shelfbreak ROMS can indeed capture the essential features of the MAB shelfbreak circulation.

### 3.2. Model Analysis

We next use the high-resolution, space and time continuous hindcast solutions to characterize the MAB shelfbreak jet and frontal structures along the Nantucket transect.

#### *A. Mean shelfbreak frontal structures*

First we concentrated on the structures of mean temperature, salinity, along and across- shelf velocity fields (**Figure 5**), each obtained by temporally averaging their respective solutions from January 1<sup>st</sup>, 2004 to December 31<sup>st</sup>, 2007.

The mean temperature field highlights the co-existence of the “cold pool” on the shelf and the temperature front at the shelf break. Within the “cold pool” area, the bottom water is about 4-5 °C cooler than the surface water. At the shelfbreak, the upward tilted temperature front extends from the bottom to 20 m below the surface. A similar shelfbreak frontal structure is also seen in the mean salinity field. However the salinity front extends all the way to the surface, presenting a clearer surface signature than does the temperature front.

The mean alongshore velocity transect shows the shelfbreak circulation consists of an equatorward shelfbreak jet and a near bottom poleward current, a structure consistent with the finding of *Flagg et al* (2006). Further examinations (not shown) indicate this near bottom flow reversal is a local feature that can be explained by the thermal wind balance described by *Chapman and Lentz* (1994). In the summer however, this locally generated flow merges with the poleward slope current, resulting in an enhanced northward transport in the Slope Sea.

The shelfbreak jet moves at  $0.1 \text{ ms}^{-1}$ , with the majority of its flow trapped within the upper 70 m. Consistent with findings of earlier studies (*Gawarkiewicz et al.*, 2004; *Fratantoni et al.*, 2001), the jet core is located at the shoreward side of the shelfbreak front. The e-folding scales are 50-m and 30-km for the shelf-jet depth and width respectively. The resulting along-jet transport is 0.42 Sv, a value comparable with previous estimates (*Beardsley et al*, 1985; *Linder and Gawarkiewicz*, 1998; *Fratantoni et al.*, 2001). The cross-shelf mean velocity exhibits a layered -structure similar to what was discussed by *Lentz* (2008). It has a seaward moving surface flow ( the upper 25 m), a shoreward moving interior flow, which is underlaid by another weak seaward moving flow near the bottom. It should be noted that the 4-year temporal averaging may smooth out small-scale frontal structures that may otherwise be observed in the synoptic in-situ surveys. We will examine the small scale variability in details in a future correspondence.

#### *B. Bimonthly mean shelfbreak jet structures*

To quantify the temporal variations of the shelfbreak jet associated with the bi-monthly hydrography presented in 3.1, we computed bi-monthly velocity means (**Figure**

6). In December and January, the shelfbreak jet is surface trapped within a thin (<50 m) but broad (> 20 km) upper layer. The poleward slope current is largely absent at this time of the year. Consequently, the equatorward shelfbreak currents transport a volume of 0.72 Sv to the south, the largest value throughout the year. The shelfbreak jet then weakens in February and March, with the core of the jet shifting offshore. This is accompanied by an onshore motion of the slope current. Transports of these two currents counteract each other, resulting in a net equatorward transport of only 64% of its winter value. In April – May, the shelfbreak jet gets stronger with the core of jet confined to within a few km shoreward of the shelfbreak. The jet speed reaches its annual maximum  $0.3 \text{ ms}^{-1}$ , a value that is consistent with the observation of *Fratantoni et al.* (2001). The slope current seaward of the shelfbreak is similarly intensified, but to a less extent. Consequently, the net equatorward transport is 0.62 sv, the second highest value of the year. Starting in Jun/Jul, the jet begins to weaken with its core moving onshore and deepening. The maximum velocity now decreases to  $0.1 \text{ ms}^{-1}$ . These changes are in response to shelf water destratification associated with enhanced cooling and mixing, leading to a weakened across-shelf density gradient (e.g., Figure 3). By October and November, the shelfbreak jet structure is less clear. Counteracted by the enhanced poleward slope current, the net equatorward transport now reaches its minimum value of the year.

### *C. Bimonthly mean bottom boundary layer detachment*

An important feature of the MAB shelfbreak circulation is the convergent flow near the bottom of the shelfbreak front and its related bottom boundary layer (BBL) detachment process (*Gawarkiewicz and Chapman, 1992; Chapman and Lentz, 1994;*

*Barth et al., 1998; Pickart, 2000; Linder et al., 2004*). *Pickart (2000)* showed a useful means to quantify such BBL detachment is through the Accumulated Property Change (APC) calculation. The basic idea is that upwelling along the isopycnal layer in which the detachment is occurring should result in a weaker water property. Hence by computing the accumulated theta change (ATC) along tilted isopycnals in a cross front transect and tracking tongues of low ATC, one can assess the intensity of bottom boundary layer detachment. Following this idea, we computed water density and its associated ATC using bimonthly temperature and salinity fields. The resulting bi-monthly shelfbreak ATC fields (**Figure 7**) indicate that bottom convergence is indeed a discernable feature in the winter, spring, and summer seasons with its intensity proportional to the degree of isopycnal tilting. That is, larger BBL convergences are observed when the isopycnals are more steeply tilted at the shelfbreak.

No significant ATC tongue structure is identified in the fall when isopycnals are relatively flat, suggesting a shutdown of the BBL convergence. We note findings here are consistent with *Linder et al. (2004)* BBL discussion. One caveat is that the present ATC calculations are based on the bimonthly mean tracer fields. A more rigorous quantification of the BBL detachment and shelfbreak upwelling rate estimation would require a more focused case study using instantaneous 3-dimensional tracer and circulation fields. This is an ongoing effort that we will report in a future correspondence.

#### *D. Cross-shelf migration of shelfbreak front*

Following *Beardsley and Flagg (1976)* and *Linder and Gawarkiewicz (1998)*, we investigated spatial variations of the foot of the front, using the 34.5 isohaline to define

the front boundary (left panel, **Figure 8**). In general, the 34.5 isohaline tilts upward. Consistent with our earlier discussion, the largest tilting angle occurs in the spring season, when the maximum speed of baroclinic shelfbreak jet occurs. Throughout the year, the monthly mean foot position migrates between 80 m and 150 m isobaths, which translates into a horizontal displacement of 15~20 km. In terms of the water depth of the frontal foot, the monthly position histogram (right panel, **Figure 8**) indicates the front moves to its farthest onshore position in the winter (November and December), and its farthest offshore position in the spring (April and May), respectively. Consistent with finding of *Linder and Gawarkiewicz (1998)*, results here suggest that in-situ samplings of the shelf break front would require a sufficient spatial coverage to resolve variations of the front. While the seasonal excursions of 15~20 km is roughly the same order of magnitude as the width of shelfbreak jet, the front still remains close to the shelf break. *Chapman (2000)* shows the front does not adjust much differently to the presence or absence of the shelfbreak topography. The mechanisms for such a frontal trapping remain to be better understood.

## 4. Discussion

### 4.1. Vorticity and momentum balance

Based on the mean shelfbreak circulation fields, we can compute the relative vorticity ( $\zeta$ )  $\frac{\partial v}{\partial x} - \frac{\partial u}{\partial y}$  along the Nantucket transect (left panel, **Figure 9**). The resulting mean vorticity field, scaled by the local Coriolis parameter, gives the Rossby number  $R_o = \zeta / f$ . Seaward of the shelfbreak jet  $R_o$  is positive with a maximum value of

0.15. Shoreward of the jet,  $R_o$  is negative with a value approaching -0.07. The result here compares favorably with the observational based vorticity calculation reported by *Fratantoni et al.* (2001) [right panel, **Figure 9**]. It is also in agreement with *Gawarkiewicz et al.* (2001) showing the absolute ratio of relative vorticity is about 2:1 between the seaward and the shoreward portions of the front. A further investigation on the relative vorticity in this fixed coordinates indicates that  $\partial v/\partial x$ ,  $-\partial u/\partial y$  term each accounts for nearly 50% of the relative vorticity. On synoptic scales (not shown), the relative vorticity of the simulated jet shows a very wide range, varying from  $-0.78 f$  to  $2.3 f$ . Examinations of the mean shelfbreak circulation (Figure 5) indicate the presence of poleward slope current induces a large velocity shear, contributing to a stronger cyclonic circulation seaward of the shelfbreak. The consistency between observed and simulated vorticity fields further confirms that the shelfbreak model captures the essence of shelfbreak circulation dynamics.

Term-by-term momentum analysis offers additional insights on the shelfbreak circulation. By examining the relative importance of the local rate of change, the Coriolis force, the horizontal pressure gradient force, horizontal and vertical advection terms, and the horizontal and vertical viscosity terms, one can identify key balances dominating the shelfbreak circulation structure. We focus on the mean momentum balance in the cross-shelf direction (**Figure 10**). As expected, both the Coriolis force and pressure gradient force are the leading (an order of magnitude larger than others) terms and together they constitute the geostrophic balance. Indeed, the shelfbreak jet and the poleward moving slope current are to the first order geostrophic flows. The residual of Coriolis force plus pressure gradient force leads to the ageostrophic circulation. The ageostrophic momentum

is balanced largely by the frictional viscosity in the surface and bottom boundary layers. The residual of those two is further balanced by the nonlinear advection presented primarily in the flow interior. The sum of ageostrophic momentum, viscosity and advection terms gives rise to the local rate of change of the mean across-shelf velocity (last panel in Figure 10), which is of four orders of magnitudes smaller than the Coriolis force. In reality, we expect the local rate of change of the shelfbreak circulation at any given time to be a significantly large number due to the transitory nature of the system (e.g., *Lozier et al.*, 2002). Therefore a large number of snapshots would have to be ensembled to produce a steady state mean field. The fact that the simulated local rate of change term is very small suggests that the temporal averaging of 4 years of daily model output fields produces a credible representation of the mean state of the shelfbreak circulation.

#### 4.2. Cross shelf transport and flux

Quantifying the slope/shelf water mass and flux exchanges has been a longstanding research problem in the MAB (*Beardsley and Boicourt*, 1981; *Lorder et al.*, 1998; *Lozier and Gawarkiewicz.*, 2001; *Fratantoni et al.*, 2001; *Gawarkiewicz et al.*, 2004). Here, we approach this problem by using simulated circulation fields. To do that, we followed *He and Chen* (submitted) by selecting the 200 m isobath as the shelf-slope boundary and compute the cross-shelf water mass transport. Simulated 3-dimensional velocity fields were first rotated into normal and tangential components relative to the local orientations of the 200 m isobath. The resulting normal component of velocity  $U_N$

was then integrated with local depth  $Z$  and along-isobath length  $S$  to yield the volume transport value according to:

$$Q = \int_0^{s_0} \int_{-H}^{\eta} u_N(s, z) ds dz \dots\dots\dots(2)$$

where  $S_0$  is the along-isobath distance. This calculation reveals that across the 200-m isobath within the shelfbreak model domain, the total transport is  $0.035 \pm 0.26$  sv. It is worth noting that the standard deviation of such transport is an order of magnitude larger than the mean, indicating that across-shelfbreak mass exchange is highly variable. We also note that the meander of the jet can induce large fluctuations in the cross-shelf transport. Thus it is prudent to state that the value above does not necessarily imply the net shelf/ deep-ocean exchange.

The spatial distribution of such variability is examined in **Figure 11**. In general, the mean transport near the Nantucket Shoal (0-100km along isobath) is weakly onshore. Immediately downstream (100-200 km), the mean transport becomes weakly offshore with a value of  $\sim 0.002$  Sv. The overall variations over these two segments are both relatively small. Fluctuations in the transport values become larger approaching Hudson Canyon off New York (200-300 km). Here, the standard deviations range from -0.02 to 0.02 sv, which are likely related to topographic steering by abrupt bathymetric changes and eddy activities often observed in this area.

The cross-shelf eddy flux of any quantity  $\phi$  can be estimated by the method proposed by *Garvine et al. (1989)*, such that

$$F(z) = \frac{1}{\Delta z \Delta x} \int_{z-\frac{\Delta z}{2}}^{z+\frac{\Delta z}{2}} \int_{x_1}^{x_2} \Phi(x, z_1) dx dz_1 \quad (3)$$

For the heat flux, we defined,

$$\Phi = \rho C_p (T - T_m)(v - v_m) \quad (4)$$

For the salt flux, we defined:

$$\Phi = \frac{\rho}{1000} (S - S_m)(v - v_m) \quad (5)$$

where  $\rho$  is water density and  $C_p$ , the seawater specific heat, and  $S$ ,  $T$ ,  $v$  are the salinity, temperature and cross-shelf velocity, respectively. The variables with subscript  $m$  indicate the temporal mean values along the 200 m isobath within the shelfbreak model domain.

We found the 4-yr mean eddy heat flux is shoreward at  $1.0 \times 10^3 \pm 1.4 \times 10^4 W / m^2$ , indicating on average the slope sea is acting as the source of heat for the shelf waters. Depending on the local and deep-ocean forcing conditions, individual monthly eddy heat flux ranges from  $4.8 \times 10^4 W / m^2$  (shoreward) in May 2004 to  $-3.0 \times 10^4 W / m^2$  (seaward) in October 2004. Further investigations into the seasonal trend of the total cross-shelf eddy heat flux (not shown) indicate that the heat flux tends to be onshore during the winter and spring seasons and offshore during summer and fall seasons.

The mean eddy salt flux is found to be shoreward at  $6.7 \times 10^{-5} \pm 7.0 \times 10^{-4} Kg / m^2 s$ . Over the 4 years, the largest onshore flux ( $0.0026 Kg / m^2 s$ ) occurred in May 2004, and the largest offshore flux ( $-0.0011 Kg / m^2 s$ ) occurred in October 2004. This model based mean salt flux value is consistent with *Gawarkiewicz et al (2004)* with regards to its

onshore transport direction. However, the magnitude is one to two orders of magnitude smaller than earlier observational estimates (e.g., *Gawarkiewicz et al.*; 2004; *Garvine et al.*, 1989), which were based on either single point measurement or some limited ship transects for a short time period. Aside the temporal averaging in our flux calculation that may have smoothed the variability, differences in sampling locations and durations between the simulation and observations also contribute to the magnitude difference.

#### 4.3. Dominant Modes of shelfbreak jet

While the focus of this study is on the mean state of the MAB shelfbreak frontal circulation, we can assess the dominant modes and temporal variability of the front and jet by applying an Empirical Orthogonal Function (EOF) analysis to the simulated current fields along the Nantucket transect. Because along-shelf and cross-shelf velocity fields are dynamically connected, a bi-variant EOF method (*He et al.*, 2005) that concurrently considers both  $u$  and  $v$  velocity components was adopted. Specifically, the data matrix  $A$  was defined as:

$$A = \begin{pmatrix} u \\ v \end{pmatrix} \quad (6)$$

The EOF decomposition of  $A$  gives

$$A(x, z, t) = \sum_{n=1}^N a_n(t) F_n(x, z) \quad (7)$$

where  $a_n$  and  $F_n(x, z)$  are the temporal evolution functions (principle components) and spatial eigenfunctions (EOF) of each mode, respectively.

The first EOF mode accounts for 62% of variance (**Figure 12**). As expected, the along-shelf velocity mode highlights the existence of the shelfbreak jet. The jet is located shoreward of the shelfbreak. It is surface trapped with a characteristic width of about 40-60 km. The spatial mode of the across-shelf velocity again reveals a layered vertical structure, which consists of a shoreward flow in the interior and seaward flows in both surface and bottom boundary layers. The principle component (PC1) of the 1<sup>st</sup> EOF mode is almost entirely positive, suggesting the equatorward shelfbreak jet and layer-structured cross-shelf flow patterns are persistent shelfbreak circulation features. PC1 also reveals that some short-duration flow reversals do occur sporadically, which are presumably related to strong atmospheric forcing and frontal instability (*Fratantoni and Pickart, 2003*). Overall, larger PC1 values occur during late winter and spring seasons. Consistent with our early discussion (3.2.B), they imply that the shelfbreak jet reaches its maximum intensity during these times.

The second EOF mode accounts for 13% of total variance. Interestingly, this mode displays contrasting flow patterns between the shelf and the slope in along-shelf direction. The cross-shelf component is surface intensified and negative throughout the entire water column. The 2<sup>nd</sup> principle component (PC2) suggests that this mode is associated with significant temporal variability that changes signs of spatial mode. Overall, this mode seems to be related to the baroclinic eddy passages across the shelfbreak. The positive PC2 indicates cyclonic eddies translating shoreward; whereas the negative PC2 corresponds to anticyclonic eddies translating seaward. Generation of baroclinic eddies are subject to large-scale surface and deep-ocean forcing conditions, and the flow interaction with the bottom topography. While no clear seasonal cycle is found,

the frequency spectra calculation (not shown) on the PC2 show the energy peaks at the periods of 71, 163, and 203 days, respectively. With some 25% of the variance remaining in higher modes a reconstruction of the shelfbreak circulation to account for its high frequency responses would require several more modes.

## 5. Summary

A1-km resolution regional circulation model was developed to hindcast the MAB shelfbreak circulation from December 2003 to June 2008. The model considered realistic atmospheric and tidal forcing. Its subtidal open boundary conditions were specified via one-way nesting with an existing shelf-wide MABGOM circulation simulation by *He and Chen*, (submitted). Hindcast solutions were compared with satellite altimeter data, hydrographic climatology for the MAB shelfbreak, and observational based decorrelation scale estimations. General agreements were found, indicating this shelfbreak circulation model is capable of capturing essential dynamics of the MAB shelfbreak circulation. As we focused on the mean structures of the shelfbreak current and hydrography in this study, time and space continuous circulation hindcast fields from January, 2004 to December 2007 were used to construct the temporal means and bimonthly averages of shelfbreak ocean states.

Our analysis showed that the MAB shelfbreak jet is a year-around, surface intensified flow. On the average, it has characteristic width and trapping depth of 60 km and 100 m, respectively, transporting 0.42 Sv equatorward. The jet reaches its maximum speed ( $0.3 \text{ ms}^{-1}$ ) in the spring, when the shelfbreak temperature and salinity fronts fully develop. Throughout the year, the bottom foot of the shelfbreak front migrates between

80m to 150m isobaths, reaching its farthest offshore (onshore) position in April and May (November and December). The accumulated theta change (ATC) calculation within shelfbreak isopycnals suggests the bottom boundary layer detachment is most significant during winter and spring seasons.

The relative vorticity analysis indicates the larger velocity shear exists seaward of the shelfbreak, and that the vorticity ratio is roughly 2:1 between the seaward portion and shoreward portion of the shelfbreak current. The geostrophy dominates the momentum balance of the shelfbreak jet. The viscosity in the boundary layers, along with the nonlinear advection in the interior play important roles in determining the ageostrophic flow. The cross-shelf volume transport, and its associated eddy heat and salt fluxes were estimated along the 200 m isobath within the model domain. These values are characterized by small means with large standard deviations, suggesting the shelf/slope exchanges across the MAB shelfbreak are highly variable. Indeed, the EOF analysis of the velocity fields along the Nantucket transect indicates that while the shelfbreak jet is the dominant mode, the structure and intensity of the current are subject to complex interactions between stratification, wind forcing, baroclinic instabilities and eddies. A better understanding of their roles in controlling the shelfbreak circulation dynamics can be further achieved in the future by focusing on synoptic scale events using the high-resolution shelfbreak model developed here. Clearly, deterministic predictions of the shelfbreak frontal circulation and its associated material property transport between the shelf and deep-ocean will also require advanced observational infrastructure together with sophisticated techniques for data assimilation (e.g., *He et al.*, 2005; *He and Wilkin*, 2006).

In that regard, the emerging MAB shelfbreak pioneer array, and the new in-situ observations it is about to collect, would be a great asset.

### **Acknowledgement**

Research support provided through ONR grant N00014-06-1-0739 and NASA grant NNX07AF62G are appreciated. We are indebted to G. Gawarkiewicz, D. McGillicuddy for their valuable discussions and suggestions throughout the course of this study. We also thank two anonymous reviewers for their insightful comments and suggestions.

## References

- Aikman, F. I., H. W. Ou, and R. W. Houghton, 1988: Current variability across the New England continental shelf-break and slope. *Continental Shelf Research*, 8, 625-651.
- Barth, J. A., D. Bogucki, S. D. Pierce, P. M. Kosro (1998), Secondary circulation associated with a shelfbreak front, *Geophys. Res. Letts*, 25, 15, 2761-2764.
- Beardsley, R. C. and C.N. Flagg, 1976: The water structure, mean currents, and shelf/slope water front on the New England continental shelf, *Mem Soc. R. Sci. Liege*, 6(X), 209-225.
- Beardsley, R. C. and W. C. Boicourt, 1981: On estuarine and continental-shelf circulation in the Middle Atlantic Bight. In B. A. Warren and C. Wunsch (editors): *Evolution of Physical Oceanography*. The MIT Press, Cambridge, Mass. pp. 198 - 233.
- Beardsley, R. C., D. C. Chapman, K. H. Brink, S. R. Ramp, and R. Schlitz, 1985: The Nantucket Shoals Flux Experiment (NSFE79).Part I: A basic description of the current and temperature variability. *J. Phys. Oceanogr.*, 15, 713–748.
- Burrage, D. M., and R. W. Garvine, 1988: Summertime hydrography at the shelfbreak front in the Middle Atlantic Bight, *J.Phys.Oceanogr.*,18,1309-1319.
- Chapman, D. C. and R. C. Beardsley, 1989: On the origin of shelf water in the Middle Atlantic Bight. *Journal of Physical Oceanography*, 19, 384-391.
- Chapman, D. C., and S. J. Lentz , 1994: Trapping of a coastal density front by the bottom boundary layer, *J. Phys. Oceanogr.*, 24, 1464– 1479.
- Chapman, D. C., 2000: Boundary Layer Control of Buoyant Coastal Currents and the Establishment of a Shelfbreak Front. *Journal of Physical Oceanography*, 30, 2941-2955.
- Chassignet, E. P., H. E. Hurlburt, O.M. Smedstad, G. R. Halliwell, P. J. Hogan, A. j. Wallcraft, R. Baraille, and R. Bleck , 2006: The HYCOM (Hybrid Coordinate Ocean Model) data assimilative system. *Journal of Marine Systems*, 65, 60-83.
- Fairall, C. W., E. F. Bradley, J. E. Hare, A. A. Garchev, and J. Edson, 2003: Bulk parameterization of air-sea fluxes: Updates and verification for the COARE algorithm. *Journal of Climate*, 16, 571-591.
- Flagg, C. N., R. W. Houghton, and L. J. Pietrafesa, 1994: Summertime thermocline salinity maximum intrusions in the Middle Atlantic Bight, *Deep Sea Res., Part II* ,41,325-340.
- Flagg, C. N., M. Dunn,D. Wang, H. T. Rossby,R. L. Benway, 2006: A study of the currents of the outer shelf and upper slope from a decade of shipboard ADCP observations in the Middle Atlantic Bight, 111, C06003, doi:10.1029/2005JC003116.
- Flather, R. A, 1976: A tidal model of the northwest European continental shelf, *Mem. Soc. R. Sci. Liege*, 6(10), 141-164.

- Fratantoni, P. S., R. S. Pickart., D. J. Torres, A. Scotti, 2001: Mean Structure and Dynamics of the Shelfbreak Jet in the Middle Atlantic Bight during Fall and Winter, *J. Phys. Oceanogr*, 31,2135-2156.
- Fratantoni, P.S., and R. S. Pickart, 2003: Variability of the shelf break jet in the Middle Atlantic Bight: Internally or externally forced?, *Journal of Geophysical Research*, 108, NO. C5, 3166,doi:10.1029/2002JC001326.
- Garvine, R., K. C. Wong, G. Gawarkiewicz, R. McCarthy, R. Houghton, and F. Aikman III ,1988: The morphology of shelf break eddies. *Journal of Geophysical Research*, 93, 15,593-15,607.
- Garvine, R. W., K. C. Wong, and G. G. Gawarkiewicz, 2001: Quantitative Properties of Shelfbreak Eddies. *Journal of Geophysical Research*, 94, 14475-14483.
- Gawarkiewicz, G. G., and D. C. Chapman, 1992: The role of stratification in the formation and maintenance of shelf-break fronts, *J. Phys. Oceanogr.*, 22, 753–772..
- Gawarkiewicz, G, F.Bahr, R.Bearsley, K.H.Brink, 2001: Interaction of a Slope Eddy with the Shelfbreak Front in the Middle Atlantic Bight, *Journal of Physical Oceanography*,31,2783-2796.
- Gawarkiewicz, G, K.H.Brink , R.Bearsley, M.Caruso, J.F.Lynch, C. Chiu, 2004: A large-amplitude meander of the shelfbreak front during summer south of New England: Observations from the Shelfbreak PRIMER experiment, *J. Geophys. Res.*,109,C03006, doi:10.1029/2002JC001468.
- He, R., McGillicuddy, D.J., Lynch, D.R., Smith, K.W., Stock, C.A., Manning, J.P., 2005: Data assimilative hindcast of the Gulf of Maine coastal circulation. *Journal of Geophysical Research*, 110, C10011, doi:10.1029/2004JC002807.
- He, R. and J. L. Wilkin, 2006: Barotropic tides on the southeast New England shelf: A view from a hybrid data assimilative modeling approach, *Journal of Geophysical Research*, 111, C08002, doi:10.1029/2005JC003254.
- He, R. and R. H. Weisberg , 2002: West Florida shelf circulation and temperature budget for the 1999 spring transition, *Continental Shelf Research*, 22, 719-748.
- He, R and K. Chen, Investigation of Northeastern North America Coastal Circulation Using a Regional Circulation Hindcast Model, *Journal of Geophysical Research*, submitted
- Houghton, R. W., R. Schlitz, R. C. Beardsley, B. Butman, and J. L. Chamberlin, 1982: The Middle Atlantic Bight cold pool: Evolution of the temperature structure in summer 1979, *J. Physc. Oceanogr.*, 12,1019-1029.
- Houghton, R. W., F. Aikman III, H.W.Ou, 1988: Shelf-slope water frontal structure, and cross-shelf exchange at the New England shelfbreak, *Cont.Shelf Res.*,8,687-710.

Houghton, R. W., C. N. Flagg, and L. J. Pietrafesa, 1994: Shelf-slope water frontal structure, motion, and eddy heat flux in the southern Middle Atlantic Bight, *Deep Sea Res., Part II*, 41,273-306.

Lentz, S.J., 2008: Observations and a Model of the Mean Circulation over the Middle Atlantic Bight Continental Shelf, *Journal of Physical Oceanography*, 38, 1203–1221.

Linder, C. A., and G. Gawarkiewicz, 1998: A climatology of the shelf break front in the Middle Atlantic Bight, *J. Geophys. Res.*, 103, 18,405– 18,423.

Linder, Christopher A., G. G. Gawarkiewicz, and R. S. Pickart, 2004: Seasonal characteristics of bottom boundary layer detachment at the shelfbreak front in the Middle Atlantic Bight. *Journal of Geophysical Research*, VOL. 109, C03049, doi:10.1029/2003JC002032, 2004.

Loder, J. W., B. Petrie, and G. Gawarkiewicz, 1998: The coastal ocean off northeastern North America: A large-scale view, in *The Sea, Vol. 11, The Global Coastal Ocean, Regional Studies and Syntheses*, edited by A. R. Robinson and K. H. Brink, pp. 105-133, Wiley, New York.

Lozier, M. Susan, and Glen Gawarkiewicz, 2001: Cross-frontal exchange in the Middle Atlantic Bight as evidenced by surface drifters. *Journal of Physical Oceanography*, 31(8), Part 2, 2498-2510.

Lozier, S., M. Reed and G. Gawarkiewicz, 2002: Linear stability of shelfbreak fronts. *Journal of Physical Oceanography*, 32(3), 924-944.

Luetlich, R.A. Jr., J.J. Westerink and N.W. Scheffner, November 1992: ADCIRC: An Advanced Three- Dimensional Circulation Model for Shelves, Coasts and Estuaries, Report 1: Theory and Methodology of ADCIRC-2DDI and ADCIRC-3DL, DRP Technical Report DRP-92-6, Department of the Army, US Army Corps of Engineers, Waterways Experiment Station, Vicksburg, MS., 137p.

Marchesiello, P., J. C. McWilliams, and A. F. Shchepetkin, 2001: Open boundary conditions for long-term integration of regional oceanic models. *Ocean Modelling*, 3, 1-20.

Marra, J., R. W. Houghton, D.C. Boardman, and P. J. Neale, 1982: Variability in surface chlorophyll a at a shelf-break front, *J. Mar. Res.*, 40, 575-591.

Marra, J., R. W. Houghton, and C. Garside, 1990: Phytoplankton growth at the shelf-break front in the Middle Atlantic Bight, *J. Mar. Res.*, 48, 851-868.

Mellor, G. L. and T. Yamada , 1982: Development of a turbulence closure model for geophysical fluid problems. *Review of Geophysics*, 20, 851-875..

Pickart, R. S., 2000: Bottom boundary layer structure and detachment in the shelfbreak jet of the Middle Atlantic Bight, *J. Phys. Oceanogr.*, 30, 2668– 2686.

Rio, M. H. and F. Hernandez, 2004: A mean dynamic topography computed over the world ocean from altimetry, in-situ measurements, and a geoid model, *Journal of Geophysical Research*, 109, c12032, doi: 10.1029/2003JC002226.

Ryan, J.P., J.A.Yorder, J.A.Bath, P.C. Cornillon. 1999: Chlorophyll enhancement and mixing associated with meanders of the shelf break front in the Mid-Atlantic Bight. *J. Geophys. Res.*, 104(C10), 23,479–23,493.

Ryan, J.P., J. A. Yoder, and P.C. Cornillon, 1999: Enhanced chlorophyll at the shelfbreak of the Mid-Atlantic Bight and Georges Bank during the spring transition. *Limnol. Oceanogr.*, 44(1), 1-11.

Shchepetkin, A.F., and J.C., McWilliams, 2005: The regional oceanic modeling system (ROMS): a split-explicit, free surface, topography-following-coordinate oceanic model. *Ocean Modelling*, 9, 347-404.

## Tables

Table 1. Comparisons of state variable de-correlation scales derived from in-situ survey in July 1996 (Gawarkiewicz et al. 2004, JGR) and from the shelfbreak model hindcast results in July 2006.

Variable (at ~54m)	Observation (July 1996)	Model (July 2006)
Temperature	7 km	12 km
Salinity	7-8 km	12 km
Density	20 km	16 km
U component velocity	11-12 km	22 km
V component velocity	12 km	20 km

## Figures

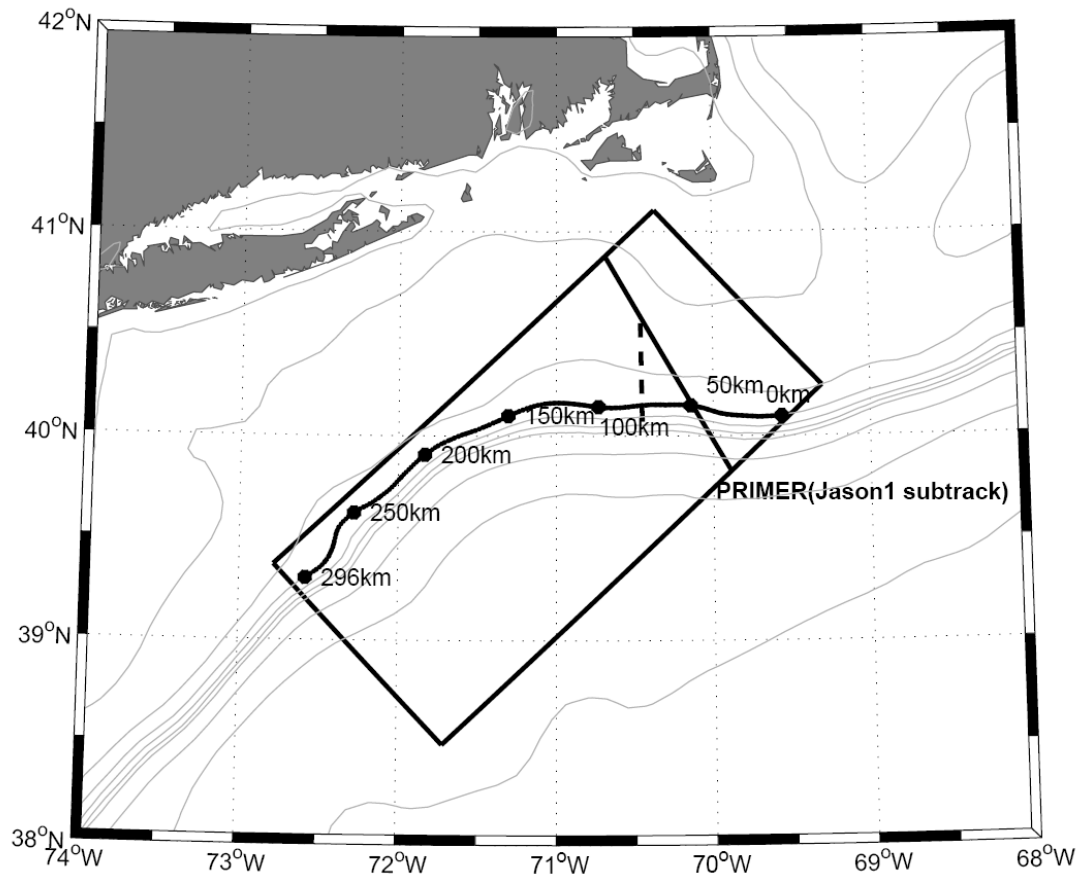


Figure 1. The high resolution shelfbreak model domain (box) and the location of Nantucket transect discussed in the manuscript (dashed line). Also shown is the satellite track (solid line), along which the sea surface height anomaly data were sampled. The curve and dots along the 200 m isobath and their associated numbers indicate the along-isobath distance downstream from the model's northeastern boundary.

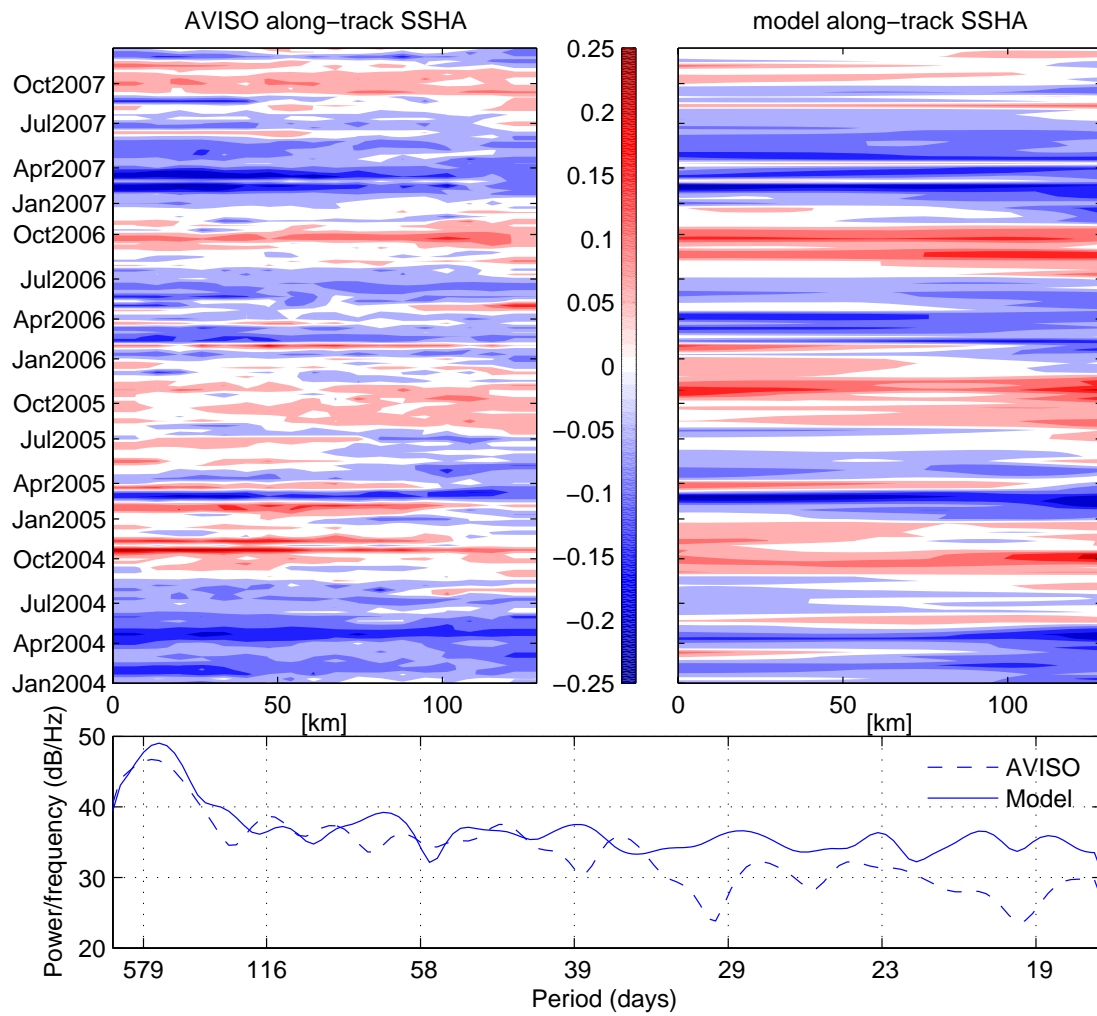


Figure 2. Hovmoller diagrams of satellite observed and model simulated sea surface height anomaly (SSHA) along the cross-shelf transect for the period from January 2004 to December 2007 (upper panels) and the comparison of spectra of satellite observed (dashed line) and model simulated (solid line) sea surface height anomaly in the MAB shelfbreak region (lower panel).

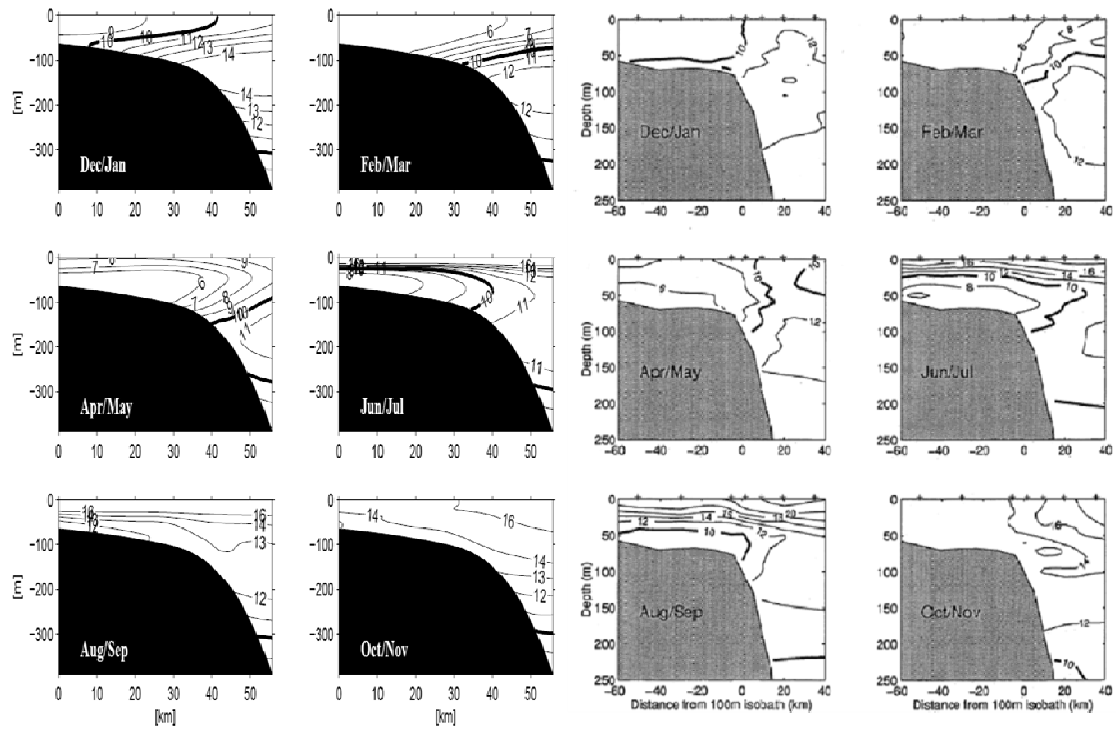


Figure 3. The bi-monthly mean temperature transect comparison between the model solutions (left panels) and the climatology (right panels) of *Linder and Gawarkiewicz (1998)*.

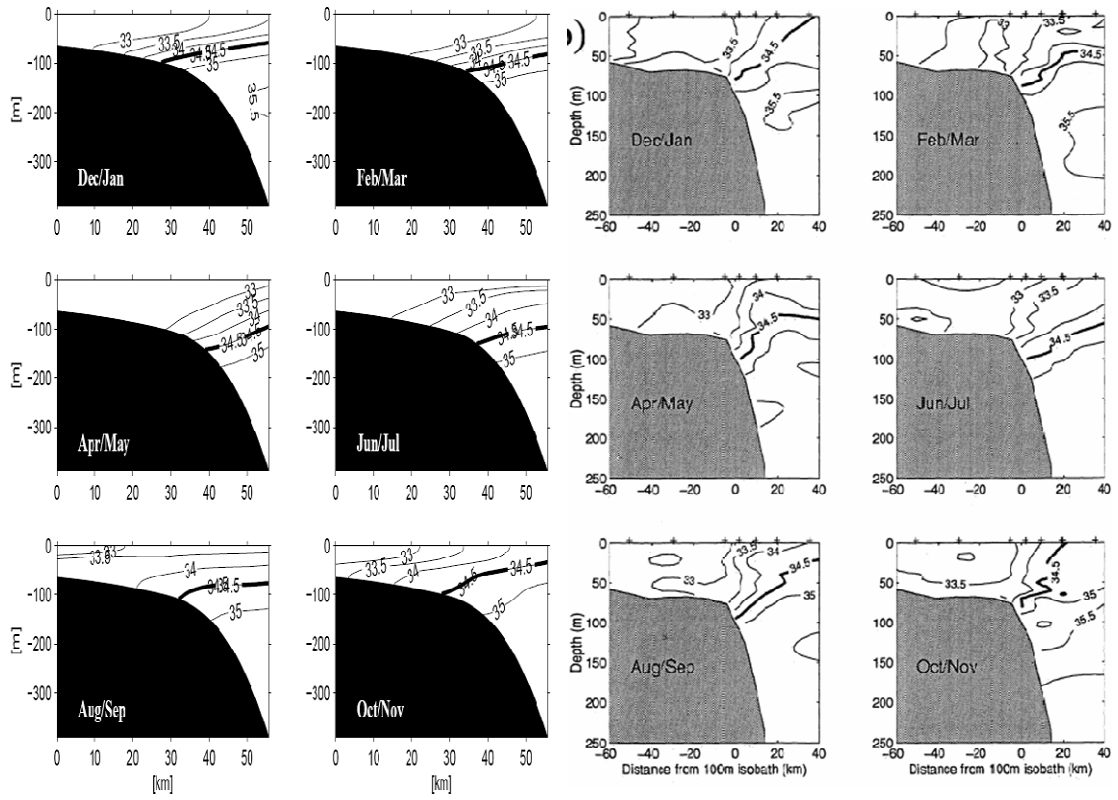


Figure 4. The bi-monthly mean salinity transects comparison between the model solutions (left panels) and the climatology (right panels) of *Linder and Gawarkiewicz (1998)*.

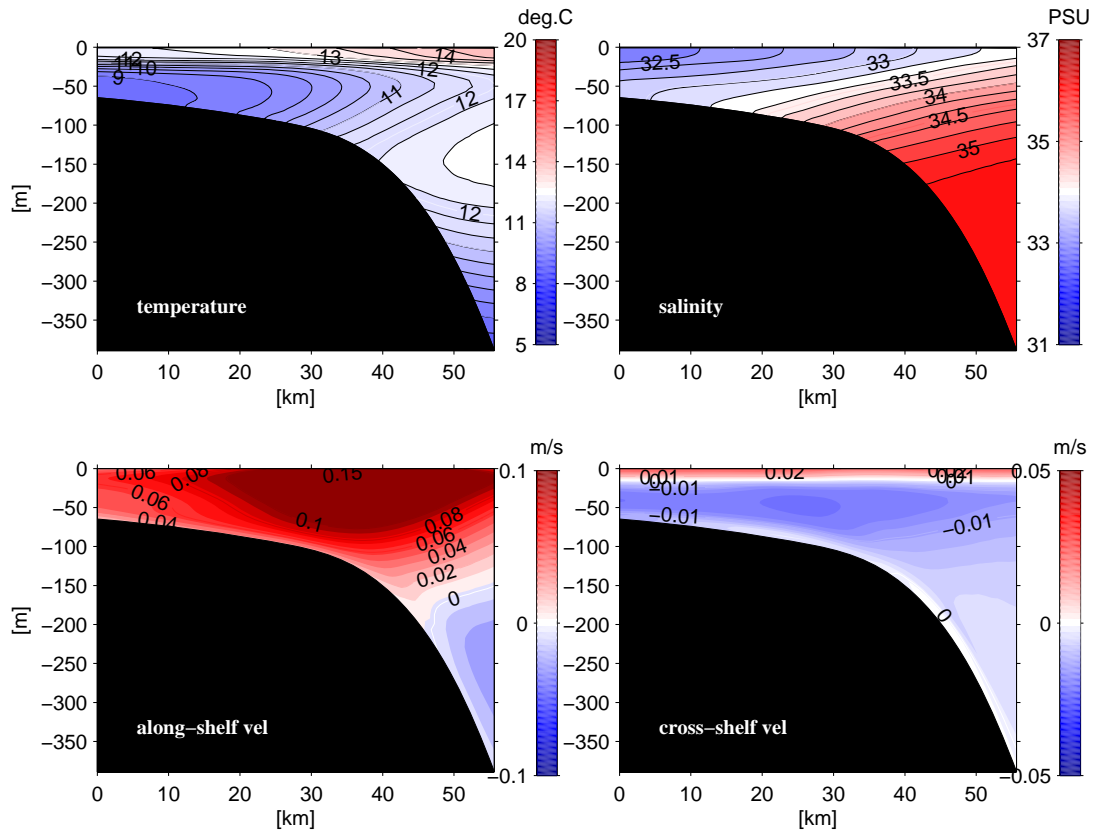


Figure 5. Model simulated mean temperature, salinity, along-shelf velocity and cross-shelf velocity fields along the Nantucket transect.

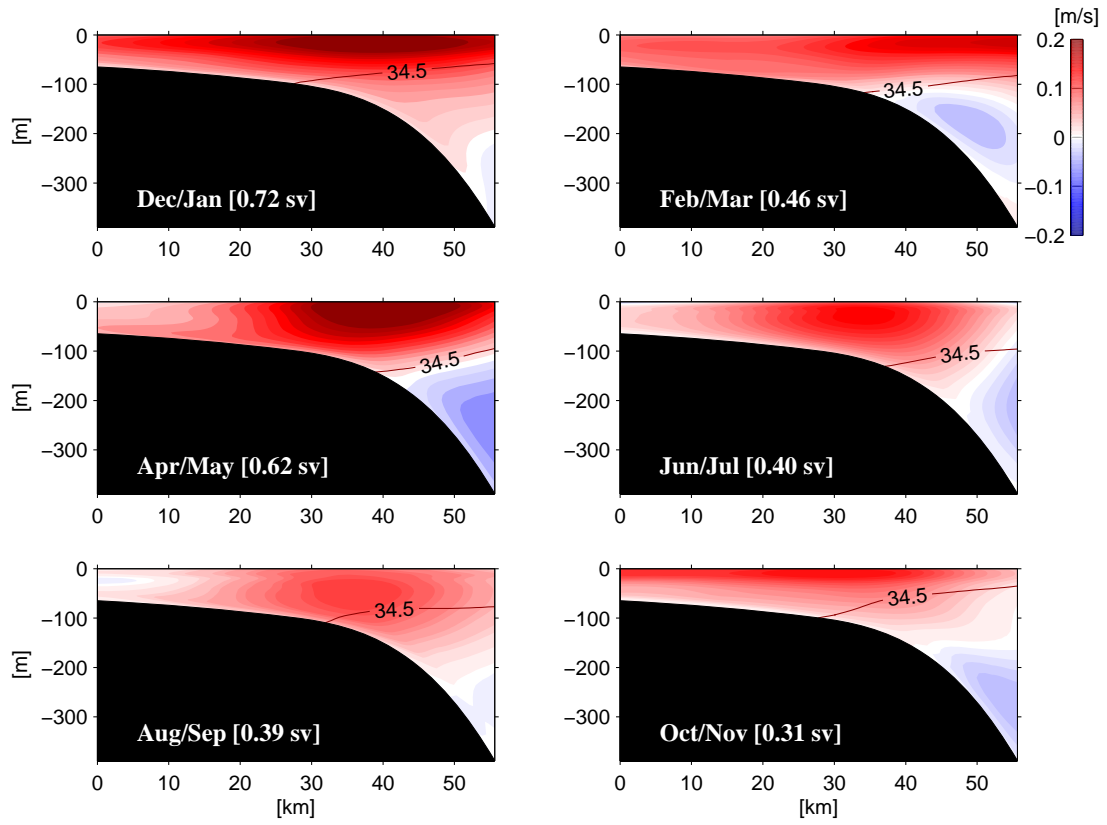


Figure 6. Simulated bi-monthly mean along-shelf velocity fields and their associated net equatorward transport. The black contour lines are the 34.5 isohaline of the respective bimonthly salinity field to indicate the location of shelfbreak front.

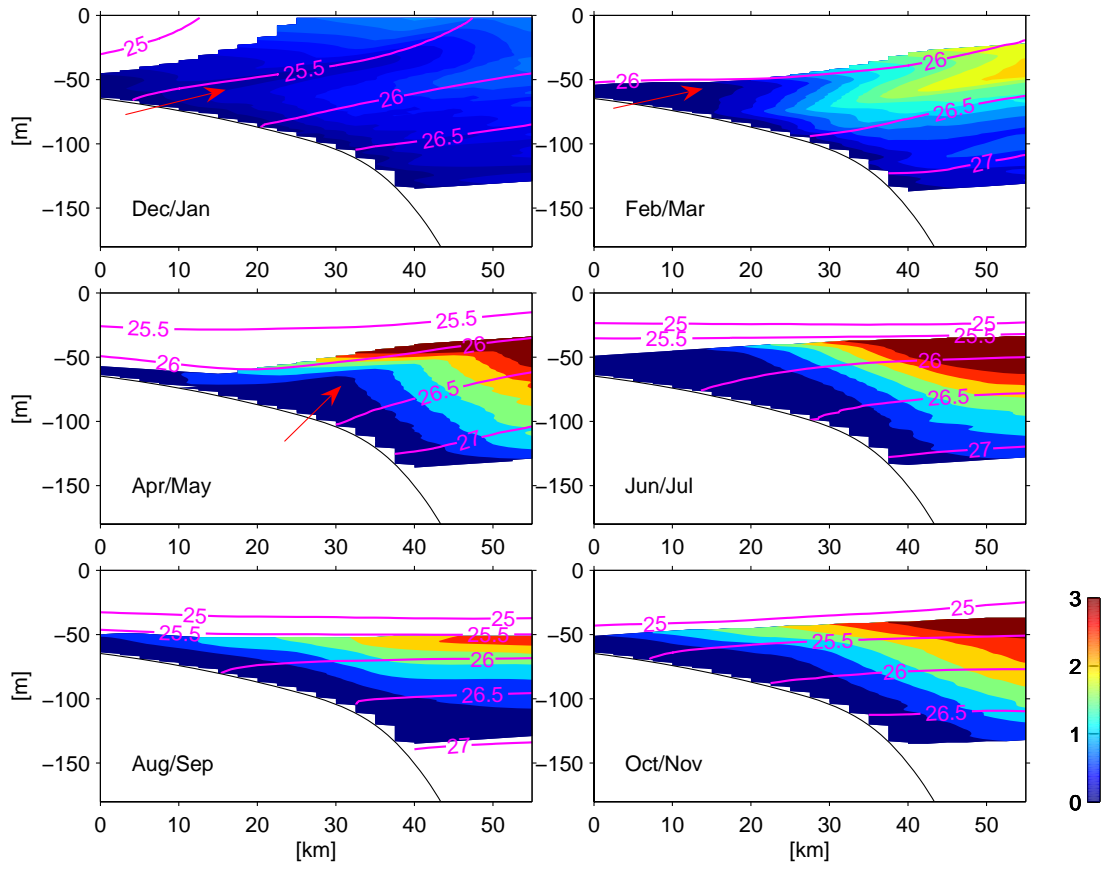


Figure 7. Bi-monthly Accumulated Theta Change (ATC) fields along the Nantucket transect. The ATC calculation is based on modeled bi-monthly density fields. The purple lines are the isopycnals, and the color shading stands for the intensity of ATC. The upward tilted, low-value ATC (indicated by arrows) is an indication of the BBL convergence and detachment.

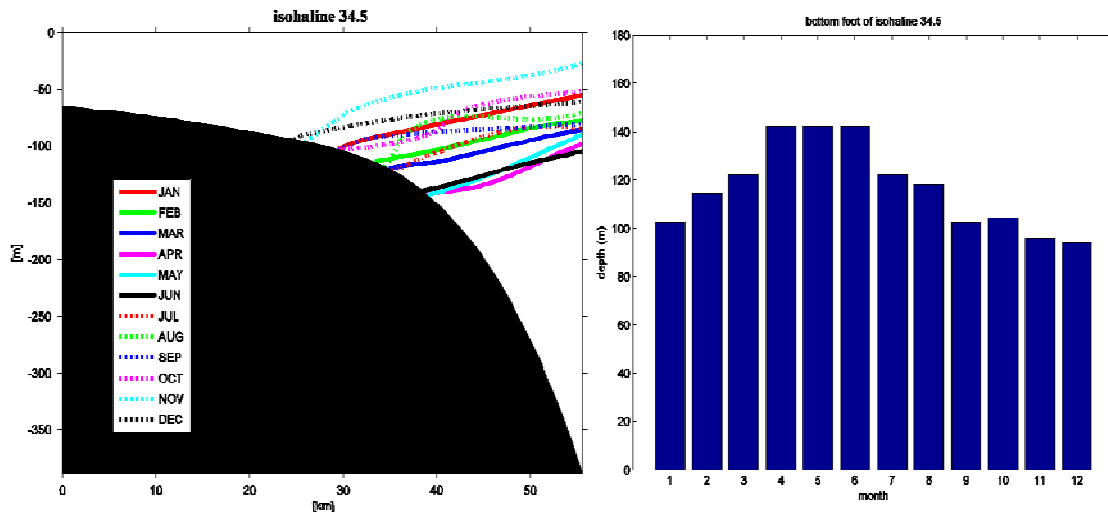


Figure 8. Monthly migrations of the shelfbreak frontal foot (left) and the histogram showing the corresponding depth of the frontal foot in each month.

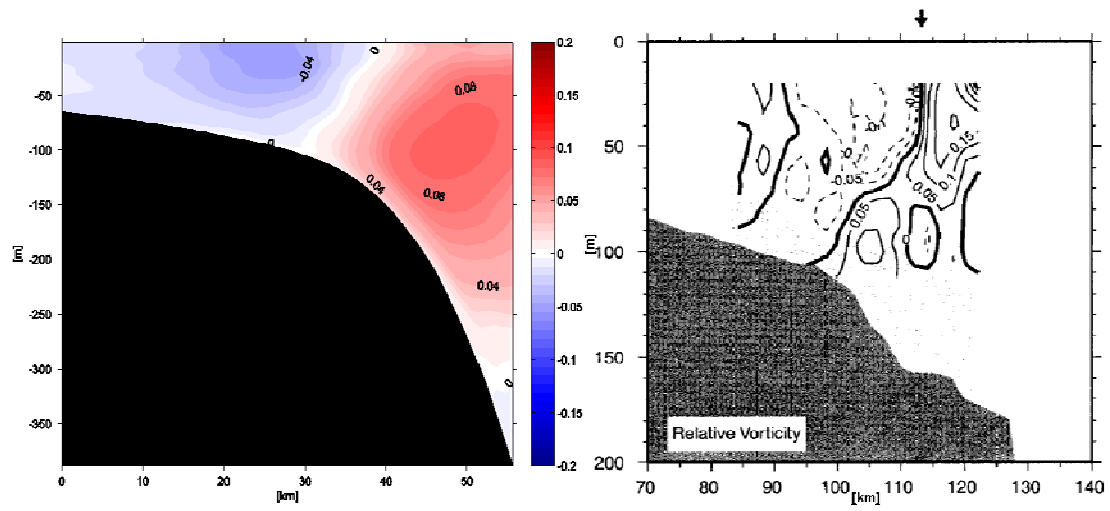


Figure 9. The comparison between simulated (left) and observed (right, adopted from *Fratantoni et al., 2001*) mean vorticity fields at the shelfbreak. Both fields are scaled by the local Coriolis parameter.

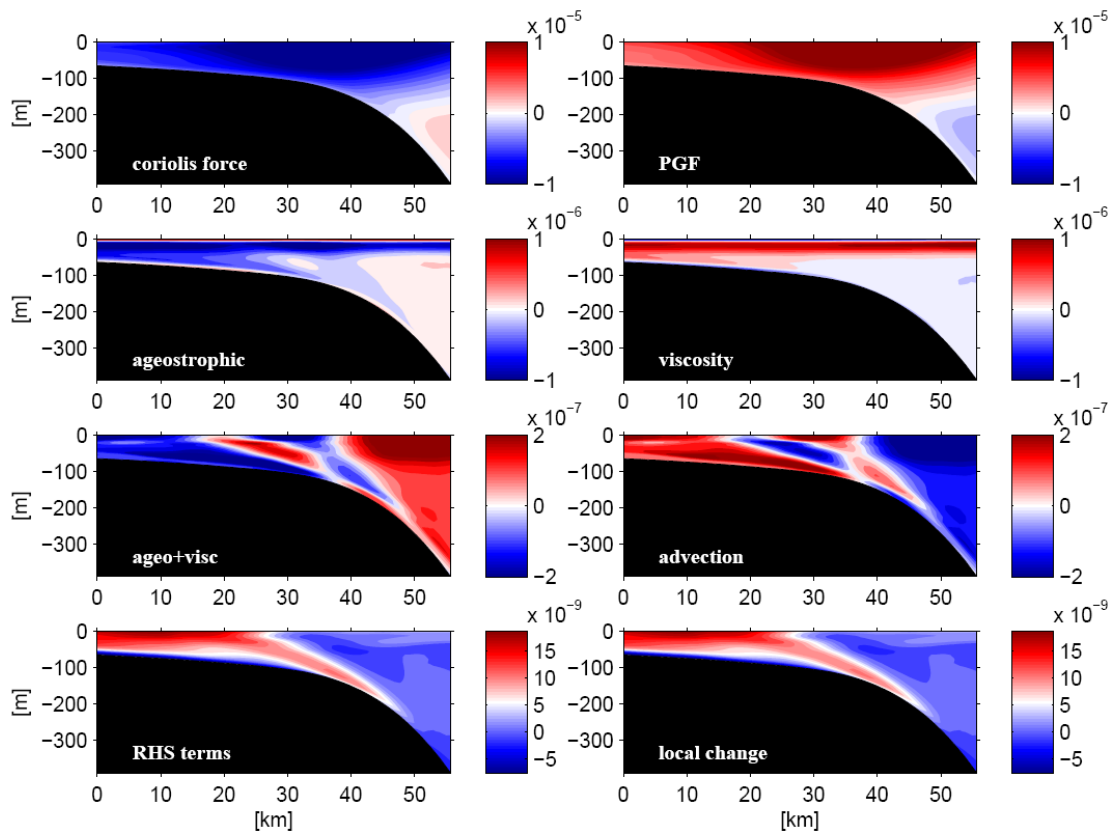


Figure 10. The mean cross-shelf momentum balance. From top to bottom and left to right are the Coriolis force, the Pressure Gradient force (PGF), the residual of Coriolis plus PGF terms (i.e., ageostrophic term), the viscosity term, the residual of ageostrophic term plus viscosity, the nonlinear advection term, the residual of ageostrophic plus viscosity and advection terms, and the local rate of change term.

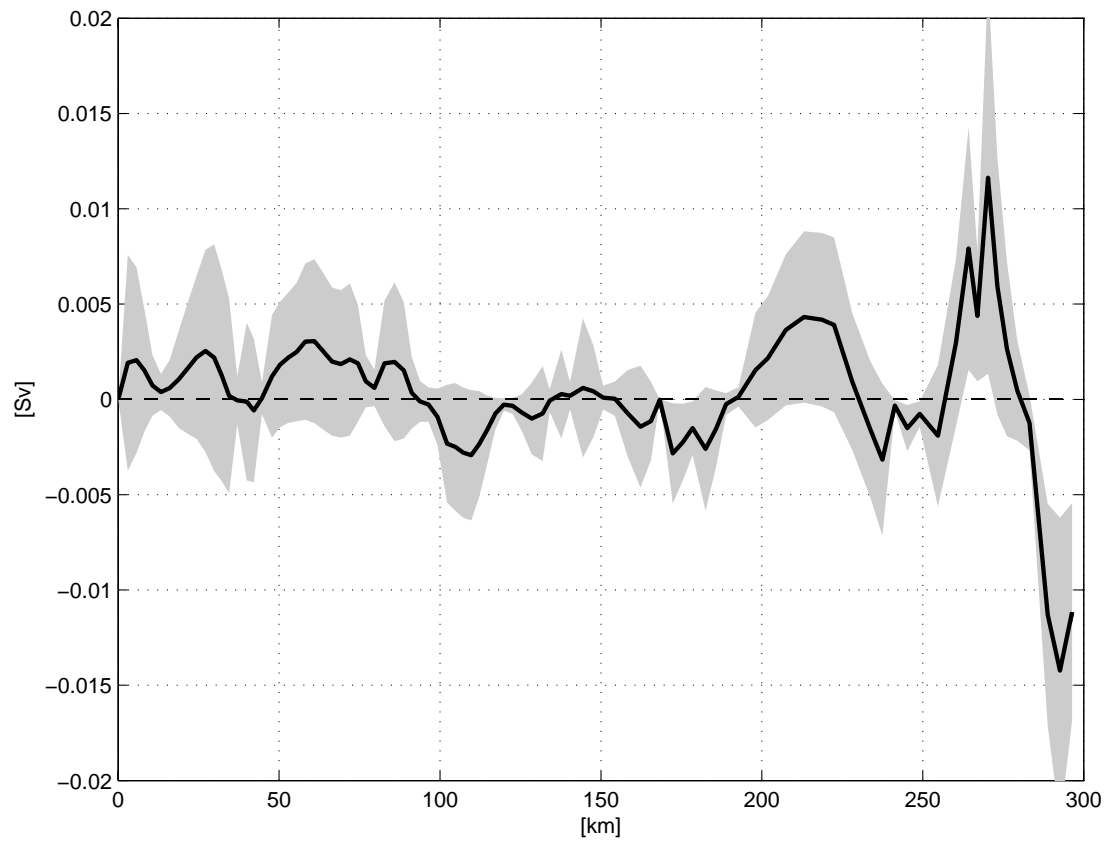


Figure 11. The cross-shelf volume transport along the 200 m isobath inside the shelfbreak ROMS domain. The x-axis is the along-isobath distance starts from zero (off the Nantucket shoal) to 300-km (off the Hudson Canyon). The solid curve is the mean cross-shelf volume transport over the 4-year period, and the gray area stands for its standard deviation.

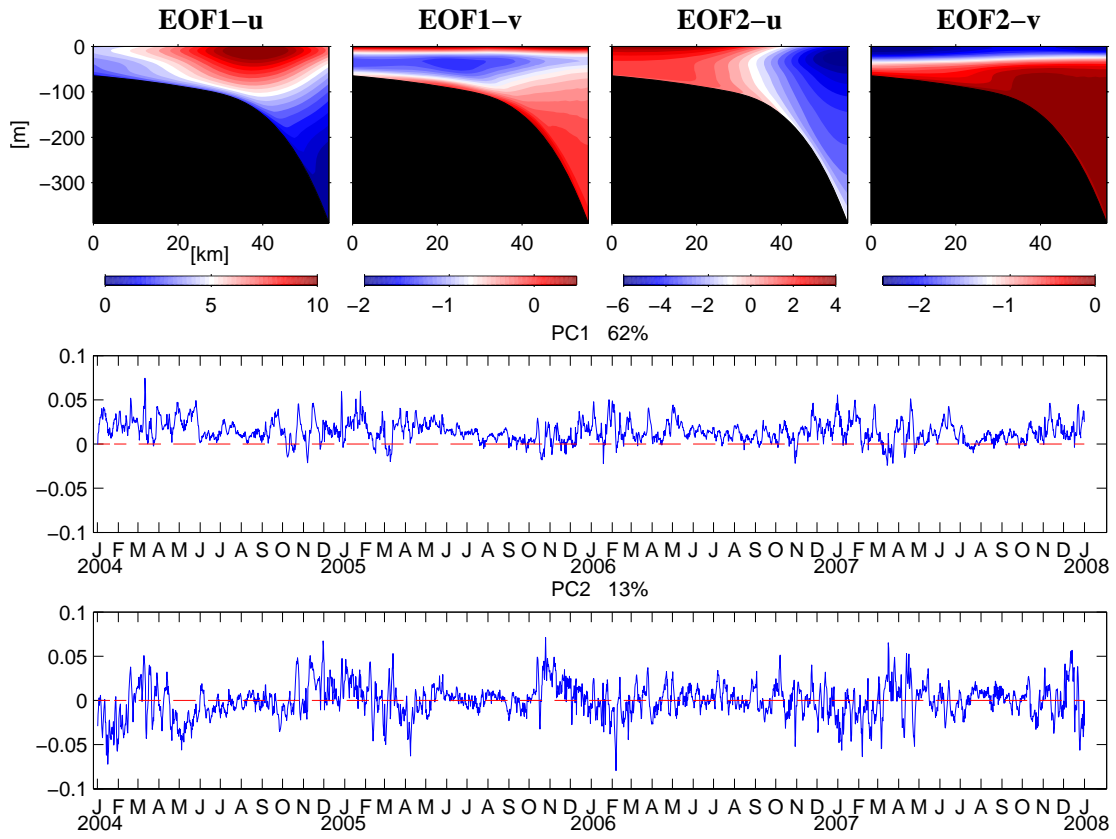


Figure 12. The first two EOF modes of simulated shelf break circulation, and their corresponding principle components. U (V) is the alongshore (cross-shelf) velocity component along the Nantucket transect.

CHAPTER 3: SEASONAL AND INTERANNUAL VARIABILITY OF PHYSICAL  
AND BIOLOGICAL DYNAMICS AT THE SHELFBREAK FRONT OF THE MIDDLE  
ATLANTIC BIGHT: NUTRIENT SUPPLY MECHANISMS<sup>2</sup>

Ruoying He<sup>a</sup>, Ke Chen<sup>a</sup>, Katja Fennel<sup>b</sup>, Glen G. Gawarkiewicz<sup>c</sup>, Dennis J. McGillicuddy, Jr<sup>d</sup>

Department of Marine Earth and Atmospheric Sciences, North Carolina State University<sup>a</sup>

Department of Oceanography, Dalhousie University<sup>b</sup>

Department of Physical Oceanography, Woods Hole Oceanographic Institution<sup>c</sup>

Department of Applied Ocean Physics and Engineering, Woods Hole Oceanographic Institution<sup>d</sup>

---

<sup>2</sup> This chapter is published in *Biogeosciences Discussions*, DOI:10.5194/bgd-8-1555-2011

## **Abstract**

A size-structured ecosystem model is coupled to a 3-dimensional, high-resolution circulation model to investigate the seasonal and interannual variability of physical and biological states and their driving mechanisms at the shelfbreak front of the Middle Atlantic Bight (MAB). Simulated surface chlorophyll fields compare favorably to the satellite observations and capture the shelfbreak biomass enhancement, which is one of the essential biological features of the region. The domain-wide upper water column nutrient content peaks in late winter-early spring. The phytoplankton spring bloom starts 1 - 2 months later, followed by a zooplankton bloom in early summer. Seasonal and interannual variability in hindcast shelfbreak nutrient supply is controlled by three processes: 1) local mixing that deepens the mixed layer and injects deep ocean nutrients into the upper water column; 2) alongshore nutrient transport by the shelfbreak jet and associated currents; and 3) nutrient upwelling associated with shelfbreak bottom boundary layer convergence. Interannual variability of physical and biological processes are highlighted by cross-shelf nutrient budget diagnostics for spring 2004 and 2007, which show not only complex vertical structure of various dynamical terms, but also significant variations in magnitude between the two years.

## **1. Introduction**

The Middle Atlantic Bight (MAB) shelfbreak region contains a sharp front that separates the cold, fresh water on the shelf from warmer, more saline water in the slope sea. Associated with the front is a narrow shelfbreak jet, which is a part of the large-scale buoyancy driven coastal current originating from the Labrador Sea (*Chapman and Beardsley, 1989; Loder et al., 1998*). The MAB shelfbreak front and jet exert a strong influence on the cross-shelf exchanges of mass, heat, freshwater, and nutrients, which further control the characteristics of physical and biological dynamics at the shelfbreak.

*In situ* and satellite observations often show higher levels of chlorophyll within the MAB frontal region, also known as the shelfbreak pigment maximum (*Marra et al., 1982; Ryan et al., 1999a, Ryan et al., 1999b; Ryan et al., 2001*). This locally enhanced

productivity provides energy to upper trophic level predators. As a result, fishes and marine mammals often aggregate in the shelfbreak front (*Podestá et al.*, 1993; *Waring et al.*, 2001). Several mechanisms are proposed to explain the shelfbreak frontal biomass enhancement. The secondary circulation in the bottom boundary layer (*Gawarkiewicz and Chapman*, 1992; *Houghton*, 1997; *Houghton and Visbeck*, 1998; *Barth et al.*, 1998; *Gawarkiewicz et al.*, 2010) has been considered as one possible process for delivering both regenerated nutrients from benthic processes over the shelf as well as deep-ocean nutrients to the euphotic zone, thus boosting primary production. The lateral transport of nutrients and plankton from the Georges Bank region is considered another key process. It is known that upstream of the MAB shelfbreak, tidal pumping on the Georges Bank constantly injects nutrients into the upper water column (e.g., *Townsend and Thomas*, 2002). While some nutrients are consumed locally, a portion can be transported downstream to the MAB.

Most earlier studies on the MAB shelfbreak circulation and ecosystem dynamics are based on either synoptic *in situ* surveys (e.g., *Gawarkiewicz et al.*, 2001; *Hales et al.*, 2009) or satellite imagery (e.g., *Ryan et al.*, 2001; *He et al.*, 2010). While having provided many valuable insights into how the shelfbreak system works, *in situ* observations are limited by both temporal and spatial coverage, whereas remote sensing is compromised by clouds and limited by its inability to measure the subsurface (e.g., *Miles et al.*, 2009; *He et al.*, 2010).

In this study, we utilize a coupled biophysical model to study MAB shelfbreak physical and biological dynamics and their associated seasonal and interannual variability. The hydrodynamics is simulated by a recently developed 3-dimensional, high resolution MAB shelfbreak circulation model described by *Chen and He* (2010), while the ecosystem dynamics is modeled by the size-structured biological model described in *Lima and Doney* (2004) and *Lehmann et al.* (2009). We performed a multi-year coupled model hindcast spanning from 2004 to 2007. The resulting time and space continuous physical and biological fields are used for several detailed process analyses. In Section 2 we give a brief description of both physical and biological models. Model validation against satellite observations is presented in Section 3. Causes of temporal and spatial

variability of physical, biological and nutrient fields are discussed in Section 4, followed by a discussion and summary in Section 5.

## 2. Methods

### 2.1. The circulation model

The MAB shelfbreak circulation model was configured based on the Regional Ocean Modeling System (ROMS, *Haidvogel et al.*, 2008; *Shchepetkin and McWilliams*, 2005). The model domain encompasses the MAB shelfbreak offshore of Nantucket Shoals in the northeast and Hudson Canyon in the southwest (**Figure 1**). Within the domain, the water depth ranges from 30 to 3000 m. The horizontal resolution of the model is 1 km. 36 terrain-following vertical levels are used in the water column with higher resolution near the surface and bottom to better resolve both ocean surface and bottom boundary layers. The minimum (maximum) model vertical spacing is 0.8 m (211 m) in the boundary layer (the mid-water column).

The MAB shelfbreak ROMS is one-way nested inside a regional-scale Middle Atlantic Bight and Gulf of Maine ROMS (hereafter MABGOM ROMS) described and validated by *He and Chen* (submitted). Along the 4 open boundaries of the shelfbreak ROMS, we use the method of *Flather* (1976) to specify the free-surface and depth-averaged velocity with MABGOM ROMS solutions plus  $M_2$  tidal harmonics from an ADCIRC tidal simulation of the western Atlantic (*Luetich et al.* 1992). For boundary temperature, salinity, and baroclinic velocity, an Orlanski-type radiation condition (*Marchesiello et al.*, 2001) is applied. Surface momentum and buoyancy forcing comes from a standard bulk flux calculation (*Fairall et al.* 2003) using the NOAA NCEP North American Regional Reanalysis (NARR) archive that includes air temperature, relative humidity, air pressure, short wave radiation, long wave radiation, cloud coverage, precipitation and surface wind speed. We applied the method of *Mellor and Yamada* (1982) to compute vertical turbulent mixing, as well as the quadratic drag formulation for the bottom friction specification.

## 2.2. The biological model

The size-structured biological model of *Lehmann et al.* (2009), which is based on the model of *Lima and Doney* (2004), is used to simulate the dynamics of picophytoplankton, diatoms, zooplankton, large detritus, small detritus, and the inorganic nutrients: nitrate and ammonium in the MABGOM domain. The nitrogen and carbon content of phytoplankton, zooplankton and detritus are tracked in the model. Chlorophyll content of the picophytoplankton and diatom groups are variable. Phytoplankton grow as a function of light, inorganic nitrogen concentration and temperature. The intracellular ratios of nitrogen, carbon and chlorophyll for phytoplankton are based on *Geider et al.* (1998) but modified to include both nitrate and ammonium (*Lima and Doney*, 2004). In addition to being grazed, small and large phytoplankton are converted into small and large detritus, respectively, through a combination of linear and quadratic loss terms. A combination of linear and quadratic terms also describes the losses from zooplankton to detritus. Decomposition of detritus to ammonium by heterotrophic bacteria is parameterized using a linear remineralization rate. Large detritus sinks at a rate of  $10 \text{ m d}^{-1}$ , while small detritus and all other biological variables do not sink. For simplicity and model stability, the diverse zooplankton population is parameterized in a single zooplankton compartment with an S-shaped grazing function (Holling-type III) and a quadratic mortality term. The interested reader is referred to *Lima and Doney* (2004) and *Lehmann et al.* (2009) for more detailed biological equations and parameterizations.

The shelfbreak biological model is embedded in its MABGOM counterpart in the same fashion as the one-way circulation downscaling described above. Its initial and boundary conditions were derived from the MABGOM biological simulation of *Lehmann et al.* (2009). The coupled simulation was initialized on December 1<sup>st</sup>, 2003 and run continuously to November 19<sup>th</sup>, 2007. For model validation and analyses described in the following sections, we focus on the period of January 2004 to November 2007.

## 3. Model-Data Comparisons

Extensive comparisons between observed and simulated shelfbreak hydrodynamics have been presented in *Chen and He* (2010). Validations show that the

MAB shelfbreak ROMS has decent skill in resolving synoptic, seasonal and interannual variability of the shelfbreak circulation, lending confidence that the biological simulation is couched in a realistic physical environment.

Satellite ocean color observations provide crucial information for validating biological model solutions. In this case, we used Aqua MODIS (Moderate Resolution Imaging Spectroradiometer) monthly mean chlorophyll data. This 4-km resolution MODIS dataset was mapped onto the shelfbreak model domain (**Figure 1**). The time series of domain-averaged chlorophyll concentration from both MODIS and our model simulation were compared to examine how well the model resolves seasonal and interannual variations.

The MODIS observations show that maximum surface chlorophyll concentration (ca.  $1.5 \text{ mg m}^{-3}$ ) occur from March to May (**Figure 2**) during the spring bloom. The surface chlorophyll concentration then declines to its annual minimum in summer (July to September) as the result of zooplankton grazing, and nutrient depletion associated with the development of summer stratification (e.g., *Walsh et al.* 1987; *Sosik et al.* 2001). In the fall, increased mixing due to storms and convective cooling break down the thermal stratification. The consequent introduction of deep water nutrients into the euphotic zone stimulates a fall bloom that is discernable in October-November (*O'Reilly and Zetlin* 1998; *Yoder et al.* 2002). The maximum chlorophyll concentration in fall is about a half of the spring peak value. Simulated chlorophyll fields closely resemble these observations (**Figure 2**). Indeed, the model captures the chlorophyll seasonal evolution well, with values generally falling within 1 standard deviation of their observational counterparts throughout almost the entire year. A discrepancy is seen in the winter when the model overestimates chlorophyll concentration. This is likely due to excessive winter mixing produced by the turbulence closure scheme (*He and Chen*, submitted), an aspect we seek to improve in a future effort.

A more robust statistical skill assessment of the temporal evolution of the domain-averaged surface chlorophyll is shown by year in the form of a Taylor diagram (*Taylor*, 2001), where correlation coefficients, centered root mean square differences (RMSD) between observed and simulated domain-averaged chlorophyll concentration, and

normalized standard deviations are all presented in a single plot (**Figure 3**). Except for 2007, the correlation coefficients between the model and data are all larger than 0.5 and all centered RMSD are less than one. The standard deviation of the simulated 2005 time series of surface chlorophyll concentration is close to that of the observations, while for other years, the values are generally smaller indicating that the model slightly underestimates observed temporal variations in the surface chlorophyll field

Model skill is further investigated by comparing observed and simulated spatial patterns in their respective seasonal means (**Figure 4**). Both are obtained by averaging over a 4-year period (2004-2007). In spring, the phytoplankton bloom spreads over the entire shelfbreak domain. Elevated chlorophyll concentrations are found on Nantucket Shoals, probably due to nutrient supply induced by strong tidal mixing (*He and Wilkin, 2006*). The model shows an elevated chlorophyll concentration at the shelfbreak; while this feature is less obvious in the relatively coarse resolution (4-km) seasonal mean satellite image, it is consistent with previous studies (e.g., *Ryan et al. 1999a*) showing the occurrence of shelfbreak chlorophyll enhancement during the spring season. In the summer, there is a minimum of chlorophyll at the surface in the entire study domain except the Nantucket Shoals region. In the fall, the breakdown of stratification allows deep-ocean nutrients to reappear in the upper water column, stimulating a region-wide fall bloom that leads to higher chlorophyll concentrations relative to summer conditions. In winter, surface chlorophyll concentrations decline again compared to the fall. The decline is associated with both light and nutrient limitation. These comparisons of seasonal maps show that the model is generally able to reproduce the seasonal evolution and spatial characteristics of the MAB shelfbreak chlorophyll fields.

Together, all comparisons (Figures 2-4) indicate that our size-structured shelfbreak biological model has some intrinsic skill in resolving the spatiotemporal variations of surface chlorophyll in the MAB shelfbreak region, providing us the confidence to use a 4-year hindcast to further characterize the physical and biological dynamics at the MAB shelfbreak.

## 4. Discussions

### 4.1 Seasonal and interannual variability of biological dynamics

We begin by focusing on the variations of simulated nutrient (nitrate and ammonium), phytoplankton (picophytoplankton and diatom) and zooplankton concentrations in the upper water column. For this analysis, all these fields are vertically averaged over the upper 50 m (for regions where local water depths are less than 50 m, the entire water column is used in averaging). Subsequently, they are also averaged over the entire model domain.

#### A. Seasonal variability

Clear seasonality in the upper water column is seen in all variables except ammonium (**Figure 5**). The highest nitrate concentration occurs in late winter and early spring. The annual maximum nitrate concentration varies from 1.5 to 3 mmol m<sup>-3</sup> over the study period. While the nitrate nutrient is abundant, phytoplankton growth is apparently inhibited by light limitation. In fact, the phytoplankton bloom does not start until the following spring season when both sufficient light and nutrients are present. Maximum phytoplankton concentrations are seen from March to May, approximately 1-2 months after the peaks in nutrient concentration. Among the phytoplankton groups, picophytoplankton show less seasonal variability with an averaged concentration of roughly 0.5 mmol N m<sup>-3</sup>. The diatoms show a more pronounced seasonal cycle. Their peak values are around 1.5 mmol N m<sup>-3</sup>, thus contributing more to the total phytoplankton variability. Zooplankton blooms begin in May-June, lagging phytoplankton blooms by approximately one month. The yearly maximum concentrations range from 0.3 to 0.4 mmol N m<sup>-3</sup>.

In the summer, nutrients are depleted in the upper water column. Consequently, both phytoplankton and zooplankton concentrations reach their annual minima. Stronger mixing events in the fall allow some regenerated deep water nutrients to enter the euphotic zone, which stimulate a weaker phytoplankton fall bloom, followed by a more discernable zooplankton bloom in November. Indeed, the seasonal evolution of nutrients,

phytoplankton and zooplankton underscore the fact that the availability of nutrients influences the timing and distribution of plankton blooms at the MAB shelfbreak.

### *B. Interannual variability*

We next focus on the interannual variability of nutrient budgets (**Figure 6**). In 2004 and 2005 the overall spring nutrient concentration (ca. 2 to 3 mmol N m<sup>-3</sup>) is twice that in 2006 and 2007 (ca. 1 to 2 mmol N m<sup>-3</sup>). As a result, the phytoplankton spring bloom is strongest in 2004 and weakest in 2007.

Temporally averaged nutrient fields during late winter and early spring (February–April) of each year allow quantification of interannual nutrient variability with respect to its 4-year (2004–2007) mean. The mean nutrient pattern is characterized by higher concentrations (ca. 3 mmol N m<sup>-3</sup>) in the northeastern corner of our shelfbreak domain (**Figure 7**, top left panel). Combined with existing knowledge of regional mean circulation (e.g., *Lentz*, 2008), this pattern indicates a nutrient input from upstream coastal areas (e.g., Georges Bank). The across-shelf nutrient field along the Nantucket transect (**Figure 7**, top right panel) further indicates that nutrient concentration increases with depth, and that there is a “nutrient pool” shoreward of the shelfbreak. These “mean” states are comparable with *in situ* synoptic observations collected in the same region (*Hales et al.*, 2009; *Gawarkiewicz et al.*, 2010).

With respect to mean nutrient conditions, 2004 is characterized as a positive anomaly year. Nutrient contents over the entire shelf (both surface and sub-surface) are higher by ca. 1 mmol N m<sup>-3</sup>. A similar situation is observed in 2005, although the higher anomalies are primarily located seaward of the shelfbreak. In contrast, 2006 and 2007 are characterized as negative anomaly years. For most areas of the shelfbreak domain, nutrient content in these two years are ca. 1 mmol N m<sup>-3</sup> less than the mean conditions.

### *C. Dominant modes of variability*

To quantify the dominant modes of nutrient and plankton variability in the upper water column (50 m), and their intrinsic linkages, we removed their temporal means and applied Empirical Orthogonal Function (EOF) analysis to their residuals. Temporal mean phytoplankton and zooplankton fields resemble the mean nutrient distribution (**Figure 8**,

upper panels). For all three variables, high concentrations occur near the upstream (northeastern) boundary of the shelfbreak domain. Maximum values for both phytoplankton and zooplankton are located in the northern corner of the domain (Nantucket shoals), shoreward of the nutrient maxima.

The first EOF mode of the surface nutrient field accounts for 87% of the variance, highlighting an apparent shelfbreak nutrient enhancement pattern. Its corresponding first principal component (PC1) shows the shelfbreak surface nutrient content reaches its peak value in the late winter and early spring (Feb-Apr), and then becomes depleted in the summer. The first EOF modes of phytoplankton and zooplankton account for 82% and 73% of the variance, respectively. For phytoplankton, the largest EOF values are located further downstream along the shelfbreak, whereas for zooplankton, the largest EOF values are nearly collocated with those of the nutrient EOF. Such differences in spatial distribution are presumably a result of the zooplankton grazing on phytoplankton.

Together, the PC1s of surface nutrient, phytoplankton and zooplankton highlight some interesting phase-locked patterns. Except for spring 2004, the nutrient variations generally lead phytoplankton variations by ca. 2 months, which in turn leads zooplankton variations by ca. 1 month. Consistent with Section 4.1.a, the EOF analysis indicates that shelfbreak plankton variation is influenced by the timing and distribution of nutrient supply. We note the second EOF modes of nutrient, phytoplankton and zooplankton representing other dynamical processes, account for only 6%, 7%, and 12% of their respective variances.

A similar EOF analysis (**Figure 9**) was performed on across-shelf nutrient, phytoplankton and zooplankton distributions along the Nantucket transect (location in **Figure 1**). The temporal mean nutrient field shows the nutricline is at about 50 m, with waters shallower than 50 m largely depleted of nutrients. This pattern is consistent with recent nutrient observations taken in the same area (*Gawarkiewicz et al., 2010*). The mean states of phytoplankton and zooplankton are similar in their across-shelf distribution. As a result of light limitation, phytoplankton accumulate mostly in the upper 100 m, as do their predators zooplankton.

The first EOF mode of cross-shelf nutrient residual (after temporal mean removed) accounts for 58% of its variance. The largest variation is located on the mid-shelf,

centered at the 80-100 m isobath. This feature is collocated with the MAB “cold pool” (Beardsley and Flagg, 1976; Houghton *et al.*, 1982) and the shoreward edge of the mean position of the foot of shelfbreak front (e.g., Linder and Gawarkiewicz, 1998). Earlier studies suggested high levels of nutrient regeneration (Rowe *et al.*, 1975; Rowe *et al.*, 1977; Harrison *et al.*, 1983) in this area. This is supported by time series of PC1 for simulated nutrient and plankton, insofar as nutrient anomalies peak after phytoplankton and zooplankton anomalies peak. The first EOFs of phytoplankton and zooplankton explain 69% and 80% of their variances, respectively, both showing the largest variations in the upper water column. For both phytoplankton and zooplankton EOFs, their subsurface variations are slightly out-of-phase (i.e., having opposite signs) from their upper water column counterparts. This is probably due to the plankton self-shading effect that when large concentrations of plankton accumulate near the surface, the growth of plankton at the subsurface can be inhibited (Tailing, 1960; Jewson, 1977; Shigesada and Okubo, 1981; Huisman, 1999).

#### 4.2. Physical control on nutrient delivery

Because the nutrient supply appears to be a central driver of MAB shelfbreak plankton dynamics, the exact mechanisms by which the shelfbreak circulation affects nutrient delivery are crucial for understanding shelfbreak ecosystem dynamics and its associated interannual variability.

We used the upper 50 m nutrient concentration within the domain as an indicator of nutrient content. The nutrient flux across the northeastern boundary of the model domain was calculated to represent the upstream nutrient input. The variability of monthly mean nutrient content at the MAB shelfbreak is found to be well correlated with the monthly mean upstream nutrient influx (**Figure 10**). The correlation coefficient between the two normalized time series is 0.92 (significant at the 95 % confidence level). We note the nutrient content peaks in a time window from November through April. The cause for this feature has both atmospheric and oceanic origins. On one hand, stronger local wind forcing in winter and spring deepens the mixed layer, making more deep-ocean nutrient available to the upper water column. On the other hand, the shelfbreak jet

reaches its highest intensity in spring (Linder *et al.*, 2004; Chen and He, 2010), maximizing the upstream nutrient influx into the MAB shelfbreak area. Taking  $0.25 \text{ ms}^{-1}$  as the mean shelfbreak jet speed in spring, it would take it about a week for a fluid parcel in the jet to traverse the shelfbreak domain under study. Because monthly values were used in Figure 10, such a time lag between local upper water-column N content and N-influx from the shelfbreak jet is not discernable. However, inflow velocities are much weaker both seaward and landward of the shelfbreak jet, thereby yielding much longer residence time of such fluid. The lack of a temporal lag between upstream nutrient input and the domain-averaged inventory may also reflect the impact of vertical mixing on upper ocean nutrient content. Indeed, time periods of increasing (decreasing) nutrient inventory in the upper 50m coincide with time periods of mixed layer depths deeper (shallower) than 50m (Figure 10). Moreover, interannual variations in nutrient content are correlated with mixed layer depth: deeper mixed layers in 2004 and 2005 are associated with larger inventories of nutrients than 2006 and 2007. Covariance between upstream nutrient input and the domain-averaged nutrient content can be explained by the same locally-forced nutrient input pertaining to the outer MABGOM domain used to specify the boundary conditions for the shelfbreak model.

The bottom boundary layer (BBL) convergence associated with the shelfbreak secondary circulation can be used to indicate the intensity of near bottom vertical advection (Chapman and Lentz, 1994; Pickart, 2000; Linder and Gawarkiewicz, 2004). To confirm the relationship between the BBL convergence ( $\nabla \cdot \vec{V}_{bottom}$ ) and upper ocean nutrient content, we computed their temporal correlation coefficients point-by-point over the entire model domain. The resulting map (**Figure 11**) reveals high positive correlation ( $r > 0.7$  at 95% confidence level) along the shelfbreak, suggesting that the upper ocean nutrient content is affected by BBL convergence.

Assuming the upstream nutrient concentration stays the same, the nutrient flux supplied by the shelfbreak jet is proportional to its strength, which we can quantify by means of the total kinetic energy ( $\text{TKE} = (u^2 + v^2)/2$ ). The 4-year Feb-Apr mean of depth-averaged TKE ( $\langle \text{TKE} \rangle$  **Figure 12**, top left panel) clearly depicts the shelfbreak jet structure. The 4-year mean seasonal alongshore velocity  $\langle U \rangle$  at the Nantucket transect

(**Figure 12**, top right panel) shows that the core of the shelfbreak jet extends to 10-20 m below the surface with a maximum speed of  $0.25 \text{ ms}^{-1}$ . Interannual variability (**Figure 12**, all other panels) can be gleaned from anomalies ( $\text{TKE}'$  and  $U'$ ) of individual spring in each year relative to their 4-year mean seasonal  $\langle \text{TKE} \rangle$  and 4-year mean seasonal alongshore velocity  $\langle U \rangle$  fields. We see spring 2004 in particular is characterized by a much stronger shelfbreak jet and higher TKE (i.e., the largest positive anomalies). In contrast, spring 2007 has the weakest jet and much lower TKE over the entire shelf (i.e., the largest negative anomalies).

Earlier studies have shown that the MAB shelfbreak jet is primarily buoyancy-driven with its interannual variability controlled by large scale hydrography (e.g., *Chapman*, 1986; *Chapman and Beardsley*, 1989; *Loder et al*, 1998; *Gawarkiewicz and Chapman*, 1992; *Chapman and Lentz*, 1994; *Chapman*, 2000). Simulated hydrographic conditions (not shown) over the 4-year hindcast period reveal shelf waters in spring 2004 are ca.  $0.5 \text{ }^\circ\text{C}$  cooler and ca. 0.4 PSU saltier than their respective 4-year mean seasonal temperature and salinity fields. In comparison, the simulated shelf water is ca.  $0.5 \text{ }^\circ\text{C}$  warmer and ca. 0.3 PSU fresher in spring 2007. Such interannual variability in local hydrography may be in part traced back further upstream. For instance, fresh water runoff from major rivers (Penobscot River, St. Johns River, Kennebec River, Androscoggin River and Merrimack River) in the Gulf of Maine is generally larger in 2006-2007 than in 2003-2004 (USGS river gauge data, not shown). Conceptually, the presence of relatively denser (saltier and warmer) shelf waters in 2004 favors a bottom-advected plume (*Chapman and Lentz*, 1994; *Yankovsky and Chapman*, 1997), whereas the presence of relatively lighter (warmer and fresher) shelf water in 2007 favors a surface-advected plume near the shelfbreak. The shelfbreak isopycnal tilting is steeper in the bottom-advected plume scenario, favoring a larger cross-shelf density gradient, and thus a stronger shelfbreak jet in 2004 than in 2007.

#### 4.3. Nutrient budget diagnostics

The dynamic details of the nutrient field can be further analyzed through term-by-term diagnosis of its governing equation in the model:

$$\frac{\partial N}{\partial t} = -\left(u \frac{\partial N}{\partial x} + v \frac{\partial N}{\partial y}\right) - w \frac{\partial N}{\partial z} + \frac{\partial}{\partial z} \left(K \frac{\partial N}{\partial z}\right) + hdiff + Source - Sink$$

By examining the relative importance of horizontal advection (HADV:  $-(u \frac{\partial N}{\partial x} + v \frac{\partial N}{\partial y})$ ), vertical advection (VADV:  $-w \frac{\partial N}{\partial z}$ ), vertical diffusion (VDIFF:  $\frac{\partial}{\partial z} (K \frac{\partial N}{\partial z})$ ), horizontal diffusion (HDIFF), and source minus sink (SmS) terms for the local rate of change ( $\partial N/\partial t$ ), we seek to quantify key dynamic processes that dominate the shelfbreak nutrient balance.

For comparison, we perform such analysis for both 2004 and 2007, during the early spring season (Feb-Apr) when the shelfbreak jet is strongest (*Linder et al., 2004; Chen and He, 2010*). **Figure 13** shows the seasonal averages of each term along the Nantucket transect for both years. The local rate of change ( $\partial N/\partial t$ ) terms in both years show the nutrient decreasing near the surface, reflecting nutrient uptake that exceeds supply to the upper water column.

The HADV term represents horizontal nutrient transport. We note that cross-shelf advection  $-v \frac{\partial N}{\partial y}$  is much smaller than along-shelf advection  $-u \frac{\partial N}{\partial x}$  (not shown), so positive values of HADV reflect along-shelf nutrient input from upstream. At the location of the shelfbreak jet, positive HADV (on the order of  $10^{-5}$  mmol N  $\cdot$  s $^{-1}$ ) is seen near the surface in both springs, with values in 2004 much larger than in 2007. By definition, the along-shelf nutrient advection  $-u \frac{\partial N}{\partial x}$  is affected by interannual variability in both nutrient concentration ( $N$ ) and shelfbreak jet ( $u$ ) strength. Both aspects contribute to the interannual variability in the simulated fluxes, as the jet is stronger and background nutrient concentrations are higher in spring 2004 versus spring 2007 (Figures 7,12). HADV also contains significant vertical structure. For example, seaward of the shelfbreak jet, negative HADV is seen at depth in both springs. This is probably related to the opposing slope current at depth (Figure 12).

The shelfbreak break nutrient upwelling related to the secondary circulation and BBL convergence is represented by positive VADV values. We note that the model shows the mean vertical velocity at the shelfbreak is on the order of  $10 \text{ m day}^{-1}$ , a value comparable with the observation-based estimates (e.g., *Houghton and Visbeck, 1998*). In 2004, the positive VADV (on the order of  $10^{-5} \text{ mmol N}\cdot\text{s}^{-1}$ ) at the shelfbreak extends from the foot of the shelfbreak front to the water column interior, and is significantly larger than the corresponding positive area of VADV in 2007, indicating nutrient upwelling due to the shelfbreak BBL convergence is stronger in 2004. Farther offshore (200m and deeper), the shelf slope BBL VADV is larger in spring 2007 than in spring 2004. In general, HADV and VADV are one order of magnitude larger than other diagnostic terms. But because they are nearly mirror images of each other, the sum of HADV and VADV (i.e., the total advection) is the same order of magnitude as the diffusion term, SmS, and the local rate of change ( $\partial N/\partial t$ ).

The vertical diffusion term also shows significant contrast between 2004 and 2007. Larger positive VDIFF located in the surface in 2004 indicates stronger mixing that injects more nutrients to the upper water column, thereby providing a larger nutrient supply. Finally, the source minus sink (SmS) term represents biological processes, showing opposite tendencies between the upper (negative) and lower (positive) part of the water column. Consistent with earlier studies (e.g., *Hopkinson, 1987; Fennel et al., 2006*), these patterns suggest nutrients are being utilized by phytoplankton near the surface, and are being regenerated at depth.

## 5. Summary and Conclusion

We coupled a size-structured ecosystem model with an existing three-dimensional high resolution circulation model (*Chen and He, 2010*) for the MAB shelfbreak region. This coupled biophysical model is nested within an existing coupled size-structured ecosystem model (*Lehmann et al. 2009*) for the Middle Atlantic Bight and Gulf of Maine (MABGOM). The shelfbreak coupled biophysical model was used to hindcast the MAB shelfbreak circulation and ecosystem variations from December 2003 to November 2007. Favorable comparisons with MODIS-AQUA chlorophyll observations indicate that the

coupled model can resolve the physical and biological dynamics at the MAB shelfbreak front. Time and space continuous hindcast fields from January 2004 to November 2007 were then used to investigate the seasonal and interannual characteristics of the MAB shelfbreak frontal circulation and ecosystem variability.

Consistent with previous studies (e.g., *Marra et al.* 1982, 1990; *Ryan et al.* 1999a, 1999b; *Gawarkiewicz et al.*, 2010), our model hindcast and EOF analysis suggest that there is a biomass enhancement at the shelfbreak. Region-wide upper water column nutrient content peaks in late winter and early spring. The phytoplankton spring bloom starts 1 - 2 months later, followed by a zooplankton bloom in early summer. Increased mixing in the fall season allows subsurface nutrient injection to the euphotic zone, stimulating a second but smaller phytoplankton bloom and subsequent zooplankton bloom.

Focusing on the early spring season (Feb-Apr), our analysis shows strong interannual variability of nutrient supply at the MAB shelfbreak. Specifically, the spring of 2004 and 2005 were relatively nutrient-rich, whereas the spring of 2006 and 2007 were relatively nutrient-poor. The cause for this feature has both atmospheric and oceanic origins. On one hand, stronger local wind mixing in winter and spring of 2004 and 2005 deepened the oceanic mixed layer depth up to 100 m, making more deep-ocean nutrient available to the upper water column. On the other hand, the shelfbreak jet was stronger in spring 2004 and 2005, allowing more effective alongshore advection of nutrients from upstream. In addition to surface mixing and horizontal advection, vertical advection associated with the shelfbreak bottom boundary layer (BBL) convergence is another contributing factor for the upper water column nutrient content. This is confirmed by significant positive temporal correlation between the BBL convergence ( $\nabla \cdot \vec{V}_{bottom}$ ) and upper ocean nutrient content.

Nutrient budget diagnostics for spring 2004 and 2007 along the Nantucket transect highlighted not only complex vertical structures of various dynamical terms (processes), but also significant variations in magnitude between the two years. Because nutrient advection ( $-u \partial N / \partial x - v \partial N / \partial y - w \partial N / \partial z$ ) is affected by interannual variability in both nutrient concentration ( $N$ ) and shelfbreak current ( $u, v, w$ ), it is difficult to distinguish the

two effects in the present study, In the future, an idealized modeling investigation using the same nutrient background state (N) will be pursued to further quantify the relative contributions of shelfbreak jet (u) and local shelfbreak upwelling (w) to the variation of shelfbreak nutrient content.

Although not analyzed explicitly in this study, interannual variability of the MAB shelfbreak circulation is also influenced by warm core rings. In summer 2006 for instance, a large warm core eddy impinged on the shelfbreak, slowing down the shelfbreak jet. Details of that process will be presented in a separate correspondence (*Chen and He*, in preparation).

Our study demonstrates that realistic coupled biophysical modeling can offer a powerful tool to better understand and quantify complex physical and biological processes in an energetic shelfbreak environment. We note however that the complexity of the food web and uncertainties in parameterizations impose some limitations on coupled biophysical modeling. For example, the exclusion of the silicate compartment in our ecosystem model may reduce the accuracy of the simulated diatom population. Improvement in shelfbreak marine ecosystem prediction clearly requires refinement of model parameterizations, advanced observational infrastructure together with sophisticated techniques for data assimilation. In that regard, the emerging MAB shelfbreak Pioneer Array (a part of the Ocean Observatory Initiative from the National Science Foundation) and new *in situ* observations it is about to collect would be most valuable.

### **Acknowledgments**

Research support provided through ONR Grant N00014-06-1-0739 and NASA Grant NNX07AF62G is much appreciated.

## Reference

- Armstrong, R.A., Stable model structures for representing biogeochemical diversity and size spectra in plankton communities, *Journal of Plankton Research*, 21, 445-464, 1999.
- Barth, J.A., D. Bogucki, S.D. Pierce, and P.M. Kosro, Secondary circulation associated with a shelfbreak front, *Geophysical Research Letters*, 25 (15), 2761-2764, 1998.
- Chapman, D.C., A Simple Model of the Formation and Maintenance of the Shelf/Slope Front in the Middle Atlantic Bight, *Journal of Physical Oceanography*, 16 (7), 1273-1279, 1986.
- Chapman, D.C., Boundary Layer Control of Buoyant Coastal Currents and the Establishment of a Shelfbreak Front, *Journal of Physical Oceanography*, 30, 2941-2955, 2000.
- Chapman, D.C., and R.C. Beardsley, On the origin of shelf water in the Middle Atlantic Bight, *Journal of Physical Oceanography*, 19, 384-391, 1989.
- Chapman, D.C., and S.J. Lentz, Trapping of a coastal density front by the bottom boundary layer, *Journal of Physical Oceanography*, 24, 1464-1479, 1994.
- Chen, K., and R. He, Numerical Investigation of the Middle Atlantic Bight Shelfbreak Frontal Circulation Using a High-resolution Ocean Hindcast Model, *Journal of Physical Oceanography*, 40, 949-964, 2010.
- Fairall, C.W., E.F. Bradley, J.E. Hare, A.A. Garchev, and J. Edson, Bulk parameterization of air-sea fluxes: Updates and verification for the COARE algorithm, *Journal of Climate*, 16, 571-591, 2003.
- Fennel, K., J. Wilkin, J. Levin, J. Moisan, J. O'Reilly, and D. Haidvogel, Nitrogen cycling in the Middle Atlantic Bight: Results from a three-dimensional model and implications for the North Atlantic nitrogen budget, *Journal of Geophysical Research*, 111 (C06003), doi:10.1029/2005JC003116, 2006.
- Flagg, C.N., M. Dunn, D. Wang, H.T. Rossby, and R.L. Benway, A study of the currents of the outer shelf and slope from a decade of shipboard ADCP observations in the Middle Atlantic Bight, *Journal of Geophysical Research*, 111 (C06003), doi:10.1029/2005JC003116, 2006.
- Flather, R.A., A tidal model of the northwest European continental shelf, *Mem. Soc. R. Sci. Liege*, 6 (10), 141-164, 1976.
- Frajka-Williams, E., and P.B. Rhines, Physical controls and interannual variability of the Labrador Sea spring phytoplankton bloom in distinct regions, *Deep-Sea Research Part 1*.
- Fratantoni, P.S., and R.S. Pickart, Variability of the shelfbreak jet in the Middle Atlantic Bight: Internally or externally forced?, *Journal of Geophysical Research*, 108 ((C5)3166), doi:10.1029/2002JC001326, 2003.

Gawarkiewicz, G., F. Bahr, R.C. Beardsley, and K.H. Brink, Interaction of a slope eddy with the shelfbreak front in the Middle Atlantic Bight, *Journal of Physical Oceanography*, 31 (9), 2783-2796, 2001.

Gawarkiewicz, G., A. Shcherbina, M. Charette, and L. Graziano, Frontal Upwelling and Nutrient Transport in the Shelfbreak Front of the Middle Atlantic Bight, submitted, 2010.

Gawarkiewicz, G.G., and D.C. Chapman, The Role of Stratification in the Formation and Maintenance of Shelf-Break Fronts, *Journal of Physical Oceanography*, 22 (7), 753-772, 1992.

Geider, R., H. MacIntyre, and T. Kana, A dynamic regulatory model of phytoplankton acclimation to light, nutrients, and temperature, *Limnology and Oceanography*, 43, 679-694, 1998.

Haidvogel, D.B., H. Arango, W.P. Budgell, B.D. Cornuelle, E. Curchitser, E. Di Lorenzo, K. Fennel, W.R. Geyer, A.J. Hermann, L. Lanerolle, J. Levin, J.C. McWilliams, A.J. Miller, A.M. Moore, T.M. Powell, A.F. Shchepetkin, C.R. Sherwood, R.P. Signell, J.C. Warner, J. Wilkin: Ocean forecasting in terrain-following coordinates: Formulation and skill assessment of the Regional Ocean Modeling System, *Journal of Computational Physics*, 227, 7, 3595-3624, 2008.

Hales, B., R.D. Vaillancourt, L. Prieto, J. Marra, R. Houghton, and D. Hebert, High-resolution surveys of the biogeochemistry of the New England shelfbreak front during summer, 2002, *Journal of Marine Systems*, 78, 426-441, 2009.

He, R., and K. Chen, Investigation of Northeastern North America Coastal Circulation Using a Regional Circulation Hindcast Model, *Continental Shelf Research*, submitted.

He, R., and J.L. Wilkin, Barotropic tides on the southeast New England shelf: A view from a hybrid data assimilative modeling approach, *Journal of Geophysical Research*, 111 (C08002), doi:10.1029/2005JC003254, 2006.

Hopkinson, C.S., Nutrient regeneration in shallow-water sediments of the estuarine plume region of the nearshore Georgia Bight, *Maine Biology*, 94, 127-142, 1987.

Houghton, R.W., Lagrangian flow at the foot of a shelfbreak front using a dye tracer injected into the bottom boundary layer, *Geophysical Research Letters*, 24 (16), 2305-2308, 1997.

Houghton, R.W., R.D. Vaillancourt, J. Marra, D. Hebert, and B. Hales, Cross-shelf circulation and phytoplankton distribution at the summertime New England shelfbreak front, *Journal of Marine Systems*, 78 (3), 411-425, 2009.

Houghton, R.W., and M. Visbeck, Upwelling and convergence in the Middle Atlantic Bight shelfbreak front, *Geophysical Research Letters*, 25 (15), 2765-2768, 1998.

Huisman, J., Population Dynamics of Light-Limited Phytoplankton: Microcosm Experiments, *Ecology*, 80 (1), 202-210, 1999.

- Hunt, G.L., and S. Mckinnell, Interplay between top-down, bottom-up, and wasp-waist control in marine ecosystems, *Progress in Oceanography*, 68, 115-124, 2006.
- Jewson, D.H., Light penetration in relation to phytoplankton content of the euphotic zone of Lough Neagh, North Ireland, *Oikos*, 28 (74-83), 1977.
- Kiorboe, T., Turbulence, phytoplankton cell size and the structure of pelagic food webs, *Advances in Marine Biology*, 27, 1-73, 1993.
- Lehmann, M.K., K. Fennel, and R. He, Statistical validation of a 3-D bio-physical model of the western North Atlantic, *Biogeosciences*, 6, 1-14, 2009.
- Lima, I.D., and S.C. Doney, A three-dimensional, multnutrient, and size-structured ecosystem model for the North Atlantic, *Global Biogeochemical Cycles*, 18 (GB3019), doi:10.1029/2003GB002146, 2004.
- Linder, C.A., G.G. Gawarkiewicz, and R.S. Pickart, Seasonal characteristics of bottom boundary layer detachment at the shelfbreak front in the Middle Atlantic Bight, *Journal of Geophysical Research*, 109 (C03049), doi:10.1029/2003JC002032, 2004.
- Lorder, J.W., B. Petrie, and G. Gawarkiewicz, The coastal ocean off northeastern North America: A large-scale view, in *The Sea*, pp. 105-133, Wiley, New York, 1998.
- Lozier, M.S., M.S. Reed, and G.G. Gawarkiewicz, Instability of a shelfbreak front, *Journal of Physical Oceanography*, 32, 924-944, 2002.
- Luetlich, R.A., J.J. Westerink, and N.W. Scheffner, ADCIRC: An advanced three-dimensional circulation model for shelves, coast, and estuaries. Report 1. Theory and Methodology of ADCIRC-2DDI and ADCIRC-3DL., U.S. Army Corps of Engineers Tech. Rep., DPR-92-6, 137pp, 1992.
- Marchesiello, P., J.C. McWilliams, and A.F. Shchepetkin, Open boundary conditions for long-term integration of regional oceanic models, *Ocean Modeling*, 3, 1-20, 2001.
- Marra, J., R.W. Houghton, D.C. Boardman, and P.J. Neale, Variability in surface chlorophyll at a shelfbreak front, *Journal of Marine Research*, 40 (3), 575-591, 1982.
- Marra, J., R.W. Houghton, and G. Christopher, Phytoplankton growth at the shelf-break front in the Middle Atlantic Bight, *Journal of Marine Research*, 48 (4), 851-868, 1990.
- Miles, T.N., R. He, and M. Li, Characterizing the South Atlantic Bight seasonal variability and cold water event in 2003 using a daily cloud free SST and chlorophyll analysis, *Geophysical Research Letters*, 36 (L02604), doi:10.1029/2008GL036396, 2009.
- O'Reilly, J.E., and C. Zetlin, Seasonal, horizontal, and vertical distribution of phytoplankton chlorophyll a in the northeast US continental shelf ecosystem, in NOAA Technical Report NMFS, pp. 139, US Department of Commerce, 1998.
- Pickart, R.S., Bottom boundary layer structure and detachment in the shelfbreak jet of the Middle Atlantic Bight, *Journal of Physical Oceanography*, 30, 2668-2686, 2000.

- Podesta, G.P., J.A. Browder, and J.J. Hoey, Exploring the association between swordfish catch rates and thermal fronts on U.S. longline grounds in the western North Atlantic, *Continental Shelf Research*, 13 (2-3), 253-277, 1983.
- Rowe, G.T., C.H. Clifford, and K.L. Smith, Nutrient regeneration in sediment off Cape Blanc, Spanish Sahara, *Deep-Sea Research Part1*, 24, 57-63, 1977.
- Rowe, G.T., C.H. Clifford, K.L. Smith, and P.L. Hamilton, Benthic nutrient regeneration and its coupling to primary productivity in coastal waters, *Nature*, 255 (215-217), 1975.
- Ryan, J.P., J.A. Yorder, J.A. Barth, and P.C. Cornillon, Chlorophyll enhancement and mixing associated with meanders of the shelf break front in the Mid-Atlantic Bight, *Journal of Geophysical Research*, 104 (C10), 23,479-23,493, 1999.
- Ryan, J.P., J.A. Yorder, and P.C. Cornillon, Enhanced chlorophyll at the shelfbreak of Mid-Atlantic Bight and Georges Bank during the spring transition, *Limnology and Oceanography*, 44 (1), 1-11, 1999.
- Ryan, J.P., J.A. Yorder, and D.W. Townsend, Influence of a Gulf Stream warm-core ring on water mass and chlorophyll distributions along the southern flank of Georges Bank, *Deep-Sea Research Part2*, 48 (159-178), 2001.
- Shchepetkin, A.F., and J.C. McWilliams, The regional oceanic modeling system (ROMS): a split-explicit, free surface, topography-following-coordinate oceanic model, *ocean Modeling*, 9, 347-404, 2005.
- Shigesada, N., and A. Okubo, Analysis of the self-shading effect on algal vertical distribution in natural waters, *Journal of Mathematical Biology*, 112 (3), 311-326, 1981.
- Sieburth, J.M., V. Smetacek, and J. Lenz, Pelagic ecosystem structure: heterotrophic compartments of the plankton and their relationship to plankton size fractions, *Limnology and Oceanography*, 23 (1256-1263), 1978.
- Sosik, H.M., R.E. Green, W.S. Pegan, and C.S. Roesler, Temporal and vertical variability in optical properties of New England shelf waters during late summer and spring, *Journal of Geophysical Research*, 106 (9455-9472), 2001.
- Storm, S.L., C.B. Miller, and B.W. Frost, What sets lower limits to phytoplankton stocks in high-nitrate, low-chlorophyll regions of the open ocean?, *Mar. Ecol.-Prog. Ser.*, 193, 19-31, 2000.
- Talling, J.F., Self-shading effects in natural populations of a planktonic diatom, *Wetter und Leben*, 12 (235-242), 1960.
- Taylor, K.E., Summarizing multiple aspects of model performance in a single diagram, *Journal of Geophysical Research - Atmosphere*, 106, 7183-7192, 2001.
- Townsend, D.W., and A.C. Thomas, Winter-spring transition of phytoplankton chlorophyll and inorganic nutrients on Georges Bank, *Deep-Sea Research Part2*, 48, 199-214, 2001.

Townsend, D.W., and M. Thomas, Springtime nutrient and phytoplankton dynamics on Georges Bank, *Marine Ecological Progress Series*, 228, 54-74, 2002.

Walsh, J.J., T.E. Whitledge, J.E. O'Reilly, W.C. Phoel, and A.F. Draxler, Nitrogen cycling on Georges Bank and the New York Shelf: A comparison between well-mixed and seasonally stratified waters, in *Georges Bank*, edited by R.H. Backus, and D.W. Bourne, pp. 234-246, The MIT Press, 1987.

Waring, G.T., T. Hamzaki, D. Sheehan, G. Wood, and S. Baker, Characterization of Beaked Whale (*Ziphiidae*) and Sperm Whale (*Physeter Macrocephalus*) summer habitat in shelf-edge and deeper waters off the northeast U.S., *Marine Mammal Science*, 17 (4), 703-717, 2001.

Yankovsky, A.E., and D.C. Chapman, A Simple Theory for the Fate of Buoyant Coastal Discharges, *Journal of Physical Oceanography*, 27 (7), 1386-1401, 1997.

Yorder, J.A., S.E. Schollaert, and J.E. O'Reilly, Climatological phytoplankton chlorophyll and sea surface temperature patterns in continental shelf and slope waters off the northeast U.S. coast, *Limnology and Oceanography*, 47, 672-682, 2002.

## Figures

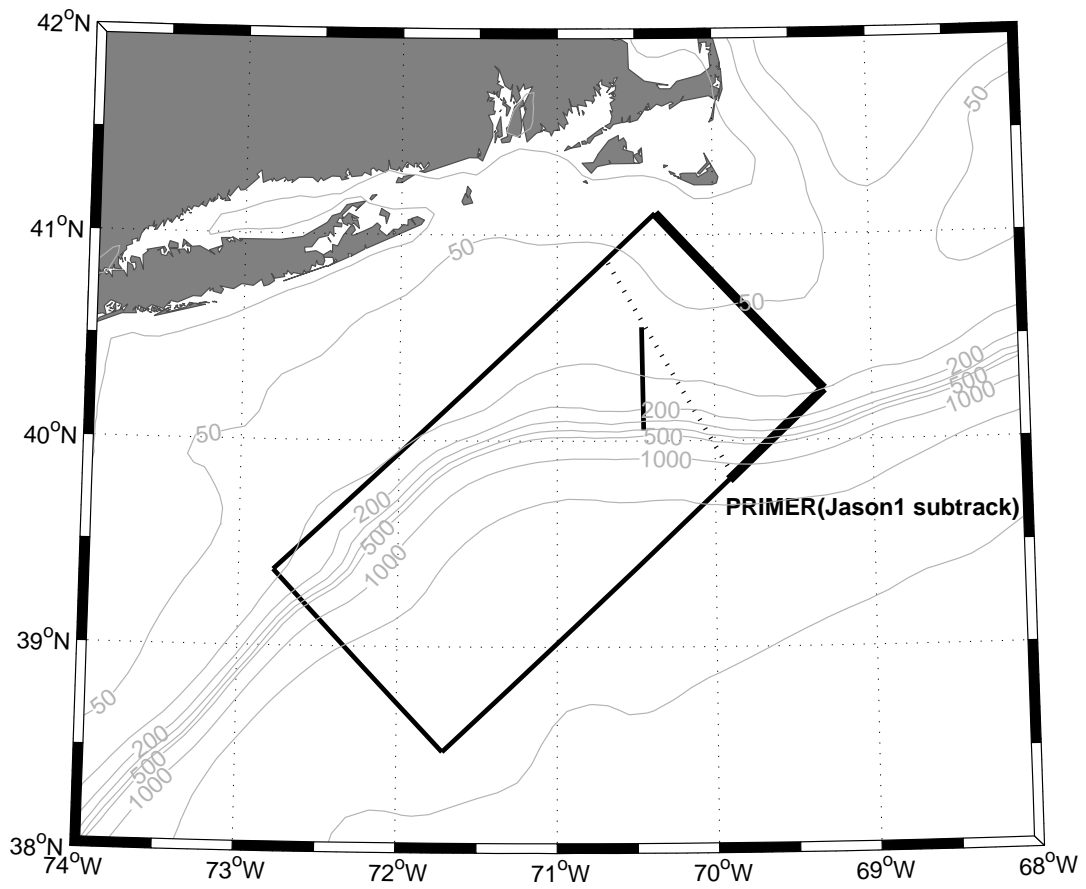


Figure 13. The shelfbreak model domain (box) and the location of Nantucket transect discussed in the following sections (solid line). Also shown is a satellite (Jason1) sub-track (dotted line). The thick line along the northeastern boundary defines the location of the upstream nutrient input calculation. Local isobaths are also shown in light gray.

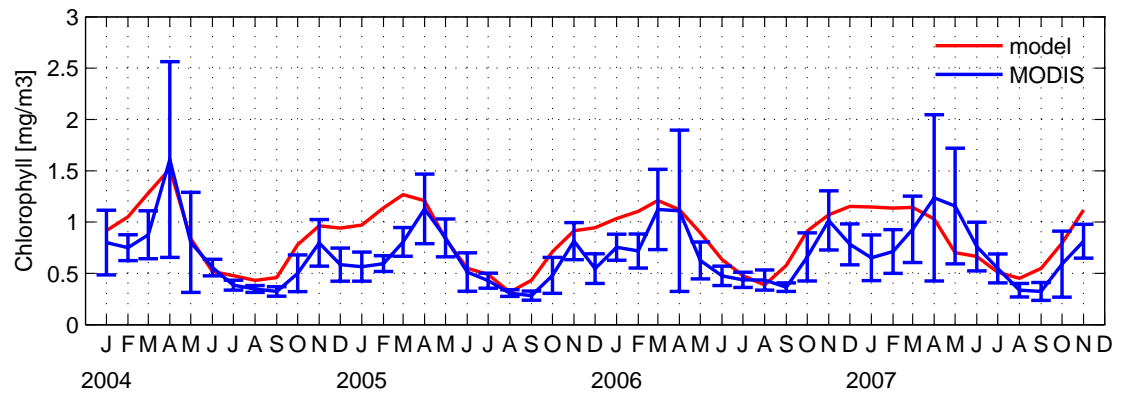


Figure2. Monthly domain-averaged surface chlorophyll from the shelfbreak model (red) and Aqua-MODIS data (blue, with one standard deviation).

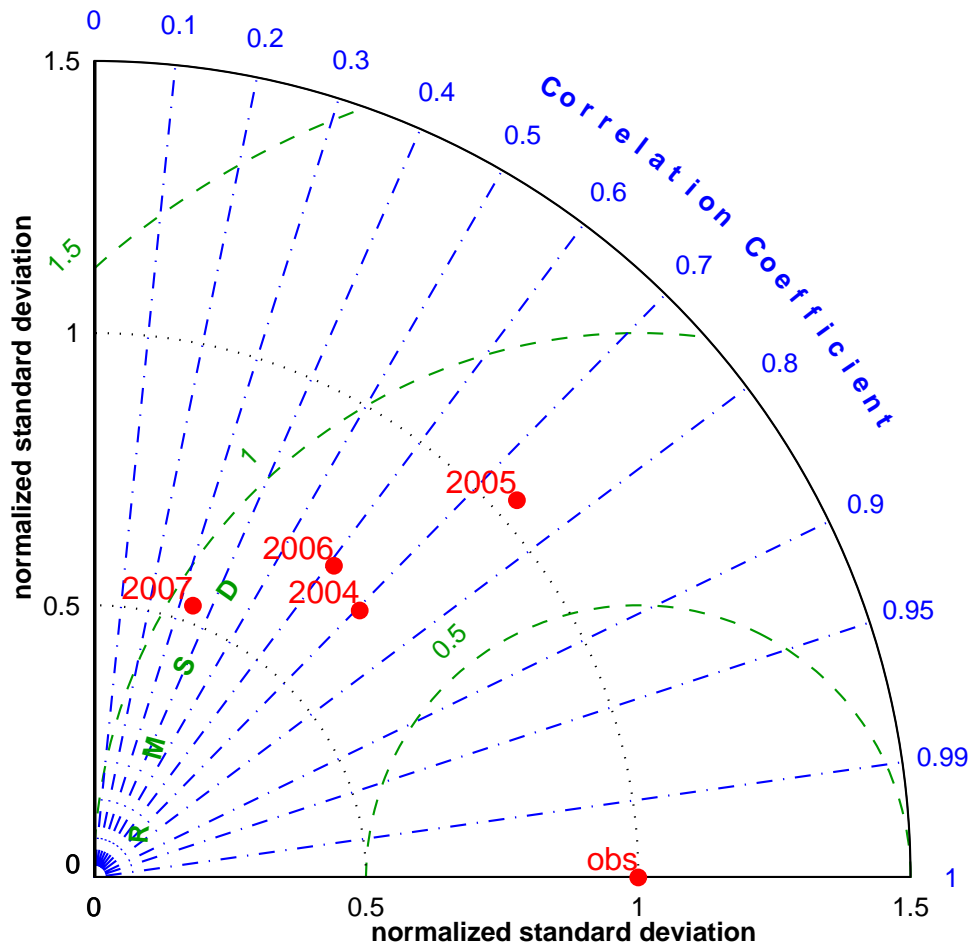


Figure 3. Taylor Diagram for domain-averaged surface chlorophyll concentrations from 2004 to 2007. Radial distance represents the ratio of simulated to observed standard deviations, and azimuthal angle represents model-data correlation. Green arcs represent centered root mean square difference between model and data.

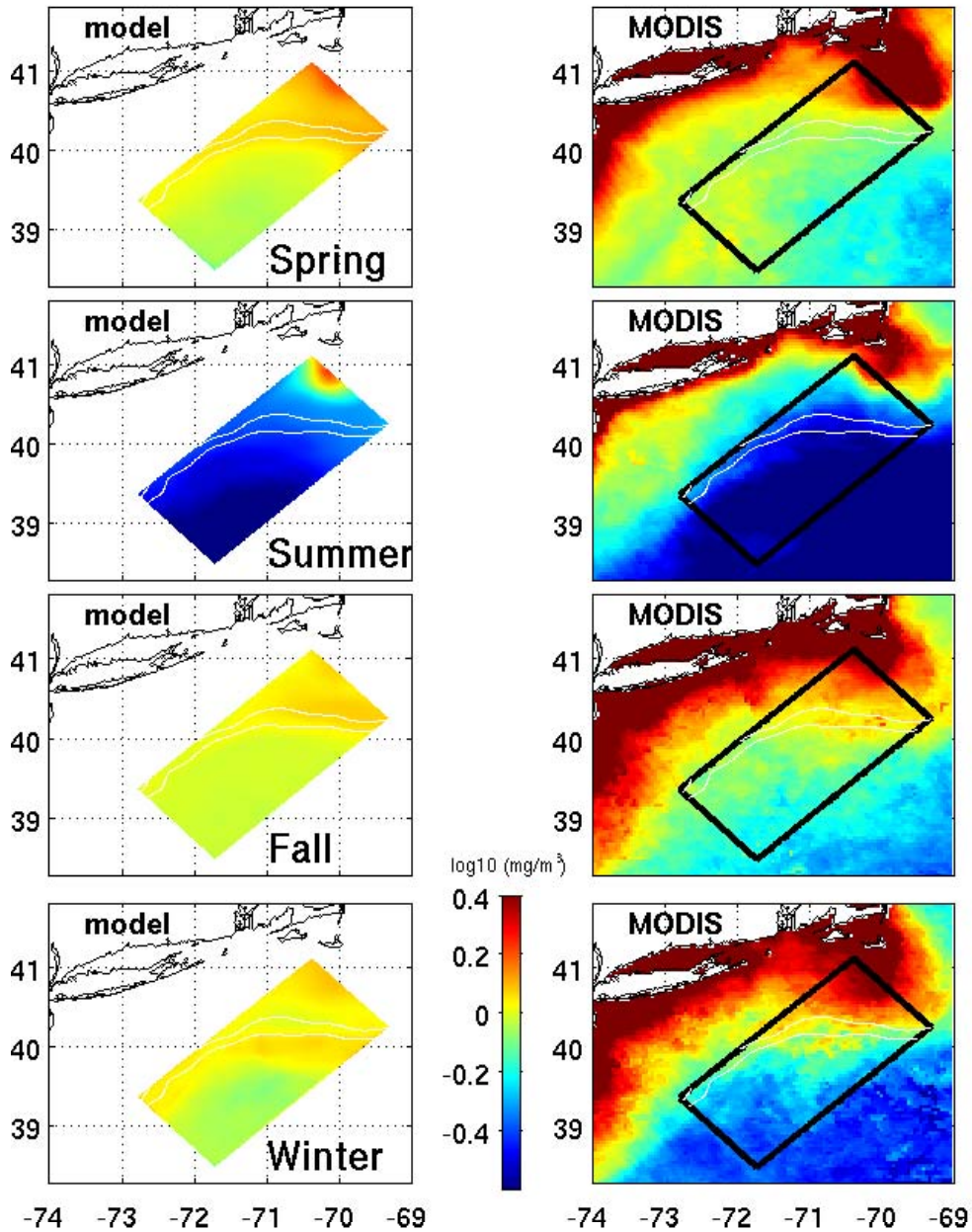


Figure 4. Seasonal surface chlorophyll comparisons based on simulated and observed 4-year mean results. Shown in the left column are model results and those in the right column are MODIS observed results, with the model domain overlaid (black box). 100 and 200 m isobaths are also shown (white curves).

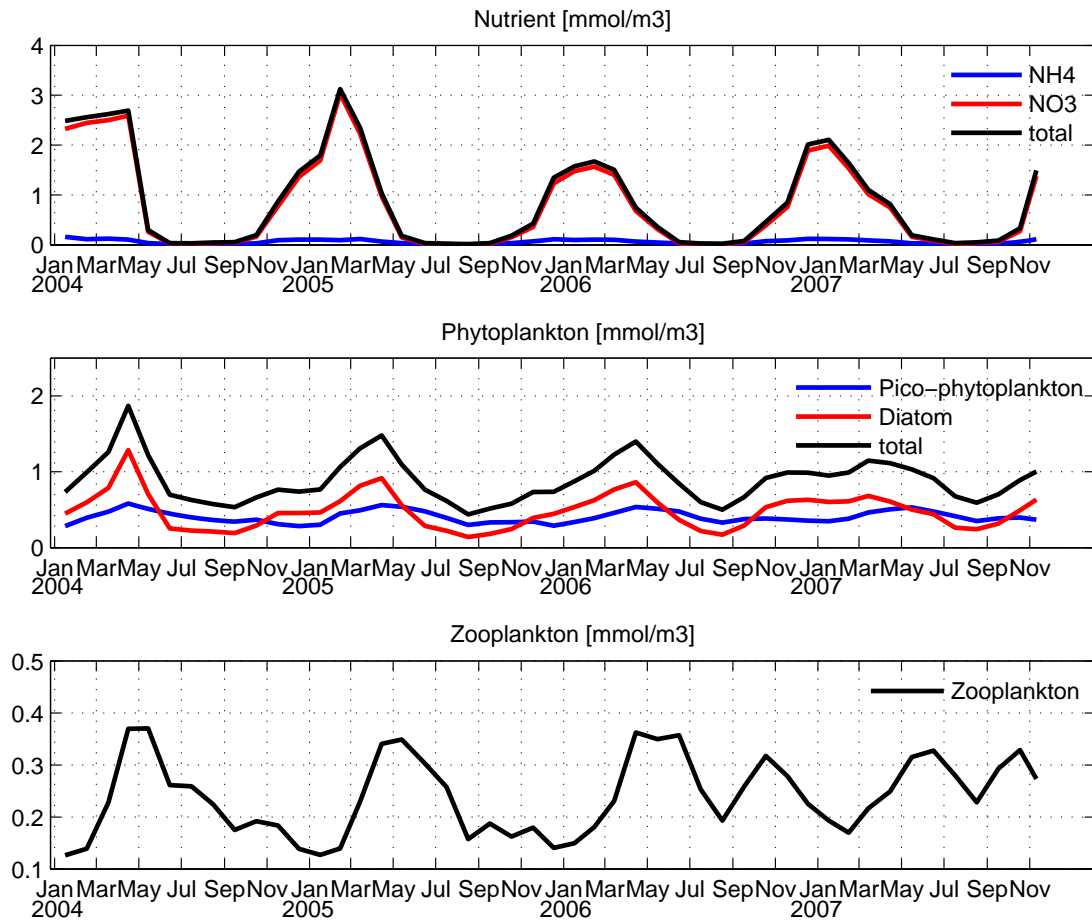


Figure 5. Monthly mean time series of nutrient, phytoplankton and zooplankton components simulated by the model.

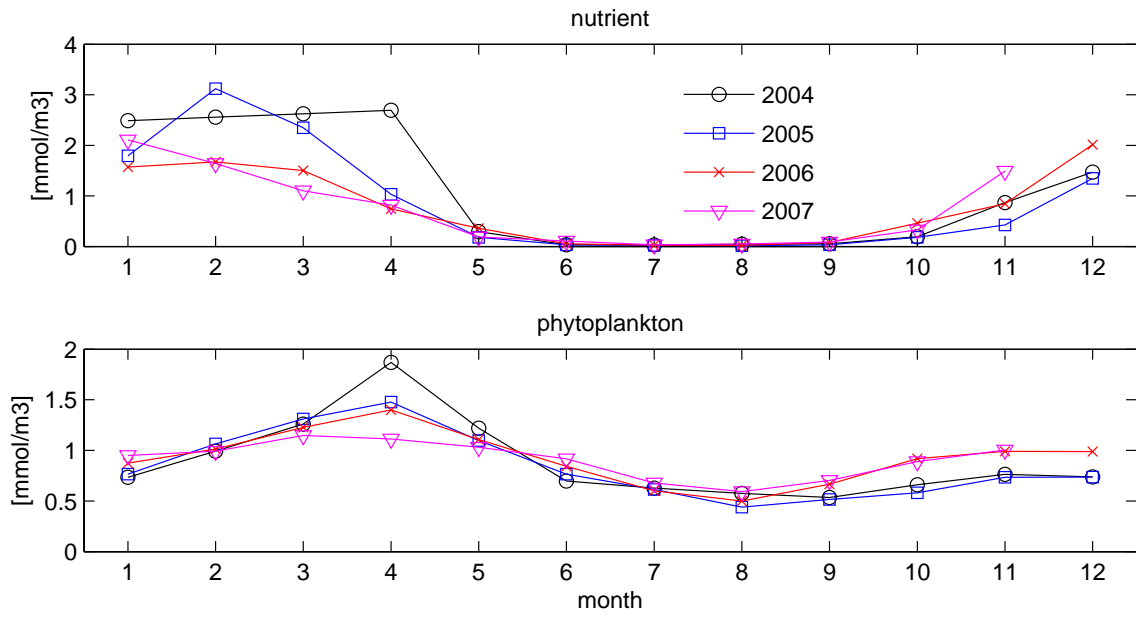


Figure 6. Inter-annual evolution of domain-averaged nutrient concentration (upper panel) and phytoplankton concentration (lower panel) at the MAB shelfbreak.

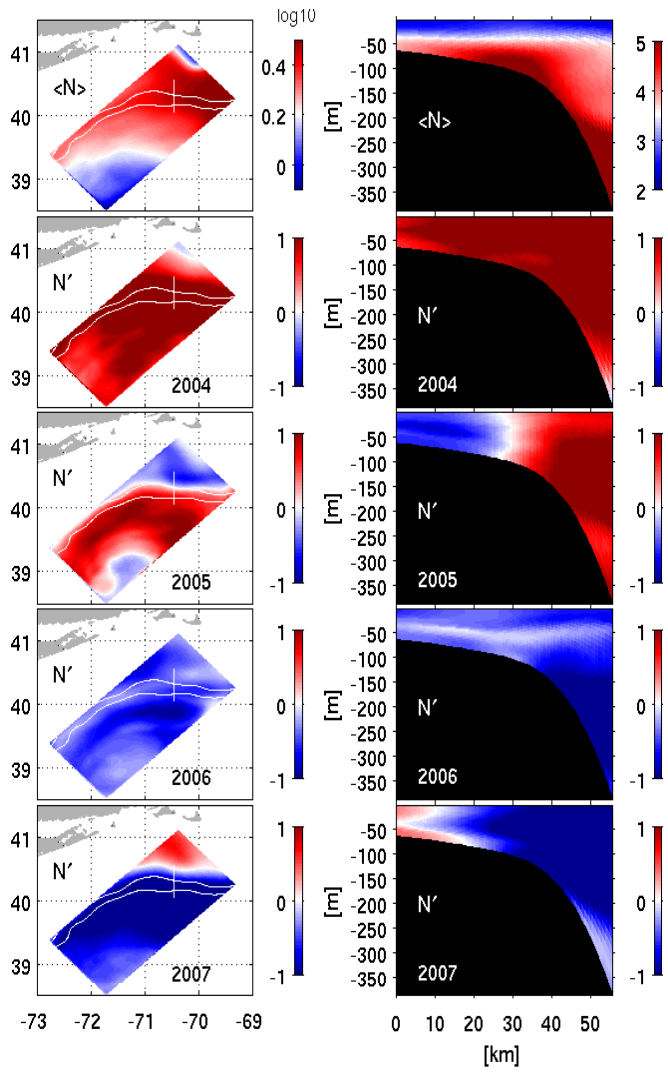


Figure 7. Inter-annual variability of nutrient concentration. Shown in the left from top to bottom are the spring mean upper water column (upper 50 m average) nutrient field averaged over 2004-2007, and the corresponding nutrient anomaly fields in springs 2004 through 2007 relative to their 4-year mean. Shown in the right from top to bottom are the spring mean nutrient field along the Nantucket transect, and the corresponding across-shelf nutrient anomaly fields in springs 2004 through 2007 relative to their 4-year mean. Also shown in the left panels are the location of the Nantucket transect, and 100 and 200 m isobaths (white curves).

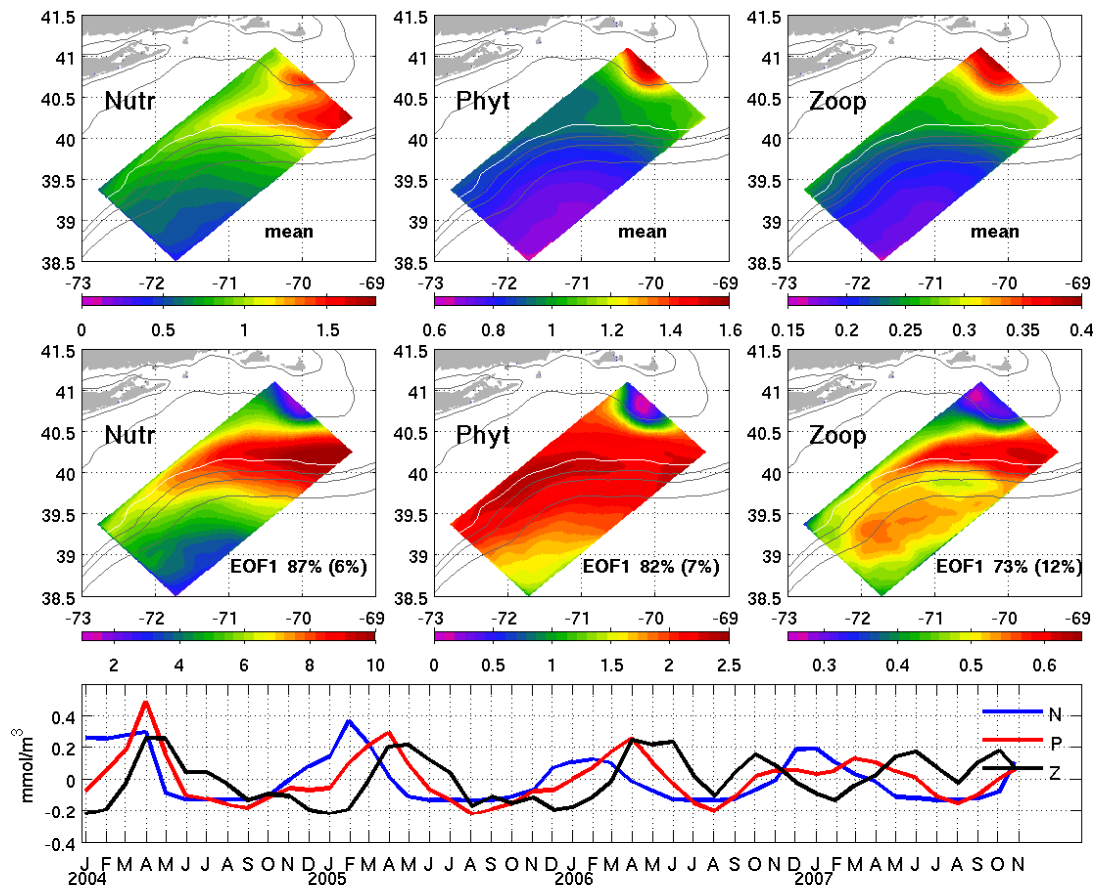


Figure 8. EOF analyses of upper water column (averaged over the upper 50 m) nutrient, phytoplankton and zooplankton fields. Mean fields are shown in the top panels, the first EOF modes with the variance they account for (also shown in the brackets are percentages of 2<sup>nd</sup> mode variance) are shown in the middle panels and their corresponding 1<sup>st</sup> principle components are shown in the bottom panels. Also shown are isobaths (gray curves) with 200 m isobath highlighted in white.

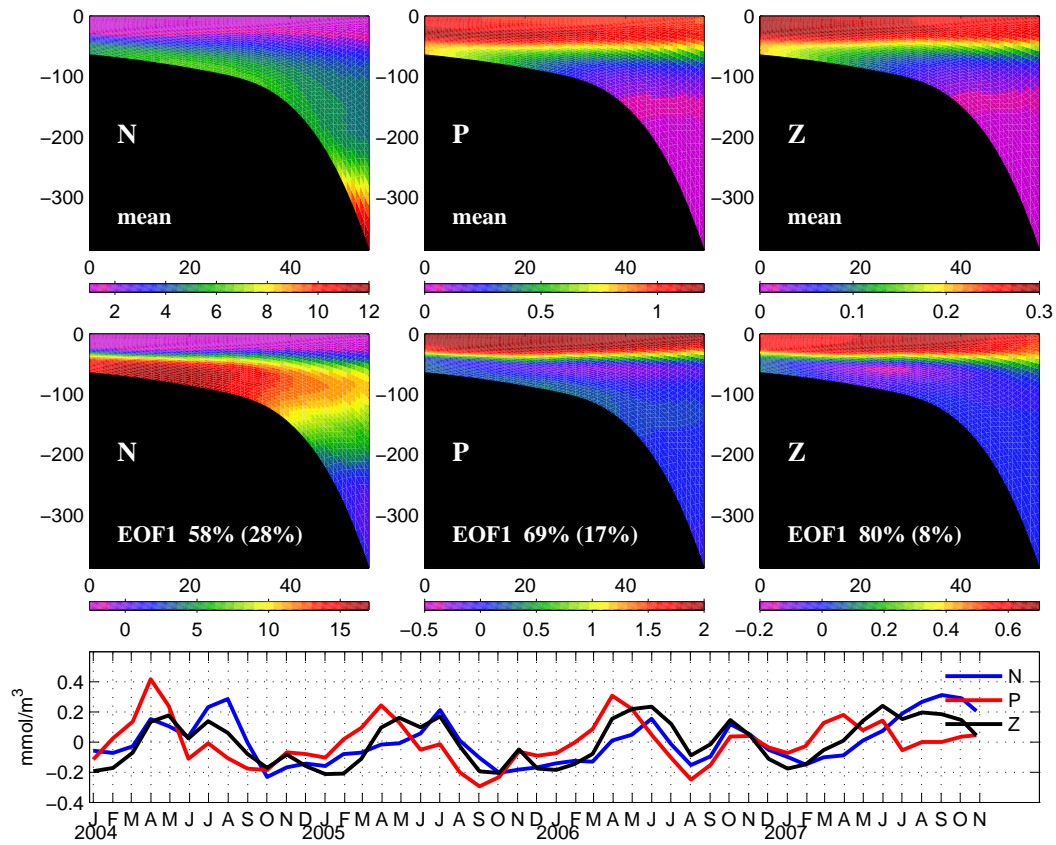


Figure 9. EOF analyses of nutrient, phytoplankton and zooplankton along the Nantucket transect. Their temporal mean fields are shown on the top panels, the first EOF modes are shown in the middle panel with the variance they account for (also shown in the brackets are percentages of 2<sup>nd</sup> mode variance) and the corresponding 1<sup>st</sup> principle components are shown at the bottom panels.

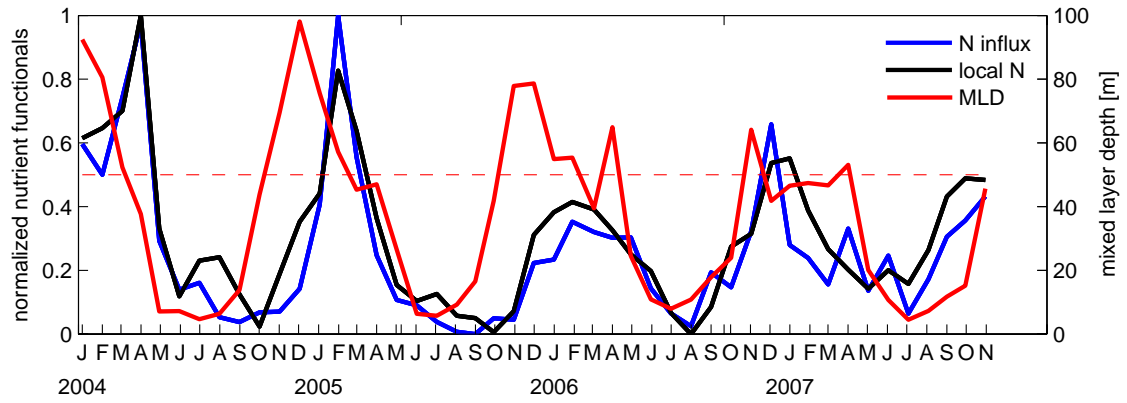


Figure 10. Monthly means of domain-averaged upper 50 m nutrient concentration (solid line), the upstream nutrient influx (dashed line), and mixed layer depth from 2004 to 2007. Both N-influx and local N time series are normalized, whereas the domain-averaged, monthly mean MLD is not and has unit of meter.

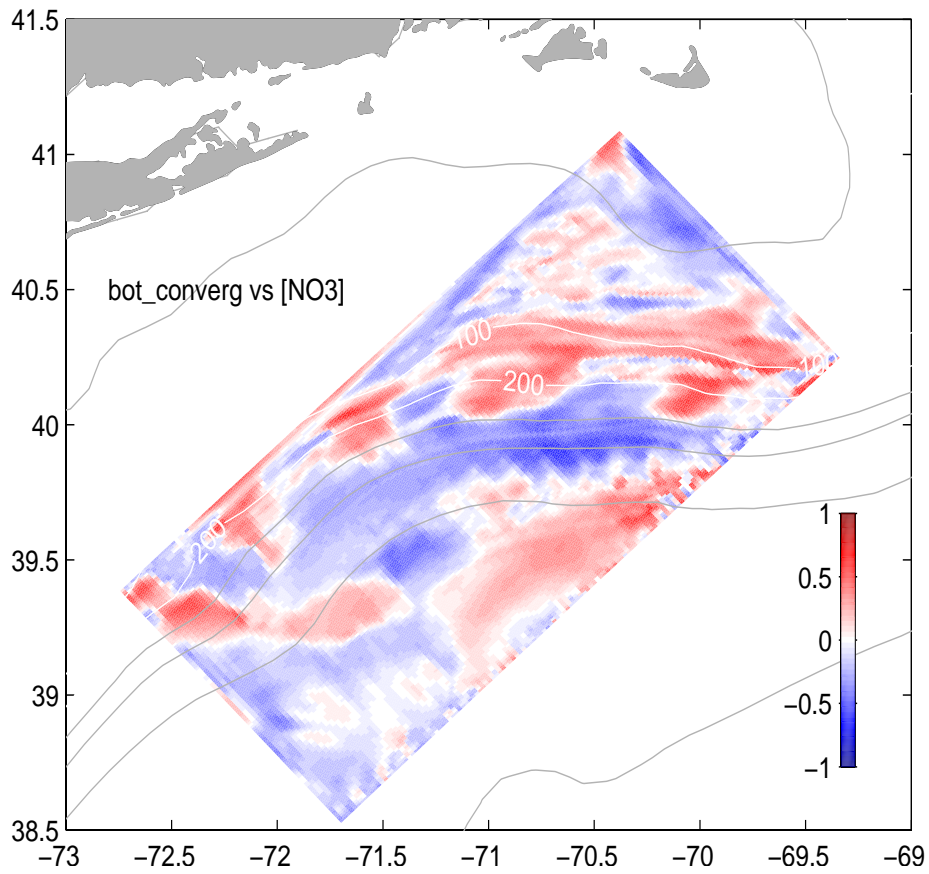


Figure 11. Spatial correlations between the bottom convergence and NO<sub>3</sub> concentration in the upper 50 m. Also shown are isobaths (gray curves) with 100 and 200 m isobaths highlighted in white.

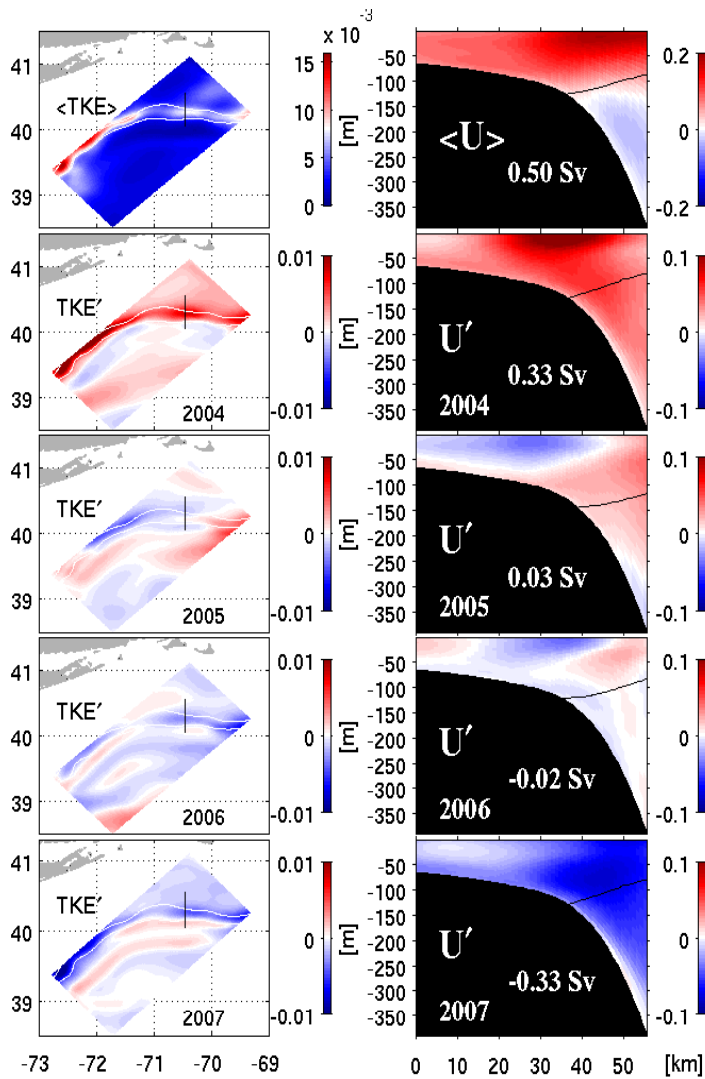


Figure 12. Inter-annual variability of total kinetic energy (TKE: left column) and shelfbreak jet (right column). The top two panels show the spring mean TKE and shelfbreak jet velocity (across the Nantucket transect; positive means westward flow) averaged over 2004-2007. The following panels show the anomaly fields of TKE and shelfbreak jet in springs 2004 through 2007 relative to their respective 4-year means. Also shown in the left hand panels are 100 and 200 m isobaths (white curves) and location of Nantucket transect (black line). The mean  $\langle u \rangle$  and anomaly  $u'$  alongshelf transport values are given in the right-hand panels.

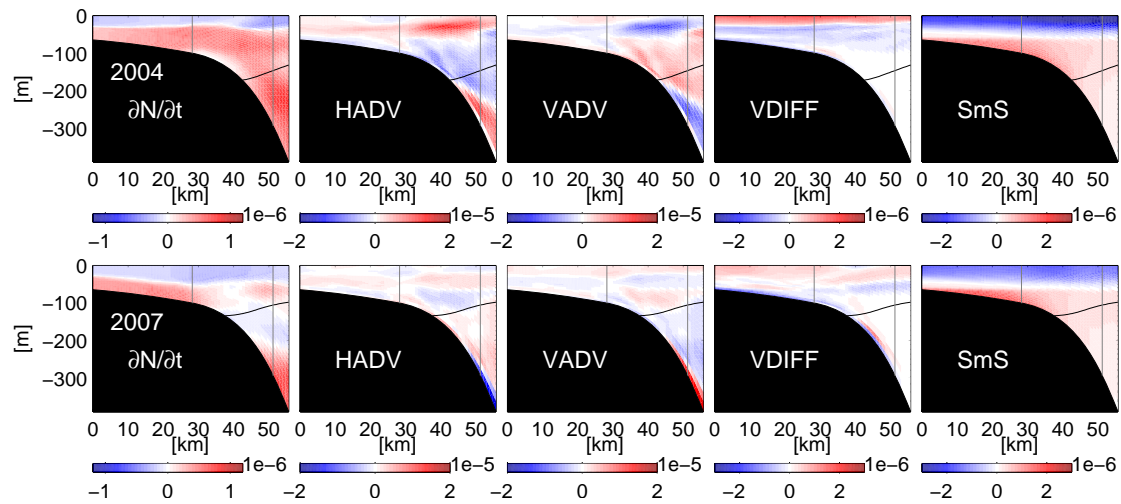


Figure 13. Term-by-term diagnostic analysis of nutrient equation. Shown from left to right are the local rate of change ( $\partial N/\partial t$ ), horizontal advection (HADV), vertical advection (VADV), vertical diffusion (VDIFF), and biological source/sink (SmS) terms averaged over the early spring season (February-March-April) in year 2004 (top panels) and 2007 (bottom panels). The unit for all these terms is  $\text{mmol N}\cdot\text{s}^{-1}$ . The 34.5 isohaline is also shown in each figure as black curve to indicate the position of the shelfbreak front. Two gray vertical lines indicate the locations of 100 and 300m isobaths, between which the shelfbreak jet net nutrient budget terms are computed.

CHAPTER 4: DATA ASSIMILATIVE MODELING INVESTIGATION OF GULF  
STREAM WARM CORE RING INTERACTION WITH CONTINENTAL SHELF AND  
SLOPE, PART 1: METHOD<sup>3</sup>

Ke Chen<sup>a</sup>, Ruoying He<sup>a</sup>, Brian Powell<sup>b</sup> and Andrew Moore<sup>c</sup>

Department of Marine Earth and Atmospheric Sciences, North Carolina State University<sup>a</sup>

Department of Oceanography, University of Hawaii at Manoa<sup>b</sup>

Department of Ocean Sciences, University of California, Santa Cruz<sup>c</sup>

---

<sup>3</sup> This chapter is based on a manuscript to be submitted to Journal of Geophysical Research

## **Abstract**

A shelf-wide realistic data assimilation system was constructed based on latest developed Regional Ocean Modeling System (ROMS) Incremental Strong constraint 4D Variational (IS4DVAR) data assimilation algorithms. The model (MABGOM) encompassing coastal ocean in Northeast US assimilates satellite observed sea surface height and sea surface temperature, in-situ temperature and salinity profiles from expendable bathythermograph, Argo floats, CTD stations and glider transects. Two-month continuous assimilation experiment was performed over April-May 2006, with the focus on Gulf Stream Warm Core Ring (WCR) event. The model skill was significantly refined via data assimilation. SSH (SST) RMS error over the entire assimilation period was reduced by 79% (65%). Comparisons against independent hydrographic data show 62% and 57% improvement for temperature and salinity respectively. The improvements in both observational space and remote areas indicate the successful application of ROMS-IS4DVAR. The data-assimilative MABGOM model well depicted the life span of the WCR and paved the road to further scientific analysis.

## **1. Introduction**

The Mid-Atlantic Bight and Gulf of Maine encompasses the central part of northeastern North America from Cape Hatteras to Nova Scotia. This region lies in the western boundary confluent zone, with subpolar gyre and Labrador current/Scotia shelf water moving south, and subtropical gyre and Gulf Stream moving north, constituting a unique setting for a range of important interdisciplinary oceanography and environmental management issues.

Annual mean shelf transport estimated by *Loder et al.* (1998) shows that there is a systematic reduction in alongshore transport, varying roughly from 7.5 Sv in Labrador Sea to 0.7 Sv off Nova Scotia. There are further reductions in the net transport as Scotian shelf and slope water enter the Gulf of Maine (GOM), and subsequently move into the Middle Atlantic Bight (MAB). Such equatorward transport is accompanied by important yet highly complex cross-shelf transports between the shelf water and the Slope Sea. Several processes have been identified as contributors to the cross-shelf exchange, the most dramatic being Gulf Stream ring interactions with the shelf/slope water front. For

example, *Joyce et al.* (1992) indicates a single ring acting over a short time span (a couple of months) can account for the yearly shelf-ocean transport and flux exchange.

Understanding and quantifying the cross-shelf exchange in this region is critically important as a key to understand the distribution of material properties, particularly the heat-, salt-, nutrient- and carbon fluxes that are vital to the coastal ecosystem. While numerous observational studies (e.g., *Morgan and Bishop*, 1977; *Churchill et al.*, 1986; *Aikamn et al.*, 1988; *Lentz*, 2008) have led to significant progress of understanding, they are limited by temporal or spatial resolutions of observations. The objective of this study is utilizing recently developed data assimilation technique combining available in-situ and remote observation with numerical model to further investigate the costal circulation in the MABGOM region. Particularly, the shelf/slope exchange process during WCR event and WCR-shelfbreak interaction will be the focus of our study.

Our study consists of two parts: part 1 serves as introduction to the data-assimilative model including system setup, evaluation and validation; part 2 presents the interaction of a WCR with continental shelf and slope circulation. We will be focusing on 2006 warm core eddy event in the spring, which is one of the largest one in recent history, and hope to reproduce the WCR process over its life span. We will start in section 2 with the model used for MABGOM and present in section 3 a brief overview of theory underpinning the ROMS IS4DVAR system, as well as observational data and 4DVAR system setup. The system behavior and data assimilation results are described in section 4. Summary and conclusions are given in section 6.

## **2. Model and Configuration**

The Regional Ocean Modeling System (ROMS) is a free-surface, hydrostatic, primitive equation model in widespread use for estuarine, coastal and basin-scale ocean applications ([www.myroms.org/papers](http://www.myroms.org/papers)). ROMS employs split-explicit separation of fast barotropic and slow baroclinic modes, and is formulated in vertically stretched terrain-following coordinates using algorithms described in detail by *Shchepetkin and McWilliams* (2005) and *Haidvogel* (2008). A redefinition of the barotropic pressure-gradient term is also applied in ROMS to reduce the pressure-gradient truncation error. In the present study, our model domain encompasses both the Middle Atlantic Bight and

Gulf of Maine (hereinafter MABGOM model, *He and Chen* (in revision)), bounded by Cape Hatteras in the southwest and Nova Scotia in the northeast. Horizontal resolution is 10km along shelf and 6km cross shelf. Vertically, there are 36 terrain-following levels in the water column with higher resolution near the surface and bottom in order to better resolve ocean boundary layers. We applied the method of *Mellor and Yamada* (1982) to compute vertical turbulent mixing, as well as the quadratic drag formulation for the bottom friction specification.

Open boundary conditions were imposed using daily averaged data from HYCOM (Hybrid Coordinate Ocean Model) NCODA (Naval Research Laboratory Coupled Ocean Data Assimilation) product with  $1/12^\circ$  resolution and 32 vertical z-level. For barotropic mode, the Flather (1976) condition completed with an Orlanski radiation condition (*Chapman*, 1985) is used. For the baroclinic mode, practical aspects of TLROMS and ADROMS calculations prevent us from using the radiation OBC. Instead, clamped boundary conditions are used along with a sponge layer (with higher viscosity) near the boundary to attenuate any wave reflections produced by the clamped conditions. To better constrain the signal from open boundaries, climatological tracer nudging is also applied within the sponge layers, with a relaxation time scale of 2-day. Due to the systematic salinity bias on the continental shelf, NCODA dataset are corrected against HydroBase (*Curry*, 2001) climatology before serving as initial and boundary conditions as well as climatology (*He and Chen*, in revision). The annual mean of temperature and salinity from NCODA dataset are replaced by annual means from HydroBase while the daily variations are retained. In addition, along west and east open boundaries, HydroBase annual mean temperature and salinity are used to compute mean dynamic height and associated geostrophic transport to replace corresponding annual means from NCODA data.

Surface forcing data are provided from National Oceanic and Atmospheric Administration (NOAA) National Center for Environment Prediction (NCEP) North America Regional Reanalysis (NARR), which has spatial and temporal resolution of 35 km and 3 hour, respectively. Air-Sea fluxes of momentum and buoyancy were computed from the standard bulk flux formulas (*Fairall et al.*, 2003) using NARR archive including surface winds, air temperature, air pressure, relative humidity, air pressure, short wave

radiation, long wave radiation, cloud coverage and precipitation. Surface net heat flux is further corrected based on NOAA blended SST with a relaxation timescale of 0.5 day (*He and Chen*, in revision; *Chen and He*, 2010). Fresh water runoff from 9 major rivers in the area was also considered. These include St Johns River, Penobscot River, Kennebec River, Androscoggin River, Merrimack River, Connecticut River, Hudson River, Delaware River and Potomac River. For each of them, United State Geological Survey (USGS) real-time river runoff measurement was collected to specify freshwater volume transport.

The data assimilation experiment is based on the MABGOM forward simulation (*He and Chen*, in revision), from Jan 1<sup>st</sup> 2004 to Dec 31<sup>st</sup> 2007, after 2-month spin-up with HYCOM NCODA hindcast. The performance of data Assimilation relies upon the model physics to match the observations, therefore, the forward model must be capable of resolving the basic dynamics. Detailed model validations can be referred to *He and Chen* (in revision), in which the MABGOM forward solutions are compared to extensive observations including coastal sea level, satellite altimeter data, mooring data, glider hydrographic data, and long-term mean along-shelf currents. The mean dynamics and long term, low frequency variability of the MABGOM are captured well while the model has difficulty in simulating short duration processes because other than surface forcing there is no time-dependent connection with the actual circulation. The mean sea surface height anomaly over April to May in 2006 (**figure 2**) from the forward model compares well to that from the observations. They are both capable of capturing the mean basic hydrodynamic patterns in the MAB and GOM region at this time of the year. The Gulf Stream, the relative low SSH in the slope sea and relative high SSH along the coast which is probably related to the combined effect of river runoff and thermal expansion, are all well depicted. The model also resolves the mean Gulf Stream eddy, but the eddy position is more to the southwest and closer to Gulf Stream, compared to satellite observations. In order to better resolve the dynamical processes in the MAB and GOM, particularly the WCR, we will need data assimilation procedure to correct time-dependent flow of the model.

### 3. 4D Variational Data Assimilation

#### 3.1. ROMS-IS4DVAR

The Regional Ocean Modeling System (ROMS) has been recently extended with 4D Variational Data Assimilation (4DVAR) functionality. The ROMS-4DVAR system including the original nonlinear model (NLROMS), tangent linear model (TLROMS) and adjoint model (ADROMS) provides opportunities for conducting various types of analysis on complex ocean circulations (*Moore et al., 2004; Di Lorenzo et al., 2007; Powell et al., 2008; Broquet et al., 2009; Moore et al., 2011b*).

The ROMS-IS4DVAR system is based on the incremental formulation described by Weaver et al. (2003). We present here an overview of important concepts of this system, to aid discussion in later sections. Specific details about the implementation in ROMS can be found in *Powell et al. (2008)* and *Moore et al. (2011a)*. Let us denote the model state vector as  $\mathbf{x}$ , composed of the prognostic variables: the sea surface height  $\zeta$  at all model grid horizontal locations, and the potential temperature  $T$  and the salinity  $S$ , and the velocities  $(u, v)$ , at all model grid 3D locations, such as  $\mathbf{x} = (\zeta, T, S, u, v)^T$  where superscript T denotes vector transpose. We represent the NLROMS symbolically as  $(\partial\mathbf{x}/\partial t) = M(\mathbf{x})$  where  $M$  denotes the model operators.

The goal of 4DVAR is to identify the best estimate circulation, also referred to as the analysis or posterior, namely  $\mathbf{x}^a(t)$ , that minimizes in a least-squares sense, the difference between the model and the observations and a background. The solution,  $\mathbf{x}(t_i)$ , of NLROMS that describes  $\mathbf{x}^a$  will depend upon the choice of initial conditions,  $\mathbf{x}(t_0)$ , surface forcing,  $\mathbf{f}(t)$ , and boundary conditions,  $\mathbf{b}(t)$ , all of which are subject to errors and uncertainties. As such,  $\mathbf{x}(t_0)$ ,  $\mathbf{f}(t)$  and  $\mathbf{b}(t)$  are referred as control variables, and the problem in 4DVAR is reduced to identifying the appropriate combination of control variables that yield the best estimate  $\mathbf{x}^a(t)$ .

In the incremental 4DVAR approach, we seek to minimize the quadratic cost function  $J=J_b+J_o$ , given by

$$J_b = \frac{1}{2} \delta\mathbf{x}(t_0)^T \mathbf{B}^{-1} \delta\mathbf{x}(t_0) \dots\dots\dots (1)$$

$$J_o = \frac{1}{2} \sum_{i=1}^{N_{\text{obs}}} (\mathbf{G}_i \delta\mathbf{x}(t_i) - \mathbf{d}_i)^T \mathbf{R}_i^{-1} (\mathbf{G}_i \delta\mathbf{x}(t_i) - \mathbf{d}_i) \dots\dots\dots (2)$$

Where  $G_i$  is tangent linear model sampled at observational space.  $\mathbf{d}_i = \mathbf{y}_i - \mathbf{H}_i \mathbf{x}(t_i)$  are the innovation vectors, where  $\mathbf{y}_i$  is  $i$ th observation in space and time,  $t_i$  is the observation time, and  $\mathbf{H}_i$  is an operator that samples NLM trajectory at observation locations.  $\mathbf{B}$  and  $\mathbf{R}_i$  are respectively model background and observation error covariance matrix, as will be discussed later. We seek a solution  $\delta \mathbf{x}^a$  for which the total cost function the gradient of  $J$  vanishes and  $J$  reaches a minimum value.  $\delta \mathbf{x}^a$  is identified iteratively by solving a sequence of linear least squares minimizations (inner-loops) repeated with periodic updates of  $\mathbf{G}$  (outer-loops). In ROMS-4DVAR a conjugate-gradient (CG) algorithm based on *Fisher* (1998) is used to achieve the minimization. The minimization procedure is terminated when  $\|\nabla J\| \leq \epsilon$ . This typically requires a large number of iterations which is generally not affordable, so instead the number of outer-loops and the number of inner-loops used during each outer-loop were fixed to yield a good estimate of the minimum of  $J$ . During each inner-loop, TLROMS is used to propagate the increments forward in time to evaluate (2), and ADROMS yields  $\nabla J(\delta \mathbf{x})$ , which is used by the CG algorithm to identify the minimum of  $J$ . The best estimate  $\delta \mathbf{x}^a$  will be found at the end of iteration. In this paper, the ROMS-4DVAR is allowed to adjust the initial, boundary and surface forcing, so the optimal increment  $\delta \mathbf{x}^a$  is applied to initial, boundary and surface conditions respectively after minimization process.

Data assimilation is typically performed over many assimilation cycles that span the entire analysis period (**Figure 3**), thus in each assimilation cycle the tangent linear approximation is valid given the relative short assimilation window. At the beginning of each assimilation window, the initial condition derived from previous window (or directly given for the first window) is used to compute a forecast with NLROMS. This forecast provides the background trajectory or the optimal model trajectory when observational data is only available to the last assimilation window. Then ROMS-4DVAR inner loop starts with CG algorithm to yield an estimate of optimal increment  $\delta \mathbf{x}^a$  which will be used to adjust control vectors. The adjusted control vectors are further used to compute the model trajectory after all designated outer and inner loops.

### 3.2. Observational data

Observations from various different instruments and satellite platforms were assimilated to constrain the WCR. These include:

*AVISO Sea Surface Height (SSH):* AVISO SSH anomaly is a merged product comprised of data from TOPEX/Poseidon, Jason-1, Envisat and GFO measurements. Original data are available every 3-4 days with horizontal resolution  $1/3^\circ$ . To better constrain the model, we linearly interpolated original data to daily basis. The anomalies are further converted to dynamic height by adding mean sea level computed from MABGOM simulation 2004-2007. Moreover, considering the data quality of satellite altimeter product, coastal data that lie shoreward 200m isobaths are excluded from assimilation. By eliminating coastal data, we hope to reduce relatively large uncertainties due to interpolation scheme and unrealistic model-observation misfit (**Figure 2**). An observation error standard deviation of 2 cm is used for SSH measurements, as it is the usual measurement precision associated with altimetric data.

*Blended SST data:* The SST product used is a blend of data from the GEOS, AVHRR and MODIS satellite instruments and was developed at the CoastWatch/NOAA Fisheries. Blended SST estimates were available from July 2002 every day as a 5 day mean product with horizontal resolution of 10 km. A standard deviation of  $0.4^\circ\text{C}$  is used.

*In situ T and S profile data:* Quality controlled data from the European Union ENSEMBLES project (EN3) archived at the UK Met Office (*Ingleby and Huddleston, 2007*) were also used. Within the domain spanned by MABGOM, EN3 contains in situ observations from a variety of instruments, platforms and sources that include mechanical and expendable bathythermographs (denoted XBT), Argo floats, and Conductivity, Temperature, Depth (CTD) profiles from the World Ocean Data (WOD) 2005, the Global Temperature-204 Salinity Profile Program (GTSP), and the USGODAE Argo Global Data Assembly Centers (GDAC). Other miscellaneous hydrographic data from volunteer observing ships are also included in EN3.  $0.1^\circ\text{C}$  and 0.1 psu are the observation error standard deviation for in-situ temperature and salinity data respectively.

*Endurance Line glider T and S data:* Repeated surveys over the shelf of New Jersey were conducted beginning in November 2003, along Rutgers University Endurance Line (**Figure 1**). The Endurance Line is approximately 120km long, generally extending from 20m isobaths to the shelfbreak. Hydrographic data were collected using a fleet of Slocum

Coastal Electric Gliders, which cycle from the surface to 3–5 m above the bottom while moving forward at an average speed of 24 km per day. The glider data (*Castelao et al.*, 2008) used here are temporal averages of original Endurance line data which otherwise have durations of weeks. Six realizations (Apr 9<sup>th</sup>, 15<sup>th</sup>, 19<sup>th</sup>, 22<sup>nd</sup>, 29<sup>th</sup> and May 20<sup>th</sup>) of cross-section of temperature and salinity are assimilated. Observational error of 0.1 °C and 0.1 psu are used for temperature and salinity, respectively.

*Line-W CTD data:* Line-W, operated by Woods Hole Oceanographic Institution, is one component of long-term climate observing system located on the continental slope south of New England (**Figure 1**). Line-W contains an array of moored instruments and also shipboard observations. The temperature and salinity observations used in this study include 17 stations of shipboard CTD observation, from Oceanus cruise 421 in April 2006. The cruise covering from the shelfbreak to the slope started on Apr 5<sup>th</sup> and ended on Apr 15<sup>th</sup> 2006, during which period a Warm Core Ring was located in the slope sea. For CTD measurements, we used 0.1 °C and 0.1 psu as observational error for temperature and salinity respectively.

All observations are combined before assimilation, and were further respectively averaged to form “super observations” that within each model grid cell and at each timestep each type of observation only has one realization, to reduce data redundancy. The standard deviation of the observations that contribute to each super observation was used as a measure of the error of representativeness.

The spatial distributions of super observations of SSH, SST and UK MET office T/S profiles are shown in **Figure 4**. SSH and SST on the first day of DA run are shown while positions of all available in-situ temperature and salinity profiles are indicated by diamonds with color being their surface values. On Apr1st, 2006, a Gulf Stream meander already formed and was located in the deep sea close to the continental slope region. The sea surface height in the center of the meander is ~0.6m higher than the surrounding slope sea and the surface temperature of the ring is ~10°C higher than ambient slope water. During the assimilation period, in-situ temperature profiles are available all across the MAB and GOM while more temperature profiles are located in the GOM. As for salinity observations, most of the data are available in the GOM and northern MAB. The temporal distributions of super observations (**Figure 5**) show the majority of observations feeding

the DA system are satellite observed SST with total number of realizations 574817. Due to the lower spatial resolution ( $\sim 1/3$  fold) and exclusion of coastal data, the number of SSH realizations is 41880. The in-situ temperature and salinity profiles contribute 23870 and 20243 observations. Endurance line glider data provide 4932 temperature and salinity realizations and Line-W CTD data have a number of 966 observations including both temperature and salinity. While the T/S profile data are less in number, they provide important subsurface information to correct model hydrodynamics.

### 3.3. Data Assimilation Setup

#### 3.3.1. Covariance modeling

The parameterization of model background error covariance matrix  $\mathbf{B}$  significantly determines the way that observational information is extrapolated to non-observational variables thus a proper  $\mathbf{B}$  has critical influence on the data assimilation performance.  $\mathbf{B}$  contains initial condition background (or prior) error covariance matrix  $\mathbf{B}_x$ , open boundary condition background error covariance matrix  $\mathbf{B}_b$ , surface forcing background error covariance matrix  $\mathbf{B}_f$ , and prior model error covariance matrix  $\mathbf{Q}$  (serves for weak constraint 4DVAR). Each error covariance matrix can be expressed as  $\mathbf{B} = \Sigma \mathbf{C} \Sigma$ , where  $\Sigma$  is diagonal matrix of error standard deviations, and  $\mathbf{C}$  is a univariate correlation matrix. The main source of background error is due to the model bias and spatial mismatch from the observations. Sensitivity experiments tell that in order for the forward model to resolve the circulation accurately, particularly the eddy pattern, climatological nudging is needed. Meanwhile, large climatological nudging would possibly introduce bias from HYCOM NCODA data, especially near coastal regions. To reduce model bias that might be induced from climatological nudging while at the same time reduce the model/observation mismatch, a trade-off configuration is implementing a nudging zone within the sponge layers along three open boundaries. Thus, the eddy information can be passed into the MABGOM model smoothly and a relative small nudging zone prevents much bias introduced into the model interior. The standard deviation  $\Sigma$  is then computed on a monthly basis using MABGOM forward simulation over 2004-2007, such that the seasonal cycle is removed from  $\Sigma$ . The univariate correlation matrix is further factorized

as  $C = \Lambda L_v^{1/2} L_h^{1/2} W^{-1} L_v^{T/2} L_h^{T/2} \Lambda$ , where  $\Lambda$  is a matrix of normalization coefficients,  $L_v$  ( $L_h$ ) is vertical (horizontal) correlation function,  $w$  is the diagonal matrix of grid volumes (*Moore et al.*, 2011a). The correlation matrices,  $L_v$  and  $L_h$ , with their associated normalization factors  $\Lambda$ , were computed as solutions of diffusion equations following *Derber and Rosati* (1989) and *Weaver and Courtier* (2001). The length scales chosen for  $L_v$  and  $L_h$  represent the decorrelation scale from a typical increment, and are currently assumed to be homogenous and isotropic. In current setup, a length scale of 50km is chosen for  $L_h$ , which is a reasonable number since the focus here is the WCR. 30m is set as the length scale for  $L_v$ . Theoretically, solutions will be smoother using larger length scales.

### 3.3.2. Assimilation cycle

To reproduce the warm core eddy event in summer 2006, we chose to run ROMS-4DVAR from Apr1<sup>st</sup>, 2006 to May 31<sup>st</sup>, 2006, covering the entire life span of eddy, including Gulf Stream Meander, detachment of meander, formation of ring, interaction of WCR and shelfbreak, retreatment and re-attachment with Gulf Stream. An assimilation window of 3-day is chosen, short enough to guarantee tangent linear approximation (*Wilkin et al.*, 2008; *Powell et al.*, 2008; *Broquet et al.*, 2009). Meanwhile, we choose 1-day as overlap between assimilation windows (**Figure 3**). Thus 3 days of observations can be utilized during each window and the starting snapshot of the 3<sup>rd</sup> day serves as initial guess for the next assimilation window. Via overlapping, more observational data are used (compared to no-overlap case) and the initial condition for the next window should not drift too far from observations. So that during the assimilation period, 30-window of assimilation were performed individually and the posterior information can be carried on from one window to the next.

The number of inner- and outer-loops used is a trade-off between computational cost, the level of convergence of the CG algorithm, and the need to update the cost function shape. Sensitivity experiments found that using several outer-loops had a weak influence on the cost function convergence, in that for a given total number of loops (i.e. the product of the number of inner-loops and outer-loops), the final cost function was similar

irrespective of the combination of inner- and outer-loops. In our case, we chose 2 outer loops and 8 inner loops for each assimilation window. So the nonlinearity will be updated one time during assimilation windows. We also found that  $\sim 16$  loops in total (inner-times outer-loops) was sufficient to yield an acceptable estimate for the minimum of  $J$ , in the sense that the rate of change in  $J$  indicated that differences between its final value and the optimal solution are small (less than 1%) compared with the difference between the initial and final values.

## 4. Results

### 4.1. Cost function behavior

By minimizing the cost function to seek an optimal value, in a least square sense, we obtain the solution that best represents the observations. This is the essential goal of 4DVAR. The performance of MABGOM 4DVAR system can be initially evaluated based on cost function evolutions (**Figure 6**). As we can see, during the first assimilation window starting on April 1<sup>st</sup>, 2006, the total cost function is effectively reduced. The maximum reduction of cost function lies in the first 5 inner loops, with percentage of reduction ranging from more than 40% to about 5%. After 10 inner loops, the reduction of cost function stays below 5% and approaches zero in the 16th inner loop. This suggests in our case 2 outer loops with 8 inner loops is good enough to yield a good minimization of cost function. The theoretical minimum value  $J_{\min}$  of total cost function  $J$  ( $J_b + J_o$ ) is estimated as  $N_{\text{obs}}/2$  (Weaver *et al.*, 2003), in which  $N_{\text{obs}}$  is the number of assimilated observations in each window. In our case, after 16 inner loops, the final value of cost function is above the theoretical value, which is common in 4DVAR data assimilation. By data assimilation, we expect to decrease the difference between the model and observation and the cost function will become smaller with assimilation window moving on. The total cost function (**Figure 6**) in the last assimilation window is smaller than that in the first window and the final value approaches the  $J_{\min}$ , indicating a good fitting to the observations. Overall, total reductions of 80% and 69% of cost functions in window 1 and window 30 respectively indicate the DA system efficiently reduced the model error. Meanwhile, the final value of non-linear cost function approximately coincide with  $J$ , indicating the choice of 3-day for tangent linear approximation is well-grounded.

The behavior of cost function depends closely on the parameterization of **B** and **R**. In our DA experiments, background cost function  $J_b$  is much larger than observational cost function  $J_o$ . This indicates that the background error **B**, which is estimated intrinsically based on MABGOM forward model hindcast, is relatively overestimated. As a result,  $J_o$  dominates  $J$  and  $J_b$  continues to increase even though  $J$  already approaches its minimum, which will lead the model to deviate from its background value. Sensitivity experiments show termination of DA at 16th inner-loop would prevent too much deviation of the model and yield good fitting of total cost function. The overall performance of cost functions in both windows shows our choice of background error and observational error appears justified.

## 4.2. Assimilation Statistics

### 4.2.1. Surface Performance

The improvement of simulated circulation from MABGOM 4DVAR system can be evaluated by Root Mean Square Error  $\sqrt{\frac{1}{N} \sum_{i=1}^N (x_i - y_i)^2}$  (RMSE, thereafter).  $x_i$  and  $y_i$  are the  $i$ th model data and observation data at the time and location of observation. Prior and posterior RMSE in the entire assimilation period are compared.

In order to gain a view how the DA system performs in terms of reducing RMSE, spatial distribution of surface fields are depicted. During the assimilation period, linearly interpolated SSH observations are available on a daily basis. The spatial RMSE of SSH is calculated at each observation locations based on 60 realizations (**Figure 7**). Large RMSE between observations and forward model exists in the Gulf Stream region, especially to the north of Cape Hatteras, and its meander region. In other regions, e.g., northern continental slope, the error is very small or close to zero. The mismatch between MABGOM forward model and satellite observations near the Gulf Stream and its frontal regions indicates without DA constraint, the forward model would drift from correct trajectory, which is a common phenomenon in numerical modeling (e.g. *Zhai et al*, 2004). A maximum value larger than 0.6m suggests the model predicted meander/eddy location is off the observation. After all inner loops are completed, the initial condition, boundary

condition as well as surface forcing during the assimilation window are optimally adjusted and will drive the forward model to seek posterior solutions. The RMSE between the posterior solutions and observations is effectively reduced (**Figure 7**). The approximate RMSE of SSH after DA is close to zero in most areas of the domain. The error is slightly larger in the Gulf Stream/Slope region where Gulf Stream meander and eddy shedding processes are active. Even so, the maximum RMSE value sits below 0.3m, which is much smaller compared to SSH RMSE from the forward model.

The performance of DA system is also evaluated in time series of spatial RMSE. At each time when SSH observations are available, spatial RMSE is calculated based on realizations at all assimilated observation locations. As shown in **Figure 7**, the RMSE between the forward model and observations ranges from more than 0.1m to 0.4m, indicating the forward model alone is not capable of resolving the surface elevation correctly. Large SSH error would hinder further sensible analysis, especially WCR evolution and its role in the coastal region. By assimilating SSH data, RMSE was effectively reduced. The DA prior RMSE was reduced immediately after the first assimilation window from  $\sim 0.18\text{m}$  to  $\sim 0.1\text{m}$  and stay around 0.1m in all other assimilation windows. In comparison, the mean SSH RMSE from DA posterior is smaller than that of prior and stays below 0.1m, though some fluctuations are observed due to the adjustment made by data assimilation.

Temporal and spatial SST RMSEs (**Figure 8**) are also calculated using the same algorithms. The SST from the forward model is generally consistent with the observations in the regions of continental shelf and deep slope sea. A relatively large discrepancy between forward model and satellite observation lies in the Gulf Stream/WCR frontal region, with maximum RMSE up to  $6^{\circ}\text{C}$ . This is most likely due to the insufficient capability of forward model in resolving the location of strong western boundary current and its related meander/WCR. After data assimilation, the RMSE of SST has been greatly reduced, to a state with maximum value around  $3^{\circ}\text{C}$ . Most of the errors still exist at the frontal region, along Gulf Stream boundary and continental shelfbreak, but the errors have already been significantly reduced to  $\sim 1^{\circ}\text{C}$  or less. Time series of spatial RMSE of SST show that the forward model has relative larger SST RMSE, ranging from

~1°C to ~2.5°C. The RMSE of SST from DA prior again immediately decreases after the first assimilation window, dropping from ~2°C to ~1°C. In comparison, the SST RMSE is further reduced in DA posterior, with average value below 1°C. The comparison of RMSEs of both SSH and SST demonstrated that the surface fields are well constrained and justified the performance of our DA system.

#### 4.2.2. Subsurface Performance

Gulf Stream Warm Core Rings have large impact on the coast environment and induce shelf slope exchange processes not only in the surface but also in the subsurface. It is vital to get the subsurface fields right in order to correctly characterize those processes. We next will examine the performance of 4DVAR data assimilation in terms of subsurface fields. One statistic usually used is model-observation error

bias  $\frac{1}{N} \sum_{i=1}^N (x_i - y_i)$ , where  $N$  is the number of assimilated observation of any state variable,  $x_i$  and  $y_i$  are state variable from model and observation respectively. The error bias which reflects average discrepancy between model output and observations is one component of RMSE (Taylor, 2001), in that  $(\text{RMSE})^2 = (\text{Error Bias})^2 + (\text{Error STD})^2$ .

Here error STD is denoted as  $(\frac{1}{N} \sum_{i=1}^N (x_i - \bar{x} - y_i - \bar{y})^2)^{\frac{1}{2}}$ , where  $\bar{x} = \frac{1}{N} \sum_{i=1}^N (x_i)$

and  $\bar{y} = \frac{1}{N} \sum_{i=1}^N (y_i)$ . Different from RMSE, error bias could provide more specific

information whether the model overshoots or undershoots.

Biases of assimilated in-situ temperature and salinity, including T/S profiles from UK MET office, glider T/S along Endurance line and shipboard CTD observations from Line-W archive, are compared to evaluate the subsurface performance of the model (**Figure 9**). Since most temperature and salinity profiles are located on the continental shelf (**Figure 4**), below we only focus on the performance of assimilating shelf T/S profiles. Assimilated temperature data (salinity) in the entire 2-month assimilation period are categorized into different vertical layers with layer interval of 10m. Thus temporal bias in each layer can be calculated to show the vertical pattern of temperature (salinity). At the sea surface, temperature from the forward model has a bias of 1.5°C, suggesting the

model overestimates surface temperature. Temperature bias decreases at depth and turns to be negative around ~40m. Temperature bias becomes more negative with depth and exceeds  $-2^{\circ}\text{C}$  below ~150m. The vertical distribution of temperature bias shows the forward model alone will overshoot thermal structure in the upper 40m while undershoot below 40m. This would intensify the thermocline and further introduce error in further calculation. In comparison, temperature bias in the DA prior was reduced to  $\sim 1^{\circ}\text{C}$  at surface and the negative bias was reduced below 50m, showing the 4DVAR adjusted model state provided good initial condition for improving forecast skill. Lastly, the DA posterior driven by optimally adjusted initial and boundary condition as well as surface forcing, significantly reduced the vertical temperature bias. The surface bias was reduced to less than  $0.5^{\circ}\text{C}$ ,  $\sim 1^{\circ}\text{C}$  smaller than that in the forward model. In the subsurface, the large negative bias was reduced to within  $1^{\circ}\text{C}$  and the bias stayed close to  $-0.5^{\circ}\text{C}$  at 200m.

The salinity bias from the forward model is positive at the surface and becomes negative below 100m, indicating the model overestimates the surface salinity and underestimates the salinity at depth. The maximum positive bias is  $\sim 0.25$  psu at surface and more than 0.5 psu around 200m. After data assimilation, salinity bias was also reduced. The positive surface bias was reduced to  $\sim 0.1$  psu and the negative subsurface bias was reduced within 0.4 psu. Considering the less abundant salinity data, particularly in the deep water column, the overall reduction of salinity bias is encouraging.

Time series of bias provides evolution of spatially overall temperature (salinity) bias. For temperature bias in the forward model, the initial value of  $-2^{\circ}\text{C}$  indicates the forward model undershoots, from a spatially average sense, temperature. The temperature bias then increases and becomes positive (**Figure 9**). The bias keeps increasing and reaches a maximum value of  $2^{\circ}\text{C}$  at the end of the study period. The drifting of temperature fields away from in-situ observations was effectively controlled after data assimilation. The DA prior was able to well constraint the temperature bias. Even more, the DA posterior constrains temperature bias around zero between  $-0.5^{\circ}\text{C}$  and  $0.5^{\circ}\text{C}$ , showing evident improvement over the forward model. Similarly for salinity, forward model error bias fluctuates up and down between  $-0.2$  psu and  $0.3$  psu, not showing stable predictability of

the forward model. With data assimilation, the salinity bias stays closely to zero in the entire assimilation period.

Overall, the evaluation of data assimilation performance regarding both surface fields and subsurface hydrography shows that the DA system can significantly reduce the discrepancy between model and observation. Although most assimilated data are satellite observed surface fields, we do see the improvement of subsurface hydrographic structure.

### **4.3. Independent data comparison**

In section 4.1 and 4.2, the performance of DA system is well evaluated at all assimilated observational time and locations and the results are promising. Since 4DVAR data-assimilative MABGOM shows improved skill in observational space, one would wonder about its skill in the entire model space. Here we will further examine the model skill by comparing model fields to independent observations.

The independent data used are temperature and salinity profiles provided by National Oceanic and Atmospheric Administration (NOAA) Northeast Fisheries Science Center (NEFSC) ECOMON program. ECOMON focuses on ecosystem monitoring and involves shelf-wide plankton surveys which are conducted 6-7 times per year over the continental shelf from Cape Hatteras, North Carolina to Cape Sable, Nova Scotia, using NOAA research ships or charter vessels. Three surveys are performed jointly with the bottom trawl surveys in the winter, spring and autumn. Additional four cruises, conducted in winter, late spring, late summer and late autumn, are dedicated to plankton and hydrographic data collection. The data we used in this study are CTD observations from Apr 3<sup>rd</sup> to May 25<sup>th</sup>, 2006. Most of the casts are located near the Great South Channel, to the west of Georges Bank (**Figure 1**). In totally 275 temperature and salinity profiles are available for comparison. For better visualization purpose, observational profiles are interpolated to the model vertical S-coordinate (**Figure 10**).

Profiles are sorted in time ascending order thus profile 1 was taken on Apr 3<sup>rd</sup>, and profile 275 was taken on May 25<sup>th</sup>, 2006. The maximum depth ranges from 50m to 200m. Seasonal variation is apparent from the observed temperature profiles e.g., the water

column was nearly well mixed in the first few profiles and the surface warmed up 10°C in May. The forward model tends to overshoot surface temperature and undershoot temperature at bottom, thus strengthens the thermocline. This is consistent with previous analysis in section 4.2.2. After data assimilation, the seasonal evolution was well resolved and both location/timing and magnitude compare favorable to in-situ observations. The total RMSE of temperature between forward and observation is 1.52°C. In comparison, total RMSE of temperature between DA posterior and observation was reduced to 0.59°C, by 62%.

Salinity profiles in early April 2006 also shows nearly well mixed conditions. As with seasonal evolution, surface salinity becomes fresher, which is probably related to increased costal freshwater discharge. The forward model was able to capture those processes but the magnitude was not accurate. With data assimilation, model control variables were adjusted and salinity profiles compare very well to the observations. In this case, adjusted circulation brought more fresh water to the Great South Channel and the adjusted surface fresh water flux contributes to the improvement of surface salinity. The total salinity RMSE was reduced from 0.30 psu to 0.13 psu, a reduction of 57%.

Furthermore, plots of temperature and salinity provide an overall comparison of observation and data-assimilative model (**Figure 11**). Compared to MABGOM forward model, both temperature and salinity form DA posterior oriented along diagonal, suggesting better fittings. For temperature (salinity), the slope and intercept based on linear fitting between observation and forward model are 1.53 (0.67) and -2.77 (11.09) respectively and for DA posterior, they are 1.0 (0.94) and -0.18 (1.87), respectively. Overall, forward model overshoot temperature and undershot salinity in the Georges Bank and Great South Chanel region while DA posterior showed better model skill.

The comparison with independent data indicates the data-assimilative MABGOM model not only significantly improves model skill in observational space, but also shows decent extrapolation capability. This provides us with confidence to use the data-assimilative model for further dynamical analysis.

#### 4.4. Evolution of the Warm Core Ring in 2006

During spring-summer transition period of 2006, a big Warm Core Ring pinched off from a Gulf Stream meander and impinged upon the continental shelfbreak in the Mid-Atlantic Bight. The role of the WCR in changing the coastal environment could be dramatic. We show the development of the WCR using data-assimilative MABGOM model. Detailed analyses of the ring evolution are included in the second part of this study.

The evolution of the WCR can be captured by SSH and SST fields. Shown in **Figure 12** and **Figure 13** are bi-weekly evolutions of SSH and SST fields related to the WCR. On April 1st, 2006, a large meander of Gulf Stream has already formed, with a larger sea surface height of  $\sim 0.5\text{m}$  and high surface temperature close to  $24^\circ\text{C}$  centered at  $74.5\text{W}$  and  $35.5\text{N}$ . This feature is also resolved in the model results. However, without data assimilation, the MABGOM forward model could not correctly resolve the proper size and magnitude of the meander. In comparison, the MABGOM posterior better captures the meander and closely matches the observation.

Two weeks later, on April 15<sup>th</sup>, the Gulf Stream meander extended further into the slope region and the meander was about to transit into a warm core ring. The sea surface height anomaly strengthened with a maximum value larger than  $0.6\text{m}$ . The extension is even more apparent from the SST field and the northern wall of the meander was about to make contact with the shelfbreak. The forward model undershoots the eddy intensity and the size and shape of the eddy was distorted without constraint. The DA posterior captured the eddy well in terms of both surface height and surface temperature.

By the end of April, the meander had already developed into a warm core ring which was located in the slope sea between Gulf Stream and continental shelf. The ring was interacting with shelfbreak where one parcel of warm water from the front of the ring was advected further downstream, to the southwest. Without realtime observation constraint, the forward model failed in resolving the eddy and Gulf Stream pattern and deviated from satellite observation. The DA posterior well reconstructed the eddy field and streamers (*Garfield and Evans, 1987*) can be clearly seen at the northern periphery of the eddy and are more apparent than in the observed SST data, which have lower resolution.

In mid-May, a detached eddy sat between shelfbreak and the Gulf Stream. This is the end period of interaction with the shelfbreak and the eddy was retreating back to the deep ocean. The size of the eddy decreased and surface height and surface temperature close to the center of the eddy also decreased. By this time, due to the interaction of eddy and shelfbreak jet and also recirculation of slope water near Cape Hatters (*Lozier and Gawarkiewicz, 2001*), the entire slope sea was covered by warm surface water up to 20°C.

In the end of May, the eddy retreat further and started re-attaching to the Gulf Stream. At the same time, another meander located to the east of the eddy was also making contact with the eddy. The eddy will probably be entrained to the meander trough in the following stage but this is beyond the scope of this study. Again, the DA posterior captured the pattern of both surface height and surface temperature.

As we can see, in order to hindcast the eddy process discussed here, the forward model only will encounter difficulty in resolving the ocean states. On the other hand, data-assimilative model is able to provide decent comparison to the observations. Meanwhile, much higher temporal and spatial resolution of the model can potentially offer much more insights into the dynamical processes.

## **5. Discussions and Summary**

Using the latest developed ROMS-4DVAR technique (*Moore et al., 2011a, 2011b, 2011c*), we constructed a shelf-wide data assimilative model encompassing the Northeast U.S. based on the forward model (MABGOM) described by *He and Chen* (in revision). Our MABGOM 4DVAR model assimilates satellite observed surface height and surface temperature, in-situ temperature profiles including CTD, XBT and ARGO, as well as glider cross-sections. The focus of this study is the Gulf Stream Warm Core Ring during spring-summer transition in 2006. Via data assimilation, the model skill was significantly improved in terms of realistically reproducing the circulation in the Mid-Atlantic Bight, especially WCR related features.

The performance of data assimilation depends closely on the parameterization of the background error covariance matrix **B**. As a part of **B**, Standard deviation errors of state

variables are usually estimated based on intrinsic variability of the forward model (Powell et al., 2008; Broquet et al., 2009; Moore et al., 2011b). Thus the performance of the forward model would also be critical because whether or not the standard deviation derived from the model forward represents realistic variability will directly impact the cost function and increments distribution. The use of clamped open boundary conditions together with the sponge layer implementation increased the uncertainties of forward model. Meanwhile, strong climatological tracer nudging is not recommended as this will introduce potential bias from the T/S climatology. On the other hand, climatological nudging is necessary in order to keep the strong western boundary current in its proper position. Thus one trade-off solution is applying nudging only in the sponge layers. By doing so, the general pattern of Gulf Stream and its meander/WCR was sensibly resolved. Also in building **B**, the choice of 50km horizontal de-correlation scale is based on the normal size of WCR and 30m vertical scale would guarantee surface-impact of satellite data and proper impact of subsurface data.

Properly defining observational error matrix **R** is another factor that controls minimization of the cost function. If large observational errors are assigned, a relatively loose constraint will be applied, which further limits the fitting to observations. On the other hand, tiny observational errors will exert stronger constraint of the model and yield closer fitting. However, large increments will be generated to correct the model, which could over-perturb the ocean state and potentially impair model performance.

The quality of assimilated data is also vital. In our case, coastal SSH data shoreward 200m isobath were excluded since the common OI error of altimeter product is large. Sensitivity twin experiments have been performed and the run without coastal SSH data outperformed the case that assimilates all available SSH data. For a region such as Mid-Atlantic Bight, co-existence of Gulf Stream and coastal flow originated from Labrador Sea (*Lorder et al.*, 1998) makes it dynamically complicated. Gridded altimeter data could get the large scale western boundary current correct but might not be able to precisely resolve nearshore processes that are dramatically different. Theoretically, along-track altimeter data would be more accurate. However, the spatial sparsity and noise of along track data do not favor the purpose of our study.

Despite all these difficulties and uncertainties, this paper presents a successful application of ROMS-IS4DVAR to the Northeast US coastal ocean. Actually this is the first shelf wide data-assimilative model in this region that allows adjustments of initial, boundary and surface forcing conditions.

The model skill was significantly refined via data assimilation. SSH over the entire assimilation period was improved by 79%. The previous RMSE with forward model was 0.28m and decreased to 0.06m (the value of SSH observational error) after data assimilation. SST was improved by 65%, with RMSE reduced from 1.90°C to 0.68°C. The DA posterior can resolve the Gulf Stream meander and WCR more accurately in both location and intensity. Subsurface fields which are of great importance for the purpose of our study have also been improved.

The comparison of independent ECOMON data that were not assimilated into the model demonstrates good extrapolation skill of the model. The overall temperature RMSE between forward model and ECOMON observation was 1.52°C and then was reduced to 0.59°C after data assimilation, a 62% reduction. The salinity RMSE was reduced from 0.3psu to 0.13psu, by 57%. Based on the information from observations, model dynamics were able to adjust the remote portion of circulation.

Realistic data assimilative modeling could potentially provide many insights into coastal circulation dynamics and prospects for its use are bright. Using state-of-art ROMS-IS4DVAR algorithms, the application in this study is successful and the evolution of a WCR was well depicted. Detailed analysis of the influence of the WCR on the coastal circulation will be discussed in the second part of this study.

## Reference

- Aikman, F., H.W. Ou, and R.W. Houghton, Current variability across the New England continental shelf-break and slope, *Continental Shelf Research*, 8, 625-651, 1988.
- Broquet, G., C.A. Edwards, A.M. Moore, B.S. Powell, M. Veneziani, and J.D. Doyle, Application of 4D-Variational data assimilation to the California Current System, *Dynamics of Atmospheres and Oceans*, 48, 69-92, 2009.
- Castelao, R.M., S. Glen, R. Chant, and J. Kohut, Seasonal evolution of hydrographic fields in the central Middle Atlantic Bight from glider observations, *Geophysical Research Letters*, 35, doi:10.1029/2007GL032335, 2008.
- Chapman, D.C., Numerical treatment of cross-shelf open boundaries in a barotropic coastal ocean model, *Journal of Physical Oceanography*, 15 (8), 1060-1075, 1985.
- Churchill, J.H., P.C. Cornillon, and G.W. Milkowski, A Cyclonic Eddy and Shelf-Slope Water Exchange Associated With a Gulf Stream Warm-Core Ring, *Journal of Physical Oceanography*, 91 (C8), 9615-9623, 1986.
- Derber, J., and A. Rosati, A global oceanic data assimilation system, *Journal of Physical Oceanography*, 19, 1333-1347, 1989.
- Fairall, C.W., E.F. Bradley, J.E. Hare, A.A. Garchev, and J. Edson, Bulk parameterization of air-sea fluxes: Updates and verification for the COARE algorithm, *Journal of Climate*, 16, 571-591, 2003.
- Fisher, M., Minimization algorithms for variational data assimilation, in *Proceedings of the ECMWF Seminar on Recent Development in Numerical Methods for Atmospheric Modelling*, pp. 364-385, Reading, England, 1998.
- Flather, R.A., A tidal model of the northwest European continental shelf, *Mem. Soc. R. Sci. Liege*, 6 (10), 141-164, 1976.
- Haidvogel, D.B., H. Arango, W. P. Budgell, B. D. Cornuelle, E. Curchitser, E. Di Lorenzo, K. Fennel, W. R. Geyer, A. J. Hermann, L. Lanerolle, J. Levin, J. C. McWilliams, A. J. Miller, A. M. Moore, T. M. Powell, A. F. Shchepetkin, C. R. Sherwood, R. P. Signell, J. C. Warner, and J. Wilkin, Ocean forecasting in terrain-following coordinates: Formulation and skill assessment of the Regional Ocean Modeling System., *Journal of Computational Physics*, 227, 3595-3624, 2008.
- Haidvogel, D.B., H. Arango, W.P. Budgell, B.D. Cornuelle, E. Curchitser, E.D. Lorenzo, K. Fennel, W.R. Geyer, A.J. Hermann, L. Lanerolle, J. Levin, J.C. McWilliams, A.J. Miller, A.M. Moore, T.M. Powell, A.F. Shchepetkin, C.R. Sherwood, R.P. Signell, J.C. Warner, and J. Wilkin, Ocean forecasting in terrain-following coordinates: Formulation and skill assessment of the Regional Ocean Modeling System, *Journal of Computational Physics*, 227, 3595-3624, 2008.
- Ingleby, B., and M. Huddleston, Quality control of coean temperature and salinity profiles - historical and real-time data, *Journrnal of Marine Systems*, 65, 158-175, 2007.

Joyce, T.M., J.K.B. Bishop, and O.B. Brown, Observation of offshore shelf-water transport induced by a warm-core ring, *Deep-Sea Research*, 39, S97-S113, 1992.

Lentz, S.J., Observations and a Model of the Mean Circulation over the Middle Atlantic Bight Continental Shelf, *Journal of Physical Oceanography*, 38, 1203-1221, 2008.

Loder, J.W., B. Petrie, and G. Gawarkiewicz, The coastal ocean off northeastern North America: A large-scale view, in *The Sea*, pp. 105-133, Wiley, New York, 1998.

Lorenzo, E.D., A. Moore, H. Arango, Chua, B.D. Cornuelle, A.J. Miller, B. Powell, and A. Bennett, Weak and strong constraint data assimilation in the inverse Regional Ocean Modeling System (ROMS): development and application for a baroclinic coastal upwelling system, *Ocean Modeling*, 16 (3-4), 160-187, 2007.

Lozier, M.S., and G.G. Gawarkiewicz, Cross-frontal exchange in the Middle Atlantic Bight as evidenced by surface drifters, *Journal of Physical Oceanography*, 31, 2498-2510, 2001.

Mellor, G.L., and T. Yamada, Development of a Turbulence Closure Model for Geophysical Fluid Problems, *Reviews of Geophysics and Space Physics*, 20 (4), 851-875, 1982.

Moore, A.M., H.G. Arango, E.D. Lorenzo, B.D. Cornuelle, A.J. Miller, and D.J. Neilson, A Comprehensive ocean prediction and analysis system based on the tangent linear and adjoint of a regional ocean model, *Ocean Modeling*, 7, 227-258, 2004.

Moore, A.M., H.G. Arango, G. Broquet, C. Edwards, M. Veneziani, B. Powell, D. Foley, J.D. Doyle, D. Costa, and P. Robinson, The Regional Ocean Modeling System (ROMS) 4-Dimensional Variational Data Assimilation Systems: part2 - Performance and Application to the California Current System, 2011.

Moore, A.M., H.G. Arango, G. Broquet, B. Powell, A.T. Weaver, and J. Zavala-Garay, The Regional Ocean Modeling System (ROMS) 4-Dimensional Variational Data Assimilation Systems: part1 - System overview and formulation, 2011.

Morgan, C.W., and J.M. Bishop, An example of Gulf Stream Eddy-Induced Water Exchange in the Mid-Atlantic Bight, *Journal of Physical Oceanography*, 7, 472-479, 1977.

Powell, B.S., H. Arango, A.M. Moore, E.D. Lorenzo, and D.F. R.F. Milliff, 4DVAR Data Assimilation in the Intra-Americas Sea with the Regional Ocean Modeling System (ROMS), *Ocean Modeling*, 25, 173-188, 2008.

Shchepetkin, A.F., and J.C. McWilliams, The regional oceanic modeling system (ROMS): a split-explicit, free surface, topography-following-coordinate oceanic model, *Ocean Modeling*, 9, 347-404, 2005.

Taylor, K.E., Summarizing multiple aspects of model performance in a single diagram, *Journal of Geophysical Research - Atmosphere*, 106, 7183-7192, 2001.

Weaver, A.T., and P. Courtier, Correlation modelling on the sphere using a generalized diffusion equation, *Quarterly Journal of the Royal Meteorological Society*, 127, 1815-1846, 2001.

Weaver, A.T., J. Vialard, and D.L.T. Anderson, Three- and four-dimensional variational data assimilation with a general circulation model of the tropical Pacific Ocean. Part I: Formulation, internal diagnostics, and consistency checks, *Monthly Weather Review*, 131, 1360-1378, 2003.

Wilkin, J., J. Zavala-Garay, J. Levin, and W.G. Zhang, Four-Dimensional Variational Assimilation of Satellite Temperature and Sea Level Data in the Coastal Ocean and Adjacent Deep Sea, in *Geoscience and Remote Sensing Symposium, 2008. IGARSS 2008. IEEE International*, pp. III - 427-III - 430, 2008.

Zhai, X., R.J. Greatbatch, and J. Sheng, Diagnosing the role of eddies in driving the circulation of the northwest Atlantic Ocean, *Geophysical Research Letters*, 31, doi:10.1029/2004GL021146, 2004.

## Figures

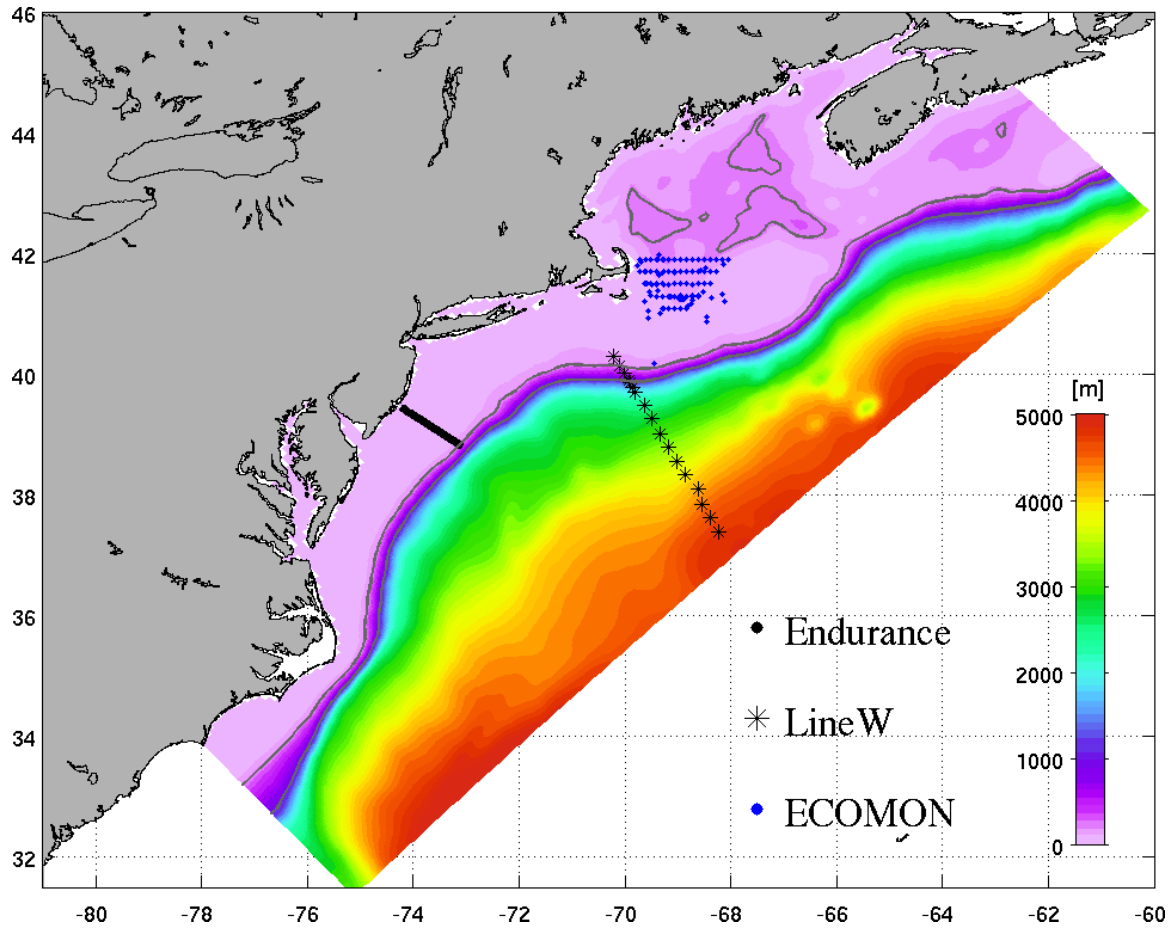


Figure 1. Mid Atlantic Bight and Gulf of Maine model domain. The bathymetry of this region is shown in color. The Endurance line along which gliders are flied is denoted in thick black line. Line-W Oceanus CTD stations are shown in black stars. ECOMON CTD stations in May 2006 are shown in black dots.

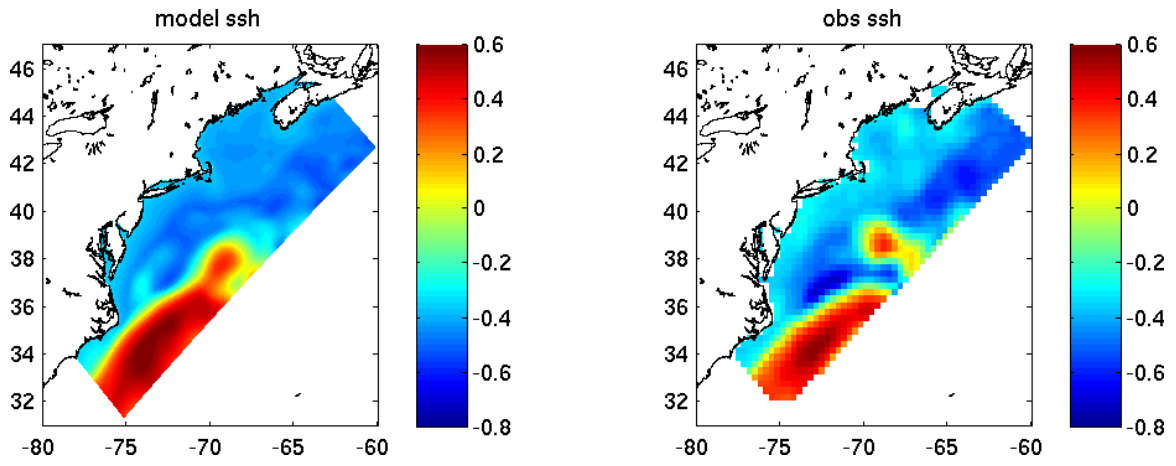


Figure2. Comparison of mean sea surface height from the forward model (MABGOM) and AVISO observations.

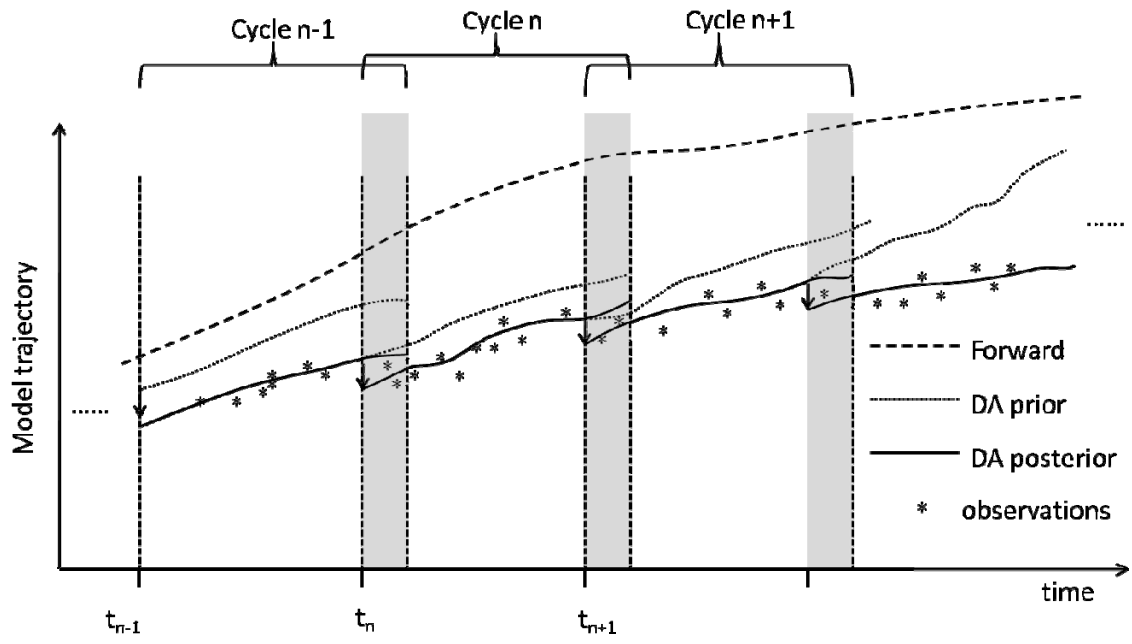


Figure 3. A schematic showing the assimilation cycles. Shaded columns represent overlaps between cycles.

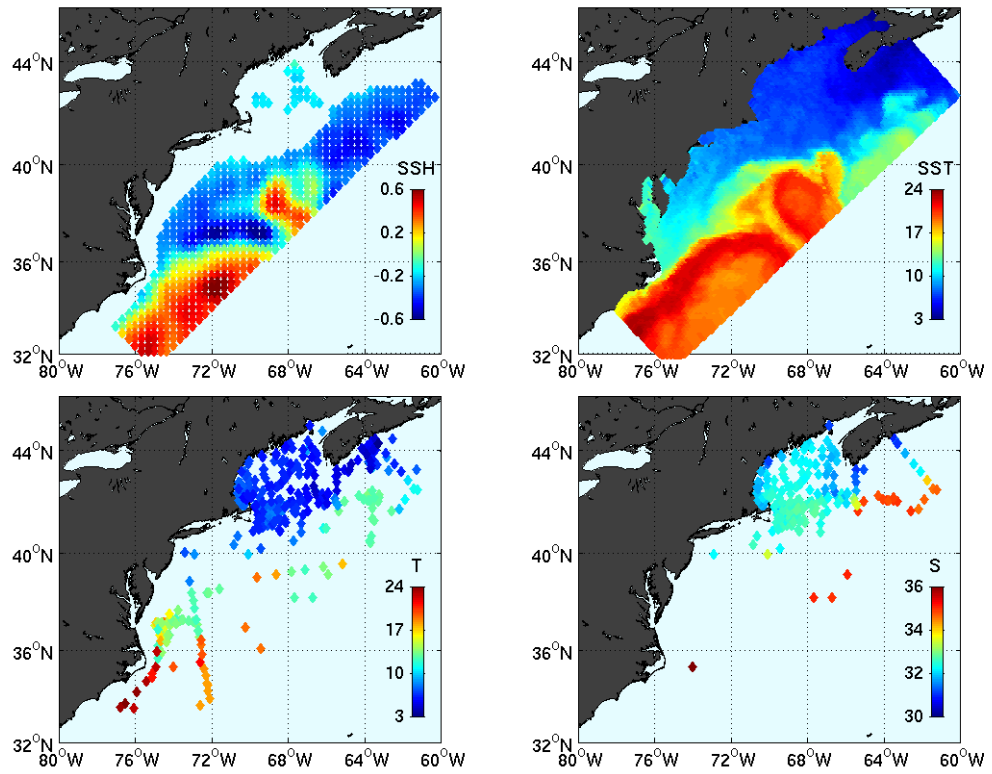


Figure4. Super observations of sea surface height (SSH, upper left), sea surface temperature (SST, upper right), in-situ temperature profiles (lower left), in-situ salinity profiles (lower right). Only SST and SSH on April 1st, 2006 are shown while all profiles collected during the assimilation period (Apr1st, 2006 to May 31<sup>st</sup>, 2006) are shown.

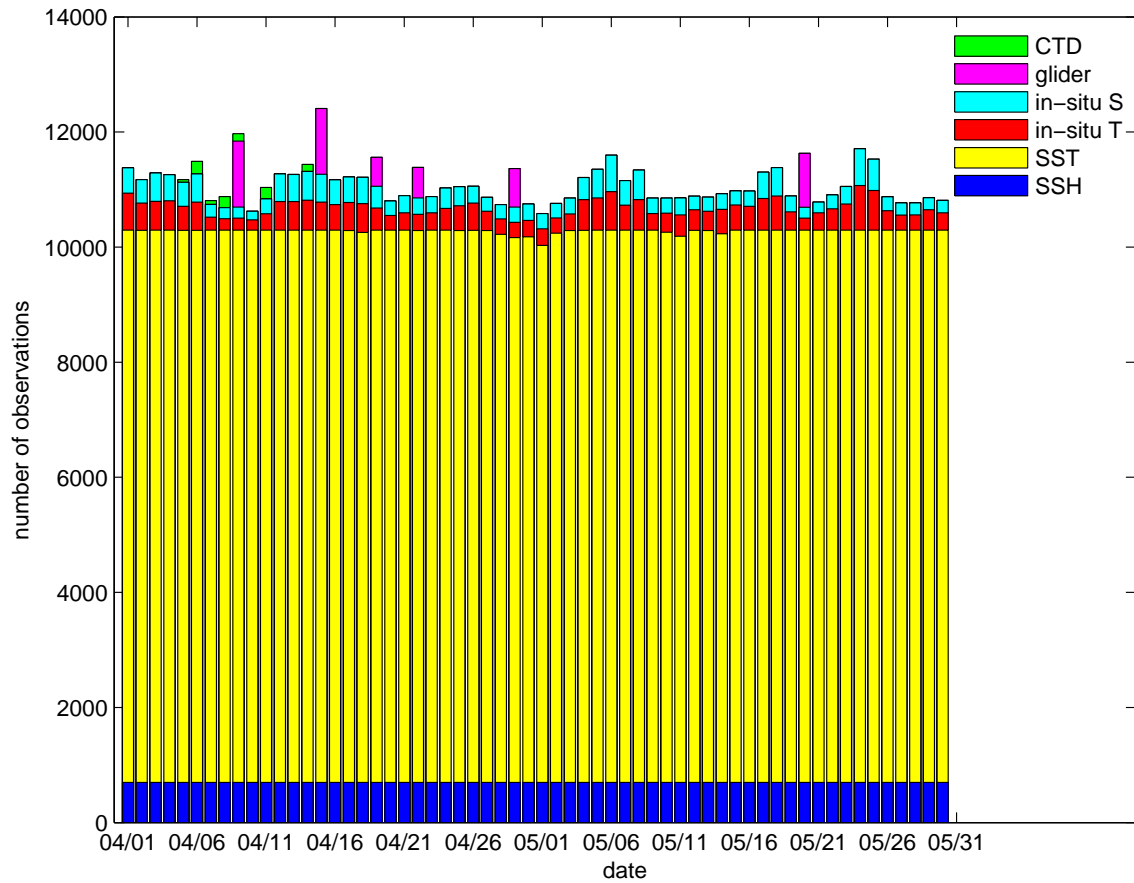


Figure 5. temporal distributions of super observations. SSH, SST, in-situ temperature profiles, in-situ salinity profiles, Endurance line glider T/S observations, and Line-W Oceanus CTD T/S observations are shown in blue, yellow, red, and cyan, magenta and green, respectively.

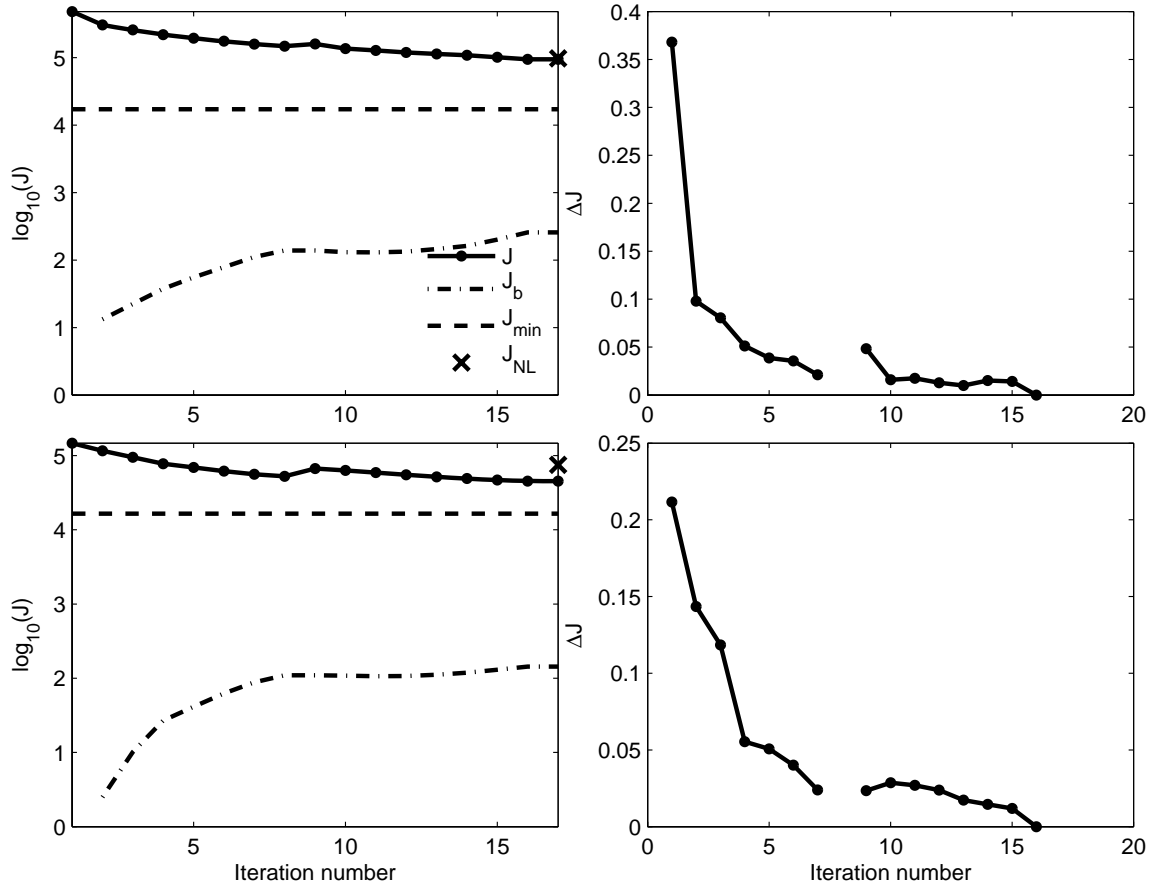


Figure 6. Cost function in the first and last window. Shown on the left column are evolutions of cost functions versus the number of inner loops during the first and last assimilation windows while on the right are changes of total cost function with respect to the inner loops. Total cost function are shown in solid while background cost functions are shown in dash-dot. The theoretical minimum value of total cost functions are shown in dashed lines. Crosses represent the value of nonlinear cost function.

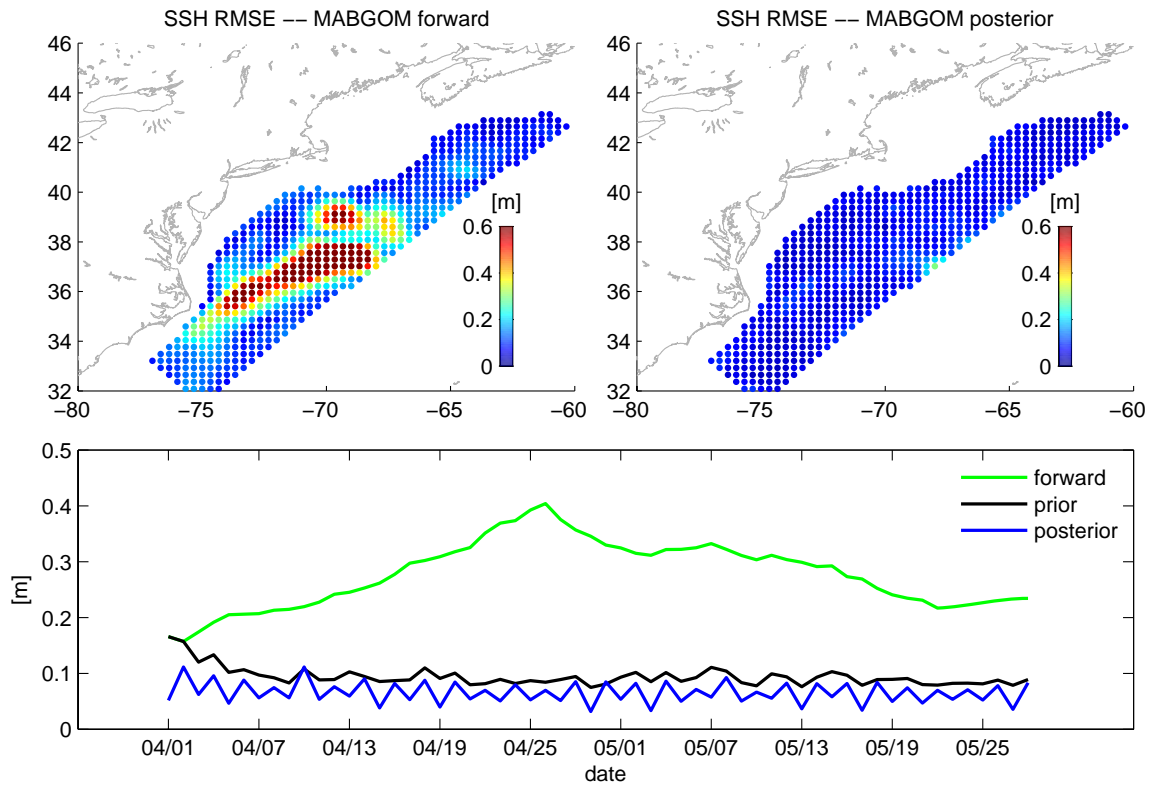


Figure 7. Root Mean Square error of assimilated sea surface height. Spatial distribution of RMSE between forward model and observations is shown on the upper left. RMSE between model posterior and observations is shown on the upper right. Time series of spatial averaged RMSE of assimilated SSH are also shown in the bottom panel.

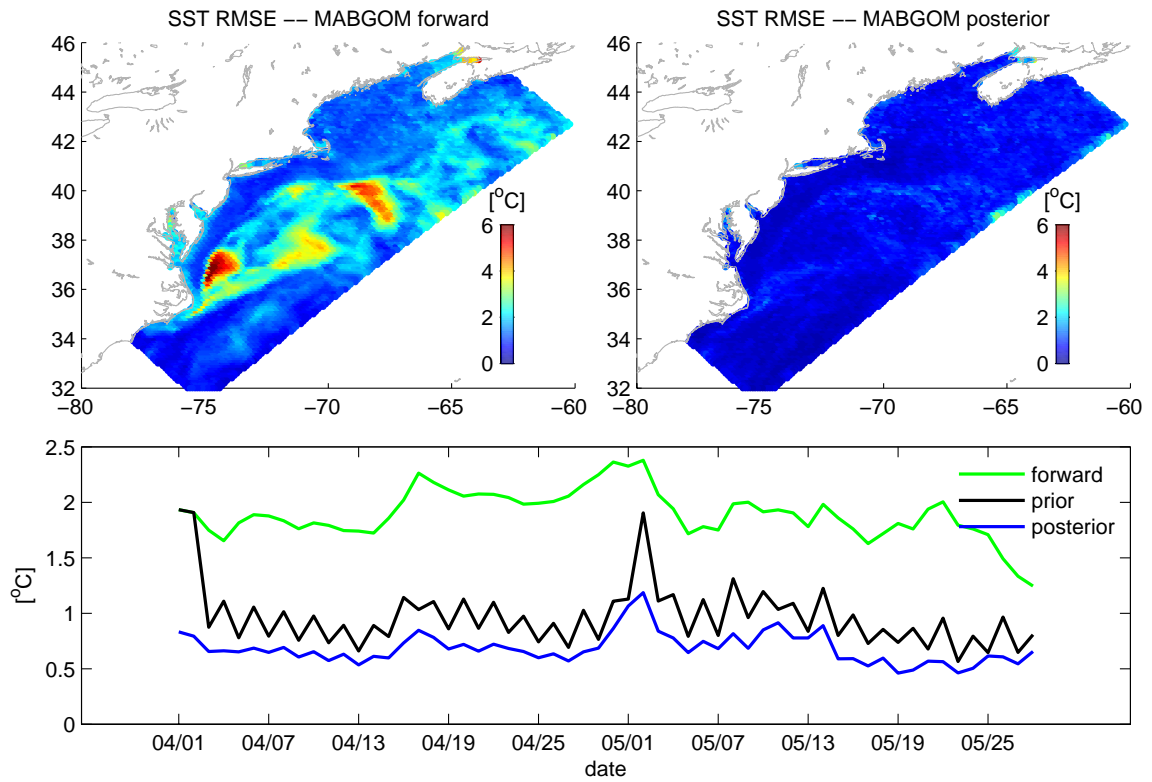


Figure 8. Root Mean Square error of assimilated sea surface temperature. Spatial distribution of RMSE between forward model and observations is shown on the upper left. RMSE between model posterior and observations is shown on the upper right. Time series of spatial averaged RMSE of assimilated SST are also shown in the bottom panel.

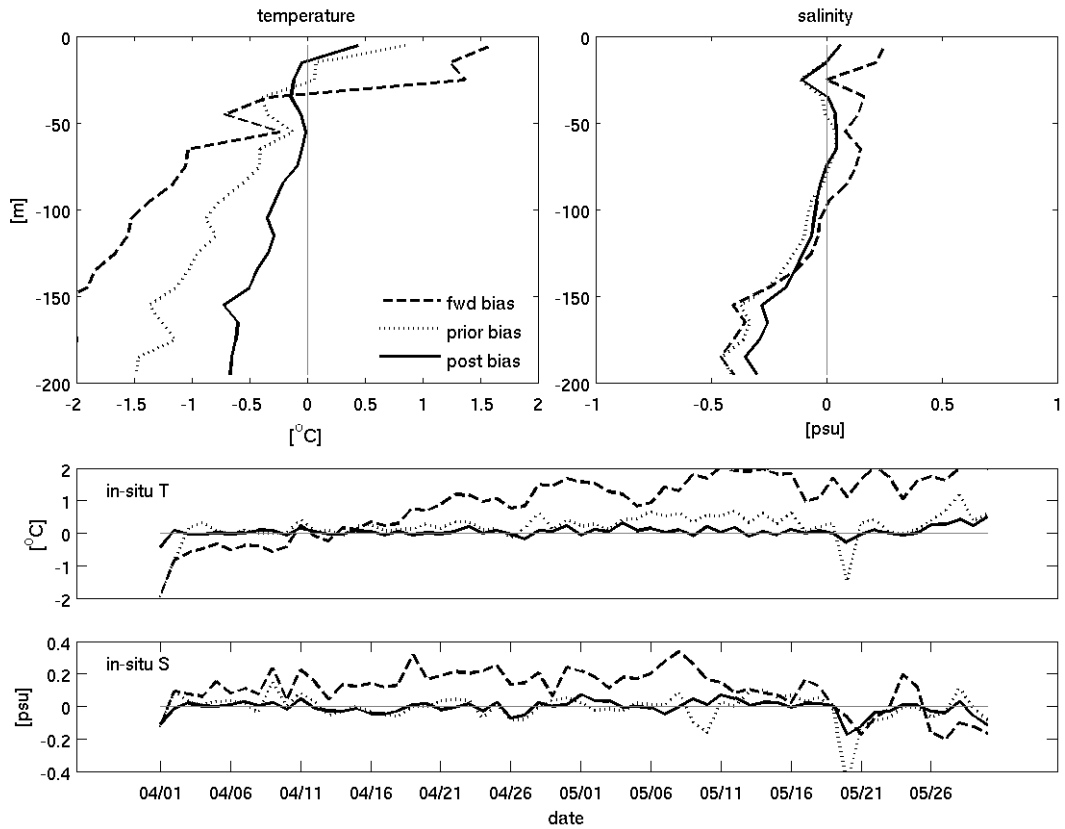


Figure 9. Bias of assimilated in-situ temperature and salinity on the continental shelf. Vertical distribution of biases of temperature and salinity over the assimilation period are shown in the top two panels, with biases from the forward model, 4DVAR prior and posterior denoted in dashed, dotted and solid lines. Time series of assimilated temperature and salinity biases are also shown.

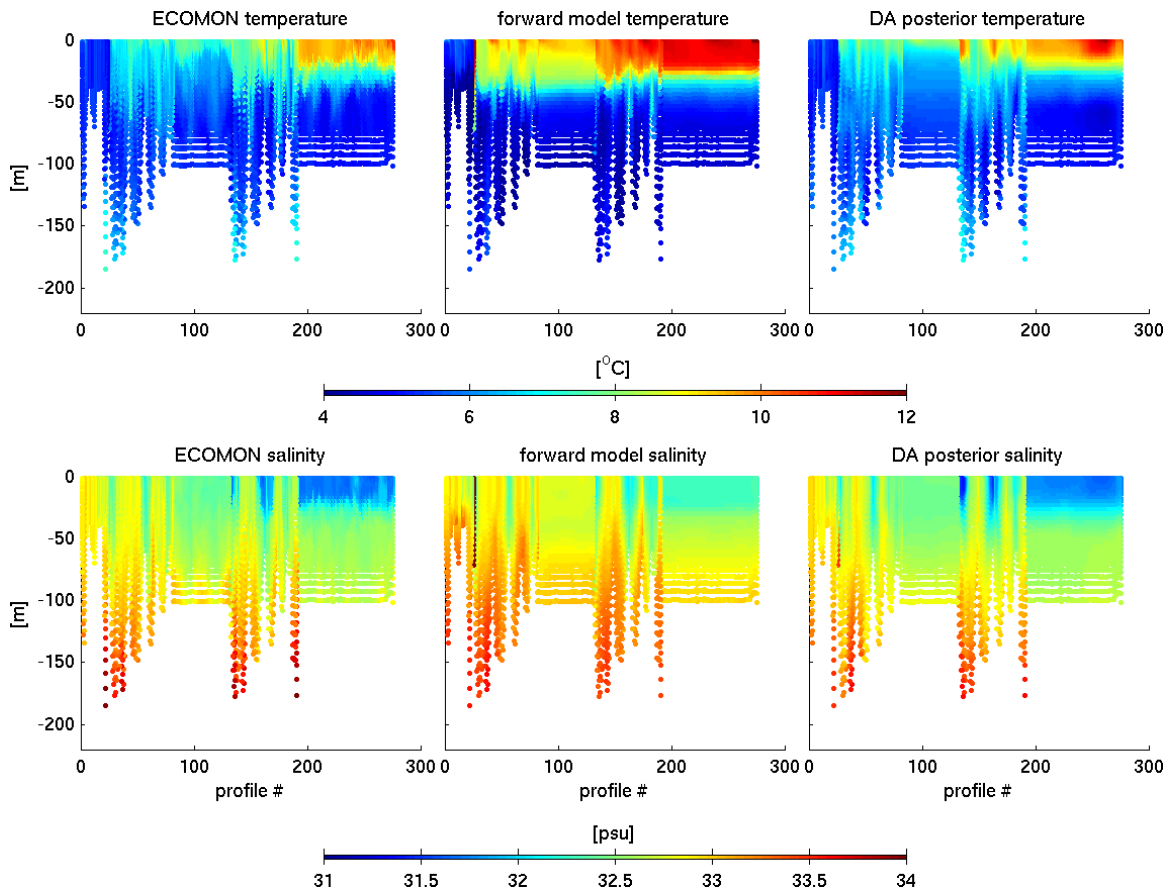


Figure 10. Comparison of temperature and salinity profiles from ECOMON in-situ observation, MABGOM forward model and 4DVAR posterior.

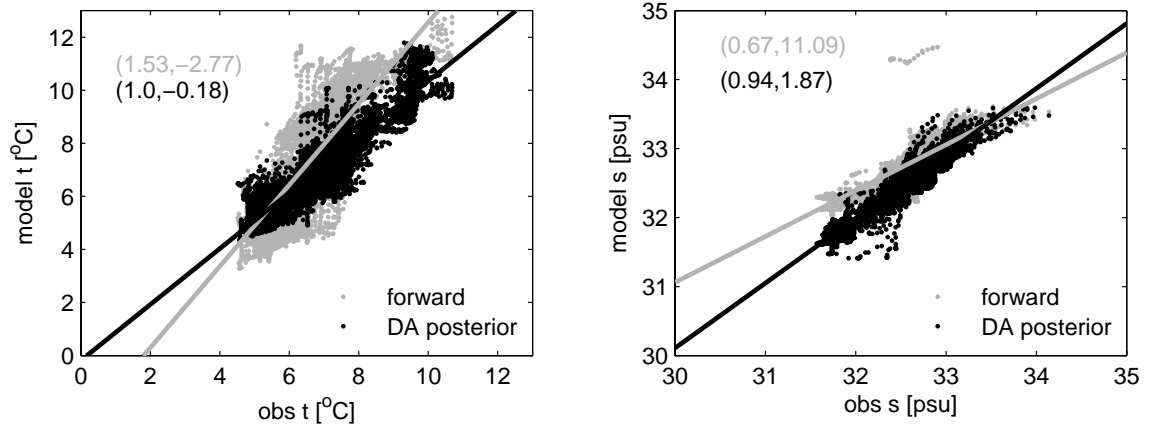


Figure 11. One to one plot of ECOMON observed versus modeled temperature (left) and salinity (right). Temperature (salinity) from the forward model is shown in gray while temperature (salinity) from DA posterior is shown in black. Slope and intercept are also shown in the parentheses, respectively.

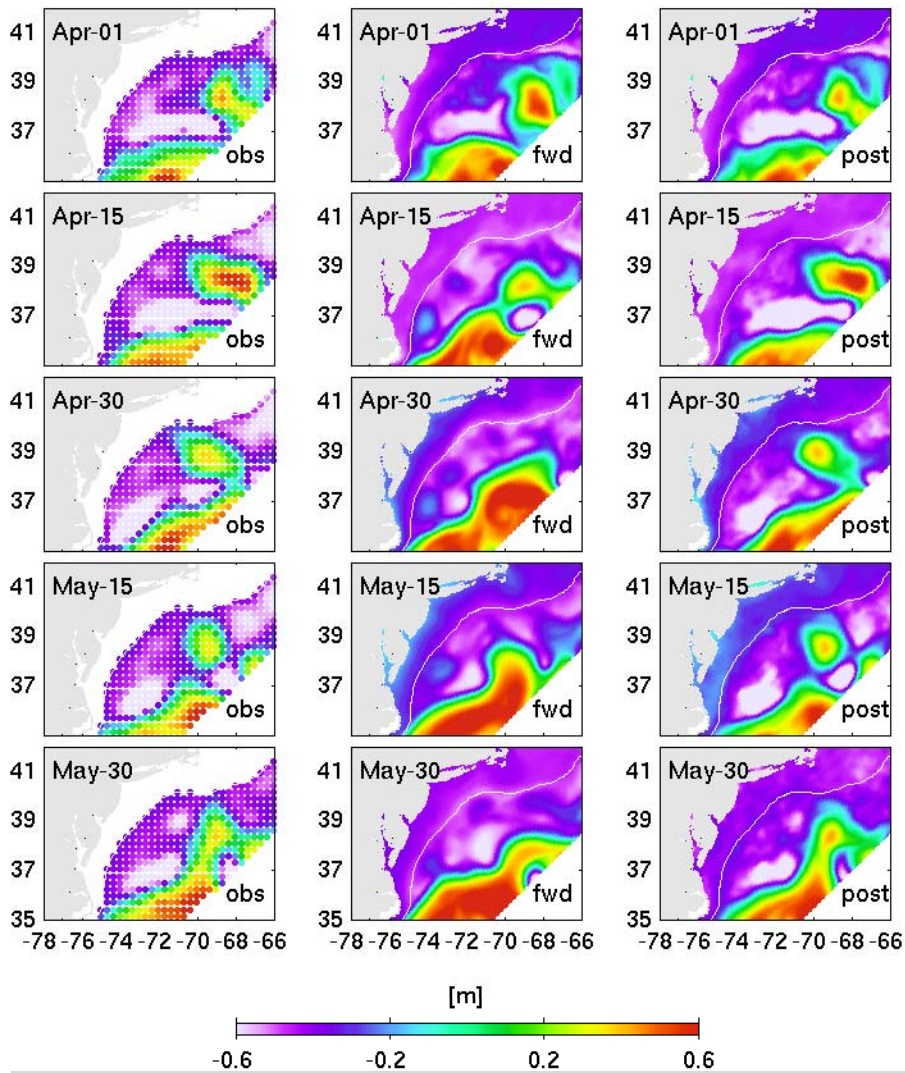


Figure12. Bi-weekly Evolution of sea surface height during the assimilation period. Showing in the first column are satellite observations while MABGOM forward model and 4DVAR posterior results are shown in the second and third column.

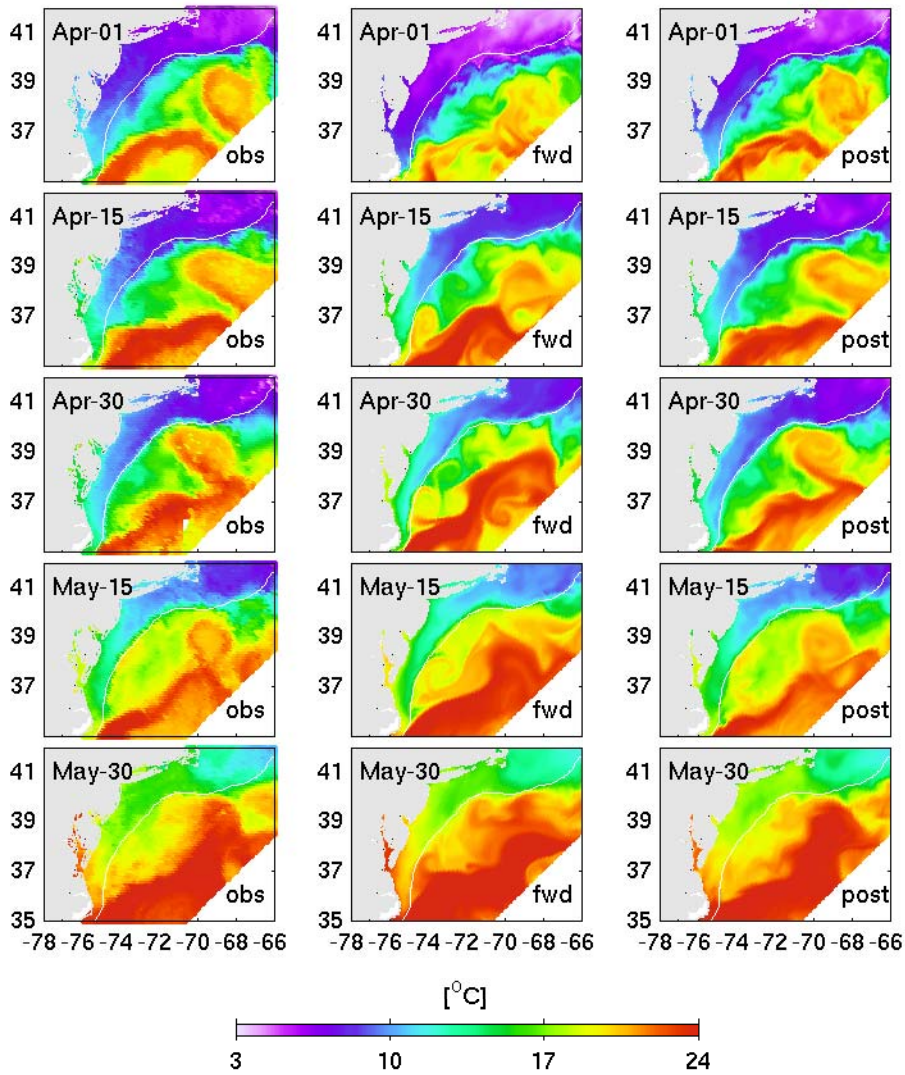


Figure13. Bi-weekly Evolution of sea surface temperature during the assimilation period. Showing in the first column are satellite observations while MABGOM forward model and 4DVAR posterior results are shown in the second and third column.

CHAPTER 5: DATA ASSIMILATIVE MODELING INVESTIGATION OF GULF  
STREAM WARM CORE RING INTERACTION WITH CONTINENTAL SHELF AND  
SLOPE, PART 2: DYNAMICS<sup>4</sup>

Ke Chen and Ruoying He

Department of Marine Earth and Atmospheric Sciences, North Carolina State University

---

<sup>4</sup> This chapter is based on a manuscript to be submitted to Journal of Geophysical Research

## Abstract

A data-assimilative ocean circulation model is used to investigate a Gulf Stream Warm Core Ring (WCR) in spring 2006. Based on the model results, 3-dimensional evolution of this great WCR is depicted in detail. The WCR, being one of the largest in recent history, significantly changed the circulation in the Middle Atlantic Bight (MAB) continental slope and shelf. The mean cross-shelf transport induced by the WCR is estimated at 0.28 Sv offshore, and balances the mean along-shelf transport by the shelfbreak jet. Instantaneous streamer transport is up to 2.1 Sv, suggesting dramatic shelf/slope exchange. During the first week of May 2006, when the WCR was impinging upon the shelfbreak, large heat/salt flux with peak value of  $-8900 \text{ Watt m}^{-2} / -4 \times 10^{-4} \text{ Kg m}^{-2} \text{ s}^{-1}$  is observed, indicating significant entrainment of cold/fresh shelf water by the WCR. Vorticity analysis reveals the nonlinear advection term, as well as the residual of joint effect of baroclinicity and bottom relief (JEBAR) and advection of potential vorticity (APV) play an important role in controlling the vorticity variability on evolution.

## 1. Introduction

In coastal oceans, one fundamental question regarding the dynamics of the shelfbreak regions is the role of offshore eddies in modifying the shelfbreak frontal system and inducing exchange between shelf and slope. This question has been studied in a variety of geographical regions and dynamic contexts (e.g., *Tintore et al.*, 1990; *Oey*, 1995; *Frolov et al.*, 2004; *Mizobata et al.*, 2006). Particularly, in the Mid-Atlantic Bight, the Gulf Stream warm-core rings have long been recognized as an important process in the exchange of shelf and slope water masses.

In the Mid-Atlantic Bight, pioneer studies on the warm core ring (WCR, thereafter) and related cross shelf exchange have been done based on field work combined with available satellite observations (e.g., *Morgan and Bishop*, 1977; *Churchill et al.*, 1986; *Houghton et al.*, 1986; *Garfield and Evans*, 1987; *Joyce et al.*, 1992). Those studies have offered important insight into WCRs and also have provided estimates of cross-shelf transport and flux based on available data. Lately, *Pickart et al.*(1999) using hydrography, acoustic Doppler current profiler (ADCP) observations and satellite imagery, showed the

pattern of a shelfbreak meander associated with a Gulf Stream WCR. *Gawarkiewicz et al.* (2001) studied the influence of a slope eddy on the shelfbreak frontal jet based on in-situ observations, and provided a generalized schematic of eddy-jet interaction.

Besides observational studies, theoretical work has also addressed this topic in various aspects. *Chapman and Brink* (1987) used a linear model to treat the case of an offshore eddy impinging upon a stratified shelf and slope. *Wang* (1992) studied a nonlinear case using a three dimensional model that showed the evolution of cyclonic eddies and shelf/slope response. *Frolov et al.* (2004) studied the interaction of a Loop Current Eddy with a western boundary of Gulf of Mexico using a two-layer model. *Wei et al.* (2009) used Princeton Ocean Model (POM) to stimulate the interaction of warm core ring with continental shelf and slope in the Mid-Atlantic Bight by using near realistic topography.

While WCRs have long been studied observationally, detailed characterization is still limited by the availability and spatial coverage of observations. Theoretical models provided important guidance to dynamics but they may not accurately represent the ocean processes. Furthermore, considering the presence of the shelfbreak front and jet (*Gawarkiewicz et al.*, 1996, 2001; *Linder and Gawarkiewicz*, 1998; *Fratantoni et al.*, 2001; *Chen and He*, 2010), the role of warm core rings on the outer shelf is even more complicated. More detailed study of warm core rings and their interaction with continental shelfbreak calls for time- and space continuous realizations of ocean state variables. In this study, we will approach this topic using a realistic, data-assimilative model. We will focus on a warm core ring during the spring-summer transition period in 2006 as a case study. The data assimilative model will be reviewed in section 2. Evolution of the warm core ring will be depicted in section 3. In section 4, we will investigate the interaction of the ring and the shelfbreak frontal system. The shelf slope exchange process will be studied in section 5, followed by discussion and summary in section 6.

## **2. Data Assimilative Model**

Regional Ocean Modeling System (ROMS) is a free-surface, hydrostatic, primitive equation model discretized with a terrain following vertical coordinate system

(*Shchepetkin and McWilliams, 2005; Haidvogel et al., 2008*). ROMS is characterized by advanced numerical techniques that are designed to minimize computational errors (*Shchepetkin and McWilliams, 2003*), and it has been widely used in many regions in the world oceans. Recently, the latest developed ROMS 4D Variational data assimilation functionality became available (*Di Lorenzo et al., 2007; Powell et al., 2008; Moore et al., 2011a*), and promoted pioneer studies in Intra-Americas Sea (*Powell et al., 2009*) and the California Current System (*Broquet et al., 2009, 2011*).

The model used in this study is based on a regional shelf-wide ocean circulation model encompassing the Northeast U.S. coastal region (MABGOM, *He and Chen*). Using recently developed ROMS-IS4DVAR functionality, we constructed data-assimilative MABGOM based on the forward model (*Chen et al., 2011a*). The model has horizontal resolution of 6km (10km) in the cross- (along-) shelf direction and has 36 vertical terrain-following layers. We applied the method of *Mellor and Yamada (1982)* to compute vertical turbulent mixing, as well as the quadratic drag formulation for the bottom friction specification. HYCOM (Hybrid Coordinate Ocean Model) NCODA (Naval Research Laboratory Coupled Ocean Data Assimilation) product with  $1/12^\circ$  resolution and 32 vertical z-level. For barotropic boundary conditions, the Flather (1976) condition completed with an Orlanski radiation condition (*Chapman, 1985*) is used while for baroclinic mode, clamped boundary conditions are used along with sponge layers near 3 open boundaries. Surface forcing data are provided by National Center for Environment Prediction (NCEP) North America Regional Reanalysis (NARR) archive. Surface net heat flux is further corrected based on NOAA blended SST with a relaxation timescale of 0.5 day (*He and Chen, in revision; Chen and He, 2010*). Real-time river runoff data from United State Geological Survey (USGS) are used to specify freshwater input of 9 major rivers along northeast US coast.

The data-assimilative MABGOM model assimilates sea surface height (SSH), sea surface temperature, in-situ temperature and salinity profiles, Endurance line glider temperature and salinity, and Line-W CTD profiles. The model initializes on April 1<sup>st</sup>, 2006 and ends on May 30<sup>th</sup> 2006, covering the entire life span of a Gulf Stream Warm Core Ring.

The MABGOM 4DVAR system has been documented in detail in the first part of this study. Evaluation of the data assimilation skill shows that using 4DVAR data assimilation, the hindcasting skill of MABGOM model was significantly improved. Comparison against independent Ecosystem Monitoring (ECOMON, collected by the National Marine Fisheries Service) hydrographic data indicates our model has decent extrapolation capability in terms of capturing hydrographic features where in-situ data are not assimilated. Overall, the well-performed data assimilative MABGOM model has paved the road for further scientific understandings.

### **3. The Evolution of the Warm Core Ring**

The Warm core ring in this study is one of the largest in recent history. Satellite imagery shows this large WCR is the result of Gulf Stream meander closeup. Large impacts on the shelf and slope circulation are expected in the presence of such a big ring. In this section, detailed evolution of Gulf Stream meander and the WCR will be depicted based on the results of our data assimilative MABGOM model.

On April 2<sup>nd</sup> 2006, a large Gulf Stream meander had already formed and the crest of the meander extended far northward into the slope region (**Figure 2**). Circular stream function contours indicate the meander was about to close at its base and pinch off. The meander was featured by high sea surface height center which was about 0.6m higher than its surroundings. The warm and saline meander water had already altered the hydrographic conditions of the slope sea. Meanwhile, negative vorticity was identified near the central part of the meander. At this time, the surface outcrop of shelfbreak front in the MAB (*Linder and Gawarkiewicz, 1998; Bisagni et al., 2009*) stayed parallel to the local isobaths close to the shelfbreak, suggesting direct impact of meander had not reached the shelf region.

The meander kept evolving with deepening of the meander trough and further extension of meander crest and the meander finally pinched off in late April. On April 22<sup>th</sup>, the meander already became a large detached WCR (**Figure 3**). The center of the WCR was located at 69° W, 38.8° N while the outer edge of the WCR covers from

71° W 67.5° W and 37.8° N to 39.8° N. The radius of the WCR is estimated based on the de-correlation distance of stream function. As highlighted by the thin white curve, the mean radius of the WCR at its initial stage is 96km while the largest radius is up to 120km. The temperature and salinity near the WCR center is about 20° C and 36 and the depth (e-folding) of the WCR is up to 1000m (**Figure 4**). With surface azimuthal velocity up to 1.7 m/s, the WCR extended completely across the continental slope region and was about to make contact with the shelfbreak. Warm/saline WCR water was advecting toward shore on the western periphery while one more impressive feature we noticed was the entrainment of cold/fresh shelf water indicated by the “streamer” (*Garfield and Evans, 1987*) on the eastern periphery of the WCR. Comparing to the meander stage, the sea surface height and negative vorticity near the center portion is larger, indicating stronger anti-cyclonic rotation.

The detached WCR moved toward the northwest and impacted the shelfbreak on May 2<sup>nd</sup> (**Figure 5**). The center of the WCR moved to 69.5° W and 38.9° N, closer to the shelfbreak and the furthest north edge of the WCR reached ~80m isobath. The size of the WCR decreased compared to its initial stage. The mean radius decreased to 65km and the longer axis was 87km. While the WCR was smaller, its impact on the shelfbreak can be clearly noticed. At the eastern side of the WCR, the leading edge of warm/saline WCR water made direct contact with the continental shelfbreak and the outcrop of 34.5 isohaline was displaced onshore. These parcels of WCR water were heading to the southwest along local bathymetry, having been entrained into the shelfbreak jet. At the trailing edge of the WCR, the streamer became even larger pulling significant amount of shelf water offshore. The entrained cold/fresh shelf water moved anti-cyclonically along the eastern periphery of the WCR and reached the Gulf Stream northern wall. The interaction between the WCR and shelfbreak excited frontal waves (*Ramp et al., 1983*) propagating westward. Frontal instability due to strong horizontal shear is believed to be the primary contributor which derived the flow across the front.

On May 9<sup>th</sup>, the WCR had already retreated slightly from the shelfbreak (**Figure 6**). The center of the WCR was at 69.3° W, 38.8° N, to the southeast of its location on May 2<sup>nd</sup>. Having no direct contact with shelfbreak and the Gulf Stream, the WCR is more

circular, with mean radius of 63km. The warm/saline water parcel detached from the WCR extended along the shelfbreak from New England to Delaware, significantly changing the shelf and shelfbreak hydrographic conditions. Further subsurface investigation (not shown) found this warm/saline water mass was about 50m deep and its most onshore limb was found near 80m isobath. With mean temperature/salinity of 20° C and 34.2, it was heading southwest at 0.6m/s. The frontal wave along the shelfbreak to the western side of the WCR was clearer. The wavelength was estimated about 120km, a number much larger than the estimation of Ramp et al (1983). We also note that the WCR in Ramp et al (1983) is smaller than the WCR in this study. At this time, the streamer was even more significant. The entrained shelfwater can be clearly seen around the western side of the WCR, covering almost half portion of the periphery. The relative vorticity filed in the central WCR was more uniform, with a value around 0.5, suggesting a more solid body rotation.

At depth, while the impact of WCR can still reach ca. 1000m, the intensity of the WCR has already decreased. The 16° C isotherm retreated to ca. 200m, compared to ca. 500m on April 22<sup>nd</sup>. The water mass with maximum salinity around 35.5 located at subsurface below 100m while the surface water was about 0.5 fresher. This feature is consistent with *Joyce* (1984) and *Joyce et al.* (1992) and is related to the entrainment of fresh shelf water in the upper water column. The maximum azimuthal velocity decreased to 1.3m/s, which also suggests the spin-down of the WCR.

The WCR kept retreating southward back to the Gulf Stream region and continued to be trimmed back in size during mid-May. By the end of May, both the intensity and size of the WCR had greatly decreased and the center of the WCR was more offshore (**Figure 8**). Actually the WCR had already made contact with the Gulf Stream and another meander which extends at the east boundary of the model domain. The interaction with Gulf and meander further reduced the size and changed the shape of the WCR, which finally were assimilated by the Gulf Stream (not shown). The warm/saline water mass along the shelfbreak had already reached Cape Hatteras and became entrained to the Gulf Stream (*Ford et al.*, 1952; *Fisher*, 1972; *Gawarkiewicz and Linder*, 2006). In the presence

of the slope gyre (Csanady and Hamilton, 1988), those water mass would be re-circulated in the slope sea.

The life span of the WCR is identified from April 22<sup>nd</sup>, to May 18<sup>th</sup>, 2006. Due to its progression across the slope in late April and its interaction with the shelfbreak in early May, significant impact on the slope and shelf hydrography and circulation are expected. The southwestward traveling along the shelfbreak of detached warm/saline WCR water and its entrainment near Cape Hatteras would have increased the near surface temperature and salinity in the slope region. The onshore advection of WCR water at its leading edge and offshore advection of shelfbreak water at its trailing edge had induced notable exchange between continental shelf and slope. The presence of the WCR acted as an obstruction for the northern portion of the shelfbreak jet and the large streamer greatly displaced the shelfbreak front offshore and advected shelf water to the slope. In the following section, we will focus on the shelf/slope exchange induced by the WCR.

#### **4. Shelf/slope exchange**

To begin with our analysis, we first need to define one boundary in order to calculate the exchange induced by the WCR. Considering the vertical extension of the WCR and also the constraint of the Taylor-Proudman theorem (*He and Weisberg, 2003*), we selected the 1000m isobath for volume transport calculation. The 1000m isobath from Cape Hatteras to Cape Cod defines a ~900km boundary offshore MAB (**Figure 1**). Using the same method in *Chen and He (2010)*, spatial distribution of the cross-shore transport is computed (**Figure 9**). While the Gulf Stream meander may also induce cross-shore exchange, in this study, only the WCR stage from April 22<sup>nd</sup> to May 18<sup>th</sup> is considered. The cross-shore volume transport in the southern MAB is still characterized by small mean values and large standard deviation. Given that the location of the WCR in northern MAB, this suggests that in the absence of WCR, cross-shore transport is small and highly variable. However, approaching the northern MAB, direct impact by the WCR is expected. From offshore New Jersey to Nantucket Shoals, as shown in Figure 8 from ~450km to 700km, the mean cross-shore transport is onshore, with the largest onshore transport of 0.5 Sv. Considering the location and the orientation of local bathymetry, the

onshore transports correlated well with the leading edge of the WCR. What is more interesting is the offshore transport up to 1Sv from ~700km to 800km, which lies at the trailing edge of the WCR. The region of offshore transport is narrower than the region of onshore transport yet the magnitude is larger. Further examination of the normal velocity across the 1000m isobath (not shown) reveals the offshore velocity is indeed larger than the onshore velocity. Recalling the trajectories of the WCR (**Figure 2 – Figure 8**) and the local bathymetry at New England shelfbreak, the trailing edge of the WCR is closer to the isobaths. Thus stronger offshore movement of the water column is induced due to the presence of the WCR.

Given the presence of the streamer, shelf water is largely pulled offshore. It is important to evaluate the role of WCR in terms of shelf water mass budget. Focusing on the region directly impacted by the WCR, we picked 450km-800km portion of 1000m isoabth to calculate total cross-shelf transport in the upper 200m over the WCR period. From April 22<sup>nd</sup> to May 18<sup>th</sup>, the total cross-shelf transport is estimated to be 0.28 Sv. This is much larger than the mean value estimated by *Chen and He* (2010), in which the cross-shelf transport is estimated as 0.035 Sv, based on 4-year hindcast results. Comparing with the mean shelfbreak jet transport of 0.3 Sv (*Linder and Gawarkiewicz*, 1998; *Chen and He*, 2011), due to the impinging of WCR on the shelfbreak, almost the entire shelfbreak jet was diverted offshore.

On the synoptic scale, the instantaneous transport of the streamer is also estimated. On May 2<sup>nd</sup>, while the WCR was interacting with the shelfbreak, a large streamer formed on the eastern periphery. Within a region that salinity is less than 34.5, we define one segment of the 1000m isobath as the base of the streamer, which has a width of 110km. Across the vertical section, the cross-shelf transport of fresh water of the streamer is calculated only where salinity is less than 34.5 and the instantaneous value is estimated at 2.1 Sv. Compared to the value (0.25 Sv) of Garfield and Evans (1987), which was based on limited in-situ stations, our result is one order of magnitude larger.

Based on the large entrainment of shelf water in the streamer, the temperature and salinity budget on the MAB continental shelf would certainly be largely influenced.

Using the same method in *Chen and He* (2010), the cross-shelf eddy heat and salt fluxes are calculated as integration of flux function  $\Phi$  (*Garvine et al.*, 1988), such that

$$F(z) = \frac{1}{\Delta z \Delta x} \int_{z-\frac{\Delta z}{2}}^{z+\frac{\Delta z}{2}} \int_{x_1}^{x_2} \Phi(x, z_1) dx dz \quad (1)$$

For the heat flux,  $\Phi$  is defined,

$$\Phi = \rho C_p (T - T_m)(v - v_m) \quad (2)$$

For the salt flux,  $\Phi$  is defined:

$$\Phi = \frac{\rho}{1000} (S - S_m)(v - v_m) \quad (3)$$

where  $S$ ,  $T$ ,  $v$  are the salinity, temperature and cross-shelf velocity, respectively.  $\rho$  is water density and  $C_p$ , the seawater specific heat. The variables with subscript  $m$  indicate the respective mean values along 1000m isobath. As defined, the cross-shelf fluxes are proportional to the eddy derivation of quantities and normal velocity from their mean states. Given the definition of normal velocity is seaward, the negative heat means onshore heat (salt) flux which can be induced by offshore transport of cold (fresh) shelf water.

Focusing on the WCR impinging region, from 450km to 800km along 1000m isobaths, we calculated the temporal cross shelf heat and salt fluxes during the WCR period (**Figure 10**). Before the impinging of the WCR, the cross-shelf heat (salt) flux is relatively small and the direction is fluctuating. Starting in May, when WCR was impacting the shelfbreak, large entrainment of shelf water occurred as indicated by the negative value of heat and salt fluxes. The cross-shelf heat (salt) flux peaks on May 3<sup>rd</sup>, up to  $\sim 8900 \text{ Watt m}^{-2}$  ( $\sim 4 \times 10^{-4} \text{ Kg m}^{-2} \text{ s}^{-1}$ ) and remains negative through the first week of May 2006. In the retreating stage of the WCR, while the heat (salt) flux is still largely onshore, the values are much smaller. The onshore heat (flux) is around  $1000 \text{ Watt m}^{-2}$  ( $5 \times 10^{-5} \text{ Kg m}^{-2} \text{ s}^{-1}$ ), which is comparable to the mean cross-shelf flux of 1000 ( $6.7 \times 10^{-5}$

$\text{Kg m}^{-2} \text{s}^{-1}$ ) in *Chen and He* (2010). Within one week timescale, the cross-shelf eddy heat (salt) flux can be increased by a factor of 8-9, which again suggests the large impact of WCR on the shelf and slope hydrographic conditions.

## 5. Vorticity Analysis

The depth averaged vorticity equation can be written as follows (see Appendix for details)

$$\frac{\partial}{\partial t} \text{curl}_z \left( \frac{M}{H} \right) + M \cdot \nabla \left( \frac{f}{H} \right) = \left( \frac{\partial(P_y/H)}{\partial x} - \frac{\partial(P_x/H)}{\partial y} \right) + \text{curl}_z \left( \frac{\tau_s - \tau_b}{\rho_o H} \right) + \text{curl}_z \left( \frac{D}{H} \right) - \text{curl}_z \left( \frac{A}{H} \right) \quad (4)$$

Where in the left hand side, the first term is the time rate change of depth averaged relative vorticity (rate); the second term is the nonlinear advection effect (ADV) and the third term is the advection of potential vorticity (APV) (*Guo et al.*, 2003). On the right hand side, the first term is Joint Effect of Baroclinicity and Bottom Relief (JEBAR) (*Mertz and Wright*, 1992; *Cane et al.*, 1998; *Guo et al.*, 2003; *Sarkisyan*, 2006); the second and third terms are effects of stress and dissipation, respectively. During the interaction with shelfbreak and spin-down of the WCR, it is interesting to diagnose relative contributions to the vorticity change. In order to do that, we focus the impinging period in the first week of May 2006 (**Figure 11**). On May 1<sup>st</sup>, the center of the WCR, as depicted by the contours of sea surface height and negative vorticity, is close to the shelfbreak. In comparison, on May 7<sup>th</sup>, the center of the WCR already retreated offshore, which is also shown by the negative rate of change slightly offshore of the shelfbreak (**Figure 11(c)**). In this period, the impinging WCR induced significant cross-shelf exchange, which can be well demonstrated by the APV term. By definition, the positive APV represents onshore transport of low PV water while negative APV stands for offshore transport of high PV water. The positive APV near the leading edge (western portion) of the WCR is consistent with the onshore movement of WCR water and the large negative APV on the trailing edge of the WCR clearly corresponds with the offshore movement. In all terms that controls the variability of depth averaged relative vorticity, apparently the APV and JEBAR are the two largest terms and they largely balance each other, as shown by the smaller residual. While considering the contribution to the

evolution of relative vorticity, the nonlinear advection term clearly plays an important role (**Figure 11(g) vs (c)**). This makes sense in that the movement of WCR largely depends on the ambient circulation condition. The residual of APV and JEBAR also contributes to the rate term, and combined with ADV, these three terms dominate the change of relative vorticity of the WCR.

## 6. Discussions and summary

The impinging of WCR on the continental shelfbreak has a dramatic impact on the shelf circulation and the interaction of WCR with the shelfbreak front/jet is important as the latter largely controls the coastal physical and biogeochemical environment. Considering the vast differences at the leading flank and the trailing flank of the WCR, two cross-isobath transects at each flank are chosen to investigate the role of WCR on the shelfbreak frontal system. As shown in **Figure 8**, one transect is located at the west of New England shelf and the leading flank of the WCR while the other one is located at the trailing flank of the WCR. Mean temperature, salinity and along-shelf velocity over the WCR during the period from April 22<sup>nd</sup> to May 18<sup>th</sup> along both transects are shown (**Figure 11**). Along the west transect, the intrusion of WCR can be clearly seen. Warm/saline WCR water dramatically altered the typical hydrographic features at this time of year (*Linder and Gawarkiewicz, 1998; Chen and He, 2010*). The thermocline was bent downward to the slope region and isohaline surfaces were more tilted offshore of the shelfbreak. The impinging anti-cyclonic WCR lead to a pole-ward movement of slope water and meanwhile, the shelfbreak jet was pushed further onshore. In comparison, on the trailing edge of the WCR, due to the strong streamer entrainment of shelf water, the hydrographic isosurfaces were flat and leaned seaward. The most striking feature we observed is the strong equatorward along shelf current, which was at least 40km wide and extended from the surface to nearly 200m deep. We found that the presence of the WCR induced significant amount of shelf water travelling downstream and greatly enhanced the along-shelf flow. Our results are consistent with *Gawarkiewicz et al. (2001)* in that the shelfbreak front are more steep at the leading flank of the WCR while is different in terms of the weakened shelfbreak jet. Actually, the results are dependent on the location of the

transects. Sampling further downstream (offshore New Jersey, not shown), we observed an enhanced shelfbreak jet. Onshore movement of slope water there increased the gradient of shelfbreak front (*Gawarkiewicz et al.* 2001) which accounts for the stronger jet.

The whole picture of the impact of the WCR on the shelfbreak frontal system can be completed in **Figure 13**. Before the impingement of the WCR, we can clearly see, especially from the subsurface map, the shelfbreak jet, which is a continuous flow from north to the south. During the impingement of the WCR, the shelfbreak circulation was dramatically altered. On the leading edge, due to the intrusion of the WCR, the shelfbreak front was pushed onshore and the shelfbreak became weaker. On the trailing edge of the WCR, due to the entrainment of shelfwater, the shelfbreak jet was bent offshore. Previous continuous along shelf flow was largely shut down.

Entrainment of shelf water is reported in many earlier studies (e.g., *Morgan and Bishop*, 1977; *Garfield and Evans*, 1987) and the footprint of entrained fresh water is not well understood due to the limitations of available observations. Previous observations revealed the fresh water could accumulate around the periphery just outside of the edge of maximum velocity (*Joyce*, 1984). In our study, the entrained fresh water could cover half portion of the WCR and reach Gulf Stream northern wall. We also noted that after the detaching of WCR from Gulf Stream, due to the cutoff supply of saline Gulf Stream water and swirl of fresh shelf water, the salinity near the center of the WCR was greatly decreased (**Figure 4**). This is even clear during the retreating stage after impacting the shelfbreak (**Figure 5**). The decrease of central salinity decreased the cross-shelf or slope gradient and played an important role in the spin-down of the WCR. Not until the re-attachment with Gulf Stream did the salinity in the WCR center increase (**Figure 6**).

Based on the state-of-art 4D variational data assimilation technique, a data assimilative model is constructed and used to study a Gulf Stream WCR in 2006. The WCR in this study is the largest one in recent history and is expected to have significant impact on MAB coastal environment. Having a life span of approximately 26 days, the WCR in this study detached from closed Gulf Stream meander on April 22<sup>nd</sup>, 2006 and re-attach Gulf on May 18<sup>th</sup>, 2006. The initial radius and depth of the WCR are estimated

as 96km and 1000m. The WCR headed to the continental shelf and made contact in early May. The impinging of WCR upon the shelfbreak lasted about one week and induced dramatic exchange between the shelf and slope. Mean cross-shelf transport is estimated to be 0.28 Sv during the impinging period while the instantaneous streamer transport is as large as 2.1 Sv. The maximum heat/salt flux is  $-8900 \text{ Watt m}^{-2} / -4 \times 10^{-4} \text{ Kg m}^{-2} \text{ s}^{-1}$ , on May 3<sup>rd</sup>, 2006, indicating strong entrainment of cold/fresh shelf water offshore. During the evolution and spin-down of the WCR, the radius and intensity were reduced. The advection of potential vorticity and joint effect of baroclinicity and bottom relief are the two largest terms while the variation of relative vorticity of the WCR is largely controlled by the nonlinear advection effect. The entrainment of fresh shelf water into the center of the WCR also accounts for its spin-down. After interacting with the shelfbreak, the WCR retreated back to the slope region. After making contact with Gulf Stream and another meander, the decaying WCR was assimilated into its main body.

In this study, we demonstrated the capability of the latest 4DVAR technique and its feasibility in strongly dynamical regions, such as the MAB. Focusing on the Gulf Stream WCR, the constructed data assimilative model promotes the understanding of the WCR and related processes and paved the road for further scientific understandings.

## Appendix A: Depth Averaged Momentum and Vorticity Equation

Vertically integrating the horizontal momentum equation:

$$\int_{-h}^{\zeta} \frac{\partial u}{\partial t} dz + \int_{-h}^{\zeta} u \frac{\partial u}{\partial x} dz + \int_{-h}^{\zeta} v \frac{\partial u}{\partial y} dz + \int_{-h}^{\zeta} w \frac{\partial u}{\partial z} dz - \int_{-h}^{\zeta} f v dz = \int_{-h}^{\zeta} \left(-\frac{1}{\rho_0} \frac{\partial p}{\partial x}\right) dz + \int_{-h}^{\zeta} \frac{\partial}{\partial z} \left(K_m \frac{\partial u}{\partial z}\right) dz + \int_{-h}^{\zeta} D_u dz$$

$$\int_{-h}^{\zeta} \frac{\partial v}{\partial t} dz + \int_{-h}^{\zeta} u \frac{\partial v}{\partial x} dz + \int_{-h}^{\zeta} v \frac{\partial v}{\partial y} dz + \int_{-h}^{\zeta} w \frac{\partial v}{\partial z} dz + \int_{-h}^{\zeta} f u dz = \int_{-h}^{\zeta} \left(-\frac{1}{\rho_0} \frac{\partial p}{\partial y}\right) dz + \int_{-h}^{\zeta} \frac{\partial}{\partial z} \left(K_m \frac{\partial v}{\partial z}\right) dz + \int_{-h}^{\zeta} D_v dz$$

Using the boundary condition we get vertical integrated equations:

$$\int_{-h}^{\zeta} \frac{\partial u}{\partial t} dz + \int_{-h}^{\zeta} u \frac{\partial u}{\partial x} dz + \int_{-h}^{\zeta} v \frac{\partial u}{\partial y} dz + \int_{-h}^{\zeta} w \frac{\partial u}{\partial z} dz - \int_{-h}^{\zeta} f v dz = \int_{-h}^{\zeta} \left(-\frac{1}{\rho_0} \frac{\partial p}{\partial x}\right) dz + \frac{\tau_s^x - \tau_b^x}{\rho_0} + \int_{-h}^{\zeta} D_u dz$$

$$\int_{-h}^{\zeta} \frac{\partial v}{\partial t} dz + \int_{-h}^{\zeta} u \frac{\partial v}{\partial x} dz + \int_{-h}^{\zeta} v \frac{\partial v}{\partial y} dz + \int_{-h}^{\zeta} w \frac{\partial v}{\partial z} dz + \int_{-h}^{\zeta} f u dz = \int_{-h}^{\zeta} \left(-\frac{1}{\rho_0} \frac{\partial p}{\partial y}\right) dz + \frac{\tau_s^y - \tau_b^y}{\rho_0} + \int_{-h}^{\zeta} D_v dz$$

If we define the depth averaged velocity as

$$\bar{u} = \frac{1}{h + \zeta} \int_{-h(x,y)}^{\zeta(x,y,t)} u dz, \quad \bar{v} = \frac{1}{h + \zeta} \int_{-h(x,y)}^{\zeta(x,y,t)} v dz,$$

vertical integrated nonlinear advection terms as

$$A_x = \int_{-h(x,y)}^{\zeta(x,y,t)} \left(u \frac{\partial u}{\partial x} + v \frac{\partial u}{\partial y} + w \frac{\partial u}{\partial z}\right) dz, \quad A_y = \int_{-h(x,y)}^{\zeta(x,y,t)} \left(u \frac{\partial v}{\partial x} + v \frac{\partial v}{\partial y} + w \frac{\partial v}{\partial z}\right) dz;$$

vertical integrated pressure gradient terms as

$$P_x = \int_{-h(x,y)}^{\zeta(x,y,t)} \left(-\frac{1}{\rho_0} \frac{\partial p}{\partial x}\right) dz, \quad P_y = \int_{-h(x,y)}^{\zeta(x,y,t)} \left(-\frac{1}{\rho_0} \frac{\partial p}{\partial y}\right) dz;$$

vertical integrated horizontal mixing terms as

$$D_x = \int_{-h(x,y)}^{\zeta(x,y,t)} D_u dz, \quad D_y = \int_{-h(x,y)}^{\zeta(x,y,t)} D_v dz,$$

and apply both the surface and bottom conditions, we can rewrite the depth averaged momentum equation as:

$$\frac{\partial \bar{u}}{\partial t} + \frac{A_x}{h + \zeta} - f \bar{v} = \frac{P_x}{h + \zeta} + \frac{\tau^{sx}}{\rho_0 (h + \zeta)} - \frac{\tau^{bx}}{\rho_0 (h + \zeta)} + \frac{D_x}{h + \zeta}$$

$$\frac{\partial \bar{v}}{\partial t} + \frac{A_y}{h + \zeta} + f \bar{u} = \frac{P_y}{h + \zeta} + \frac{\tau^{sy}}{\rho_0 (h + \zeta)} - \frac{\tau^{by}}{\rho_0 (h + \zeta)} + \frac{D_y}{h + \zeta}$$

Taking the curl of the depth averaged momentum equation:

$$\frac{\partial}{\partial t} \left( \frac{\partial \bar{v}}{\partial x} - \frac{\partial \bar{u}}{\partial y} \right) + \left( \frac{\partial A_y / (h + \zeta)}{\partial x} - \frac{\partial A_x / (h + \zeta)}{\partial y} \right) + \left( \frac{\partial f \bar{u}}{\partial x} + \frac{\partial f \bar{v}}{\partial y} \right) = \left( \frac{\partial P_y / (h + \zeta)}{\partial x} - \frac{\partial P_x / (h + \zeta)}{\partial y} \right) + \left( \frac{\partial D_y / (h + \zeta)}{\partial x} - \frac{\partial D_x / (h + \zeta)}{\partial y} \right) + \left( \frac{\partial \tau^{xy} / \rho_0 (h + \zeta)}{\partial x} - \frac{\partial \tau^{yx} / \rho_0 (h + \zeta)}{\partial y} \right) - \left( \frac{\partial \tau^{by} / \rho_0 (h + \zeta)}{\partial x} - \frac{\partial \tau^{bx} / \rho_0 (h + \zeta)}{\partial y} \right)$$

If we define:  $H = h + \zeta$ ;  $M = (\bar{u}\vec{i} + \bar{v}\vec{j}) * H$ ;  $A = A_x\vec{i} + A_y\vec{j}$ ;  $D = D_x\vec{i} + D_y\vec{j}$

The Coriolis force curl can be rewritten as

$$\frac{\partial f \bar{u}}{\partial x} + \frac{\partial f \bar{v}}{\partial y} = \frac{\partial (f/H)(\bar{u} * H)}{\partial x} + \frac{\partial (f/H)(\bar{v} * H)}{\partial y} = (\bar{u}H) * \frac{\partial (f/H)}{\partial x} + (\bar{v}H) * \frac{\partial (f/H)}{\partial y} + (f/H) \frac{\partial (\bar{u} * H)}{\partial x} + (f/H) \frac{\partial (\bar{v} * H)}{\partial y} = (\bar{u}H) * \frac{\partial (f/H)}{\partial x} + (\bar{v}H) * \frac{\partial (f/H)}{\partial y} = M \cdot \nabla \left( \frac{f}{H} \right)$$

We can then rewrite the depth-averaged vorticity equation as follows:

$$\frac{\partial}{\partial t} \text{curl}_z \left( \frac{M}{H} \right) + M \cdot \nabla \left( \frac{f}{H} \right) = \left( \frac{\partial (P_y / H)}{\partial x} - \frac{\partial (P_x / H)}{\partial y} \right) + \text{curl}_z \left( \frac{\tau_s - \tau_b}{\rho_0 H} \right) + \text{curl}_z \left( \frac{D}{H} \right) - \text{curl}_z \left( \frac{A}{H} \right)$$

## Appendix B: Derivation of JEBAR term

Joint Effect of Baroclinicity and Relief (JEBAR) (*Sakisyan, 2006*) term is firstly derived as

$$J \left( \int_{-h}^0 \frac{\rho g z}{\rho_0} dz, 1/h \right) \text{ where } J(A, B) = \frac{\partial A}{\partial x} \frac{\partial B}{\partial y} - \frac{\partial B}{\partial x} \frac{\partial A}{\partial y}$$

The pressure gradient force curl is equivalent to the JEBAR term if we assume zeta=0.

First we prove the following pressure gradient term's expression:

$$\int_{-h}^0 \frac{\partial p}{\partial x} dz = h \frac{\partial}{\partial x} [p(z=0)] + g \int_{-h}^0 \rho dz + \frac{\partial}{\partial x} \left( g \int_{-h}^0 \rho z dz \right)$$

$$\begin{aligned}
& h \frac{\partial}{\partial x} [p(z=0) + g \int_{-h}^0 \rho dz] + \frac{\partial}{\partial x} (g \int_{-h}^0 \rho z dz) - \int_{-h}^0 \frac{\partial p}{\partial x} dz \\
&= h \frac{\partial}{\partial x} p(z=0) + h \frac{\partial}{\partial x} [g \int_{-h}^0 \frac{\partial p}{\partial z} (-\frac{1}{g}) dz] + \frac{\partial}{\partial x} [g \int_{-h}^0 \frac{\partial p}{\partial z} (-\frac{1}{g}) z dz] - \int_{-h}^0 \frac{\partial p}{\partial x} dz \\
&= h \frac{\partial}{\partial x} p(z=0) - h \frac{\partial}{\partial x} (\int_{-h}^0 \frac{\partial p}{\partial z} dz) - \frac{\partial}{\partial x} (\int_{-h}^0 \frac{\partial p}{\partial z} z dz) - [\frac{\partial}{\partial x} \int_{-h}^0 p dz + \frac{\partial(-h)}{\partial x} p(z=-h)] \\
&= h \frac{\partial}{\partial x} p(z=0) - h \frac{\partial}{\partial x} (\int_{-h}^0 \frac{\partial p}{\partial z} dz) - (\frac{\partial}{\partial x} \int_{-h}^0 \frac{\partial p}{\partial z} z dz + \frac{\partial}{\partial x} \int_{-h}^0 p \frac{\partial z}{\partial z} dz) + \frac{\partial(h)}{\partial x} p(z=-h) \\
&= h \frac{\partial}{\partial x} p(z=0) - h \frac{\partial}{\partial x} (\int_{-h}^0 \frac{\partial p}{\partial z} dz) - \frac{\partial}{\partial x} (\int_{-h}^0 \frac{\partial p z}{\partial z} dz) + \frac{\partial(h)}{\partial x} p(z=-h) \\
&= h \frac{\partial}{\partial x} p(z=0) - h \frac{\partial}{\partial x} (\int_{-h}^0 \frac{\partial p}{\partial z} dz) + \frac{\partial}{\partial x} [-hp(z=-h)] + \frac{\partial(h)}{\partial x} p(z=-h) \\
&= h \frac{\partial}{\partial x} p(z=0) - h \frac{\partial}{\partial x} (\int_{-h}^0 \frac{\partial p}{\partial z} dz) - h \frac{\partial}{\partial x} [p(z=-h)] \\
&= h (\frac{\partial}{\partial x} p(z=0) - \int_{-h}^0 \frac{\partial p}{\partial z} dz - p(z=-h)) \\
&= h (\frac{\partial}{\partial x} (p(z=0) - [p(z=0) - p(z=-h)] - p(z=-h))) \\
&= 0
\end{aligned}$$

$$\text{Similarly } \int_{-h}^0 \frac{\partial p}{\partial y} dz = h \frac{\partial}{\partial y} (p(z=0) + g \int_{-h}^0 \rho dz) + \frac{\partial}{\partial y} (g \int_{-h}^0 \rho z dz)$$

Then we prove that the the curl of depth averaged pressure gradient is equivalent to JEBAR.

$$\begin{aligned}
& \frac{\partial}{\partial x} (\frac{1}{h} \int_{-h}^0 \frac{\partial p}{\partial y} dz) - \frac{\partial}{\partial y} (\frac{1}{h} \int_{-h}^0 \frac{\partial p}{\partial x} dz) \\
&= \frac{\partial}{\partial x} [\frac{\partial}{\partial y} (p(z=0) + g \int_{-h}^0 \rho dz)] + \frac{1}{h} \frac{\partial}{\partial y} (g \int_{-h}^0 \rho z dz) - \frac{\partial}{\partial y} [\frac{\partial}{\partial x} (p(z=0) + g \int_{-h}^0 \rho dz)] + \frac{1}{h} \frac{\partial}{\partial x} (g \int_{-h}^0 \rho z dz) \\
&= \frac{\partial}{\partial x} [\frac{1}{h} \frac{\partial}{\partial y} (g \int_{-h}^0 \rho z dz)] - \frac{\partial}{\partial y} [\frac{1}{h} \frac{\partial}{\partial x} (g \int_{-h}^0 \rho z dz)] \\
&= \frac{\partial}{\partial x} (\frac{1}{h}) \frac{\partial}{\partial y} (g \int_{-h}^0 \rho z dz) - \frac{\partial}{\partial y} (\frac{1}{h}) \frac{\partial}{\partial x} (g \int_{-h}^0 \rho z dz) \\
&= J(1/h, \int_{-h}^0 \rho g z dz)
\end{aligned}$$

Therefore,

$$\frac{\partial}{\partial x} (\frac{1}{h} \int_{-h}^0 -\frac{1}{\rho_0} \frac{\partial p}{\partial y} dz) - \frac{\partial}{\partial y} (\frac{1}{h} \int_{-h}^0 -\frac{1}{\rho_0} \frac{\partial p}{\partial x} dz) = J(\int_{-h}^0 \frac{\rho g z}{\rho_0} dz, 1/h)$$

## Reference

- Bisagni, J.J., H.-S. Kim, and A. Chaudhuri, Interannual variability of the shelf-slope front position between 75 and 50 W, *Journal of Marine Systems*, 78, 337-350, 2009.
- Broquet, G., C.A. Edwards, A.M. Moore, B.S. Powell, M. Veneziani, and J.D. Doyle, Application of 4D-Variational data assimilation to the California Current System, *Dynamics of Atmospheres and Oceans*, 48, 69-92, 2009.
- Broquet, G., A.M. Moore, H.G. Arango, and C.A. Edwards, Corrections to ocean surface forcing in the California Current System using 4D variational data assimilation, *Ocean Modeling*, 36, 116-132, 2011.
- Cane, M.A., V.M. Kamenkovich, and A. Krupitsky, On the Utility and Disutility of JEBAR, *Journal of Physical Oceanography*, 28, 519-526, 1997.
- Chapman, D.C., Numerical treatment of cross-shelf open boundaries in a barotropic coastal ocean model, *Journal of Physical Oceanography*, 15 (8), 1060-1075, 1985.
- Chapman, D.C., and K.H. Brink, Shelf and Slope Circulation Induced by Fluctuating Offshore Forcing, *Journal of Geophysical Research*, 92 (C11), 11,741-11,759, 1987.
- Chen, K., and R. He, Numerical Investigation of the Middle Atlantic Bight Shelfbreak Frontal Circulation Using a High-Resolution Ocean Hindcast Model, *Journal of Physical Oceanography*, 40, 949-964, 2010.
- Churchill, J.H., P.C. Cornillon, and G.W. Milkowski, A Cyclonic Eddy and Shelf-Slope Exchange Associated With a Gulf Stream Warm-Core Ring, *Journal of Geophysical Research*, 91 (C8), 9615-9623, 1986.
- Csanady, G.T., and P. Hamilton, Circulation of the slope water, *Continental Shelf Research*, 8 (565-624), 1988.
- Fisher, A., Entrainment of shelf water by the Gulf Stream northeast of Cape Hatteras, *Journal of Computational Physics*, 77, 3248-3255, 1972.
- Flather, R.A., A tidal model of the northwest European continental shelf, *Mem. Soc. R. Sci. Liege*, 6 (10), 141-164, 1976.
- Ford, W., J. Longard, and R. Banks, On the nature, occurrence and origin of cold, low salinity water along the edge of the Gulf Stream, *Journal of Marine Research*, 11, 281-293, 1952.
- Frantantoni, P.S., R.S. Pickart, D.J. Torres, and A. Scotti, Mean Structure and Dynamics of the Shelfbreak Jet in the Middle Atlantic Bight during Fall and Winter, *Journal of Physical Oceanography*, 31, 2135-2156, 2001.
- Frolov, S.A., G.G. Sutyrin, G.D. Rowe, and L.M. Rothstein, Loop Current Eddy interaction with the Western Boundary in the Gulf of Mexico, *Journal of Physical Oceanography*, 34, 2223-2237, 2004.

- Garfield, N., and D.L. Evans, Shelf Water Entrainment by Gulf Stream Warm-Core Rings, *Journal of Geophysical Research*, 92 (C12), 13,003-13,012, 1987.
- Garvine, R.W., K.-C. Wong, and G.G. Gawarkiewicz, Quantitative properties of shelfbreak eddies, *Journal of Geophysical Research*, 94, 14,475-14,483, 1989.
- Gawarkiewicz, G., T. Fredelman, T. Church, and G. Luther, Shelfbreak frontal structure on the continental shelf north of Cape Hatteras, *Continental Shelf Research*, 16, 1751-1773, 1996.
- Gawarkiewicz, G., F. Bahr, R.C. Beardsley, and K.H. Brink, Interaction of a Slope Eddy with the Shelfbreak Front in the Middle Atlantic Bight, *Journal of Physical Oceanography*, 31, 2783-2796, 2001.
- Guo, X., H. Hukuda, Y. Miyazawa, and T. Ymagata, A Triply Nested Ocean Model for Simulating the Kuroshio - Roles of Horizontal Resolution on JEBAR, *Journal of Physical Oceanography*, 33, 145-169, 2001.
- Haidvogel, D.B., H. Arango, W.P. Budgell, B.D. Cornuelle, E. Curchitser, E.D. Lorenzo, K. Fennel, W.R. Geyer, A.J. Hermann, L. Lanerolle, J. Levin, J.C. McWilliams, A.J. Miller, A.M. Moore, T.M. Powell, A.F. Shchepetkin, C.R. Sherwood, R.P. Signell, J.C. Warner, and J. Wilkin, Ocean forecasting in terrain-following coordinates: Formulation and skill assessment of the Regional Ocean Modeling System, *Journal of Computational Physics*, 227, 3595-3624, 2008.
- He, R., and R. Weisberg, A Loop Current Intrusion Case Study on the West Florida Shelf, *Journal of Physical Oceanography*, 33, 465-477, 2003.
- Houghton, R.W., D.B. Olson, and P.J. Celone, Observation of an Anticyclonic Eddy near the Continental Shelf Break South of New England, *Journal of Physical Oceanography*, 16, 60-71, 1985.
- Joyce, T.M., Velocity and Hydrographic Structure of a Gulf Stream Warm-Core Ring, *Journal of Physical Oceanography*, 14, 936-947, 1984.
- Joyce, T.M., J.K.B. Bishop, and O.B. Brown, Observation of offshore shelf-water transport induced by a warm-core ring, *Deep-Sea Research*, 39, S97-S113, 1992.
- Linder, C., and G. Gawarkiewicz, A climatology of the shelf-break front in the Middle Atlantic Bight, *Journal of Geophysical Research*, 103, 18,405-18,423, 1998.
- Lorenzo, E.D., A. Moore, H. Arango, Chua, B.D. Cornuelle, A.J. Miller, B. Powell, and A. Bennett, Weak and strong constraint data assimilation in the inverse Regional Ocean Modeling System (ROMS): development and application for a baroclinic coastal upwelling system, *Ocean Modeling*, 16 (3-4), 160-187, 2007.
- Mellor, G.L., and T. Yamada, Development of a Turbulence Closure Model for Geophysical Fluid Problems, *Reviews of Geophysics and Space Physics*, 20 (4), 851-875, 1982.
- Mertz, G., and D.G. Wright, Interpretation of the JEBAR Term, *Journal of Physical Oceanography*, 22, 301-305, 1992.

- Mizobata, K., J. Wang, and S.-i. Saitoh, Eddy- induced cross-slope exchange maintaining summer high productivity of the Bering Sea shelf break, *Journal of Geophysical Research*, 111 (C10017), doi: 10.1029/2005JC003335, 2006.
- Moore, A.M., H.G. Arango, G. Broquet, B. Powell, A.T. Weaver, and J. Zavala-Garay, The Regional Ocean Modeling System (ROMS) 4-Dimensional Variational Data Assimilation Systems: part1 - System overview and formulation, 2011.
- Morgan, C.W., and J.M. Bishop, An Example of Gulf Stream Eddy-Induced Water Exchange in the Mid-Atlantic Bight, *Journal of Physical Oceanography*, 7, 472-479, 1977.
- Oey, L.-Y., Eddy- and wind-forced shelf circulation, *Journal of Geophysical Research*, 100 (C5), 8621-8637, 1995.
- Pickart, R.S., D.J. Torres, T.K. McKee, M.J. Caruso, and J.E. Przystup, Diagnosing a meander of the shelf break current in the Middle Atlantic Bight, *Journal of Geophysical Research*, 104 (C2), 3121-3132, 1999.
- Powell, B.S., H. Arango, A.M. Moore, E.D. Lorenzo, and D.F. R.F. Milliff, 4DVAR Data Assimilation in the Intra-Americas Sea with the Regional Ocean Modeling System (ROMS), *Ocean Modeling*, 25, 173-188, 2008.
- Powell, B.S., A.M. Moore, H.G. Arango, E.D. Lorenzo, R.F. Milliff, and R.R. Leben, Near real-time ocean circulation assimilation and prediction in the Intra-Americas Sea with ROMS, *Dynamics of Atmospheres and Oceans*, 48, 46-68, 2009.
- Ramp, S.R., R.C. Beardsley, and R. Legeckis, An Observation of Frontal Wave Development on a Shelf-Slope/Warm Core Ring Front Near the Shelf Break South of New England, *Journal of Physical Oceanography*, 13, 907-912, 1983.
- Sarkisyan, A.S., Forty Years of JEBAR - the Finding of the Joint Effect of Baroclinicity and Bottom Relief for the Modeling of Ocean Climatic Characteristics, *Izvestiya Atmospheric and Oceanic Physics*, 42 (5), 534-554, 2006.
- Shchepetkin, A.F., and J.C. McWilliams, A method for computing horizontal pressure-gradient force in an oceanic model with a nonaligned vertical coordinate, *Journal of Geophysical Research*, 108 (C3), doi:10.1029/2001JC001047., 2003.
- Shchepetkin, A.F., and J.C. McWilliams, The regional oceanic modeling system (ROMS): a split-explicit, free surface, topography-following-coordinate oceanic model, *Ocean Modeling*, 9, 347-404, 2005.
- Tintore, J., D.-P. Wang, and P.E.L. Violette, Eddies and Thermohaline Intrusions of the Shelf/Slope Front off the Northeast Spanish Coast, *Journal of Geophysical Research*, 95 (C2), 1627-1633, 1990.
- Wang, X., Interaction of an eddy with a continental slope, MIT, 1992.

Wei, J., and D.-P. Wang, A three-dimensional model study of warm core ring interaction with continental shelf and slope, *Continental Shelf Research*, 29, 1635-1642, 2009.

## Figures

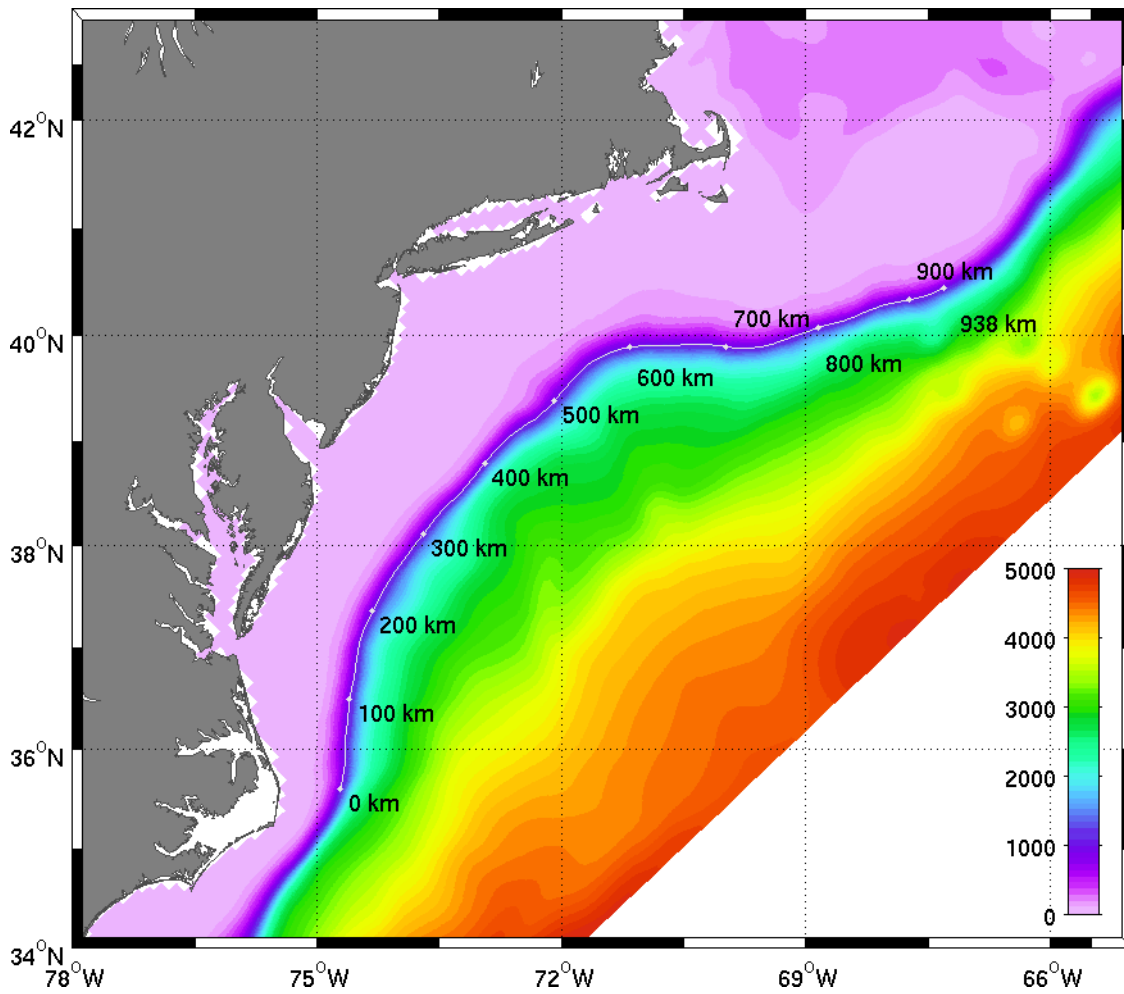


Figure 1. Mid Atlantic Bight and Gulf of Maine model domain. The bathymetry of this region is shown in color. 1000m isobath along which the cross-shelf transport and fluxes are calculated is shown in white curve. The relative along-isobath distance with respect to the starting point are also labeled.

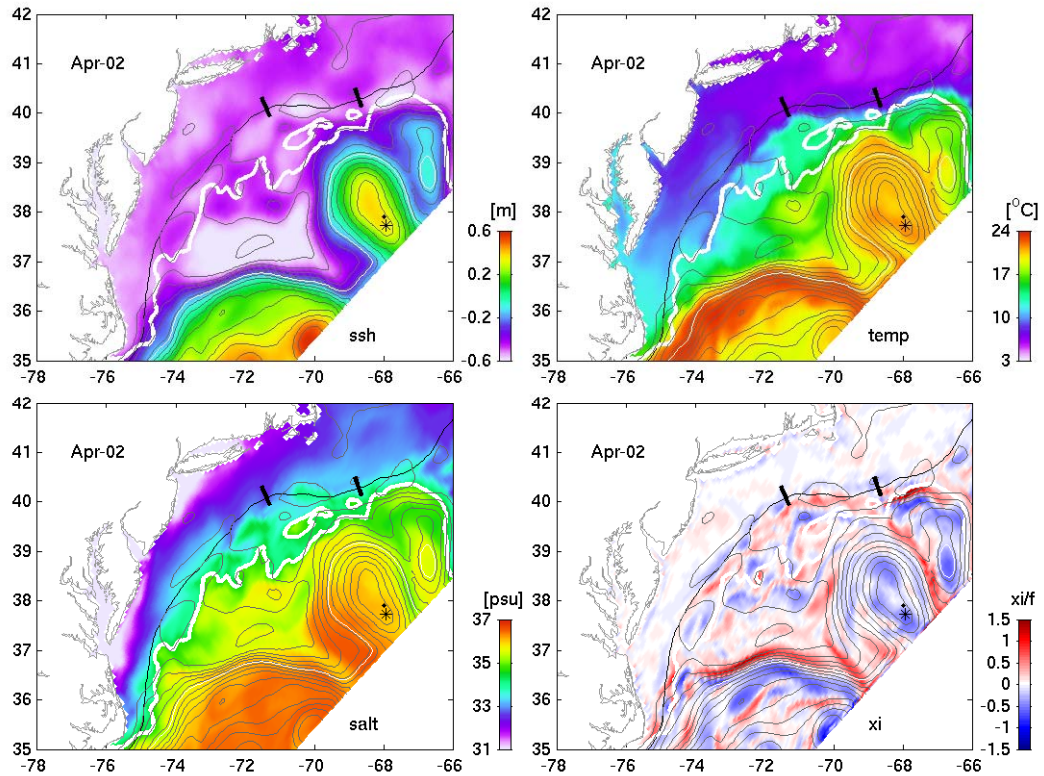


Figure 2. Surface height, surface temperature, surface salinity and surface vorticity on April 2<sup>nd</sup>, 2006. Also shown are streamfunction contours (gray) and e-folding value (thin white contour) of maximum streamfunction. The center of the meander/ring is shown by black star while its track is shown every 3 day in black dots. The thick white curve is isohaline 34.5 and the thin black curve is 200m isobaths. Two cross-shelf transects are depicted in black line segment.

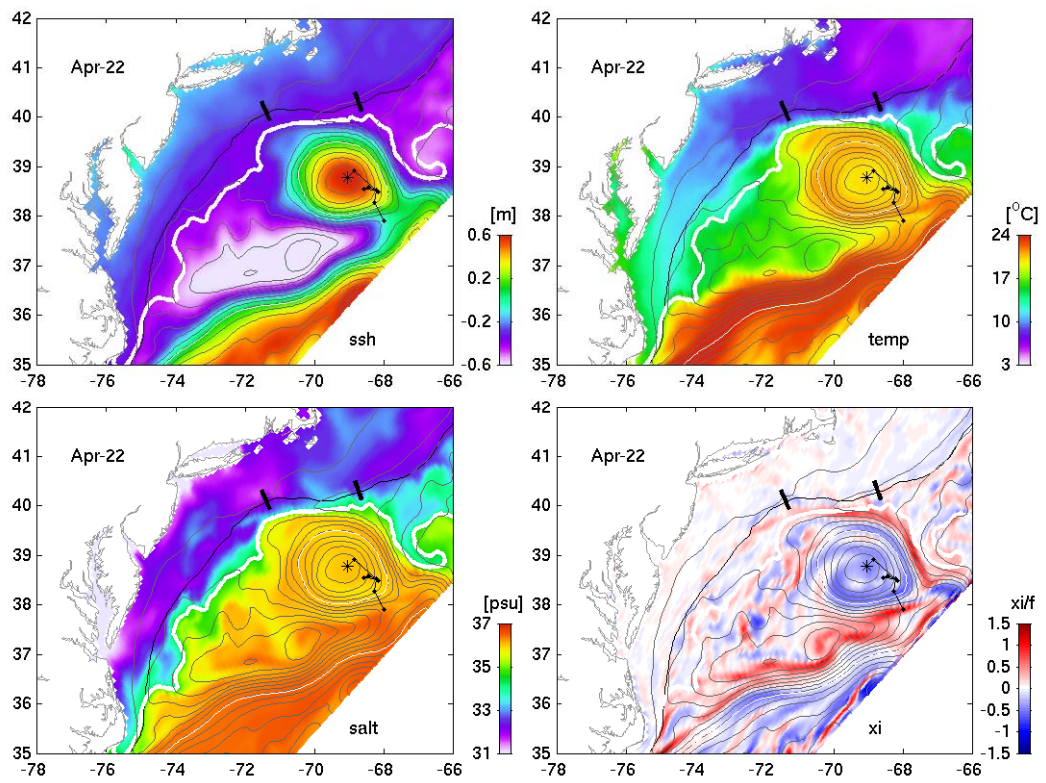


Figure 3. Same as figure 2 but on April 22<sup>nd</sup>, 2006.

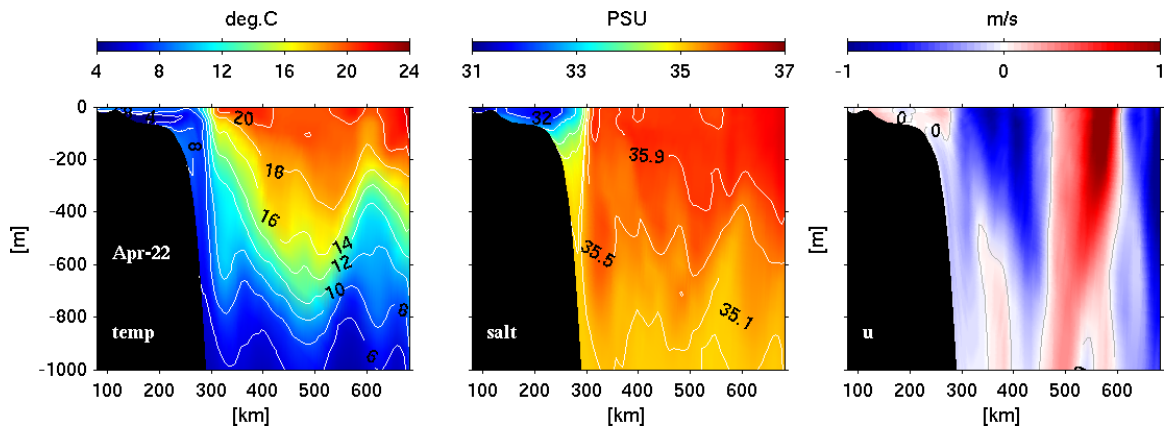


Figure 4. Cross-section view of temperature, salinity and velocity along cross-shelf directional transect at the center of WCR on April 22<sup>nd</sup>, 2006.

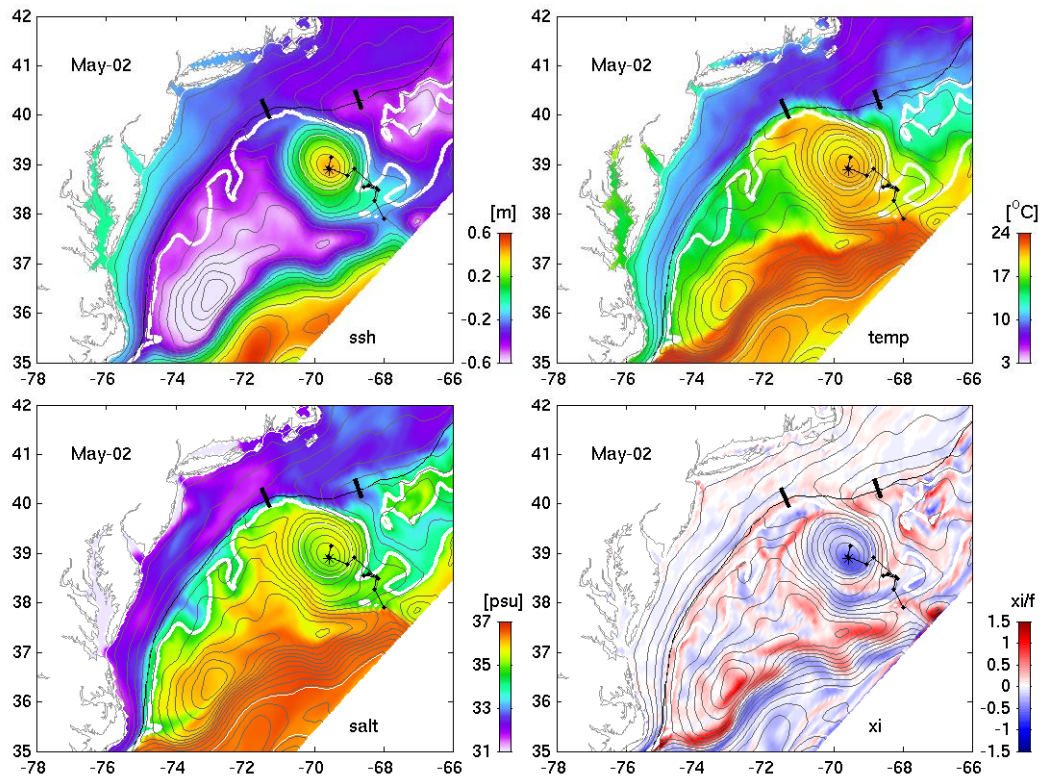


Figure 5. Same as figure 2 but on May 2<sup>nd</sup>, 2006.

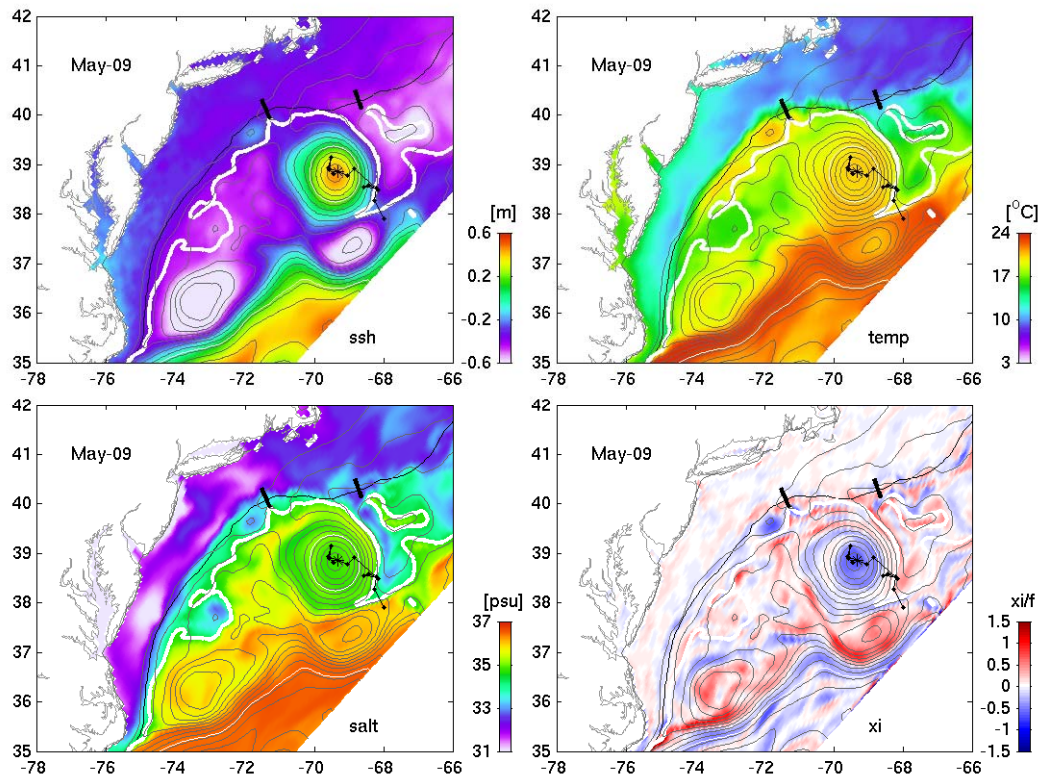


Figure 6. Same as figure 2 but on May 9<sup>th</sup>, 2006.

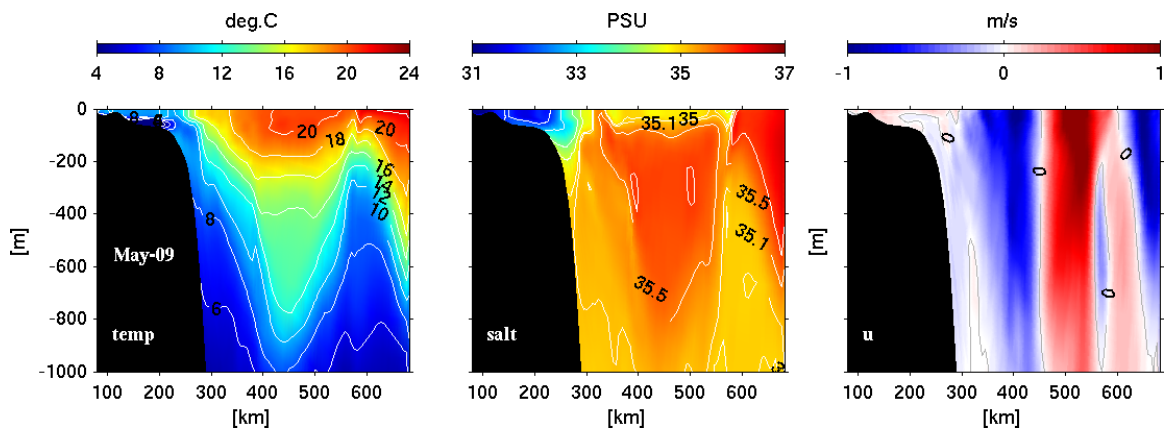


Figure 7. Same as figure 4 but on May 9<sup>th</sup>, 2006

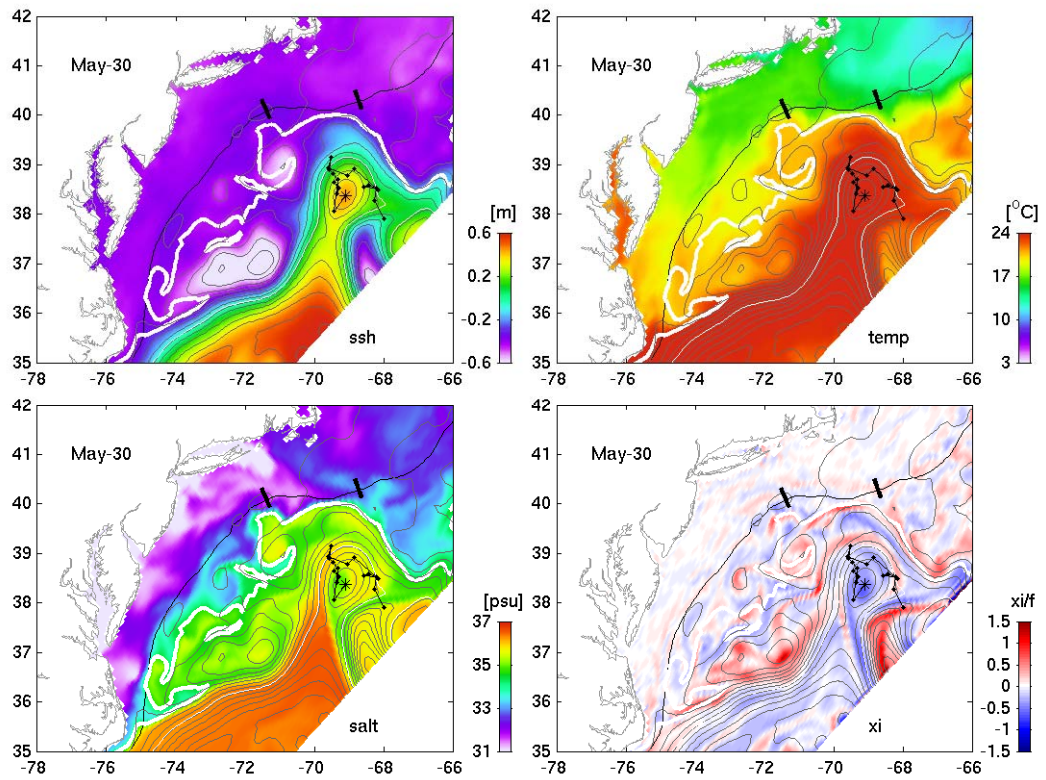


Figure 8. Same as figure 2 but on May 30<sup>th</sup>, 2006.

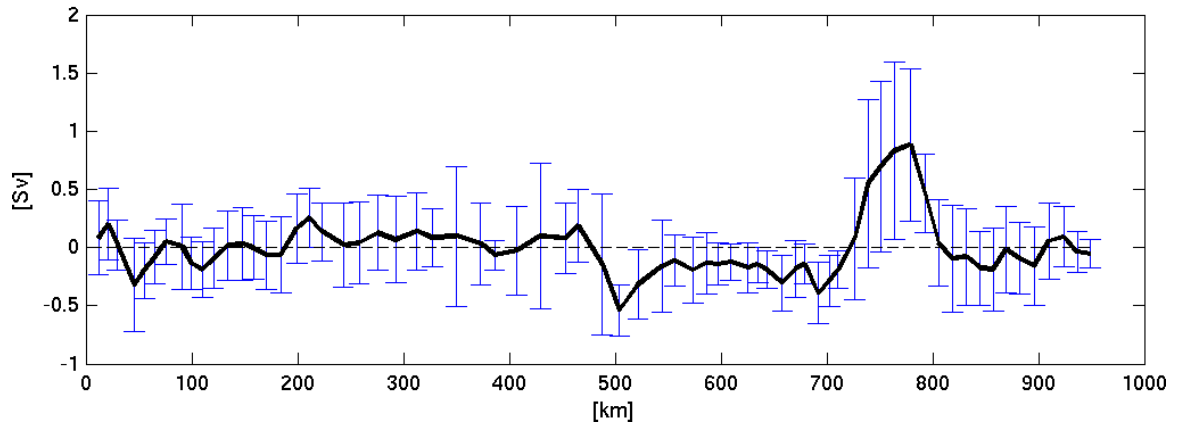


Figure 9. cross-shelf volume transport along 1000m isoabth. Mean values (April 22<sup>nd</sup> to May 18<sup>th</sup>) are shown in solid black curve while standard deviation are shown in blue. Negative values stand for onshore transport while positive values stand for offshore transport.

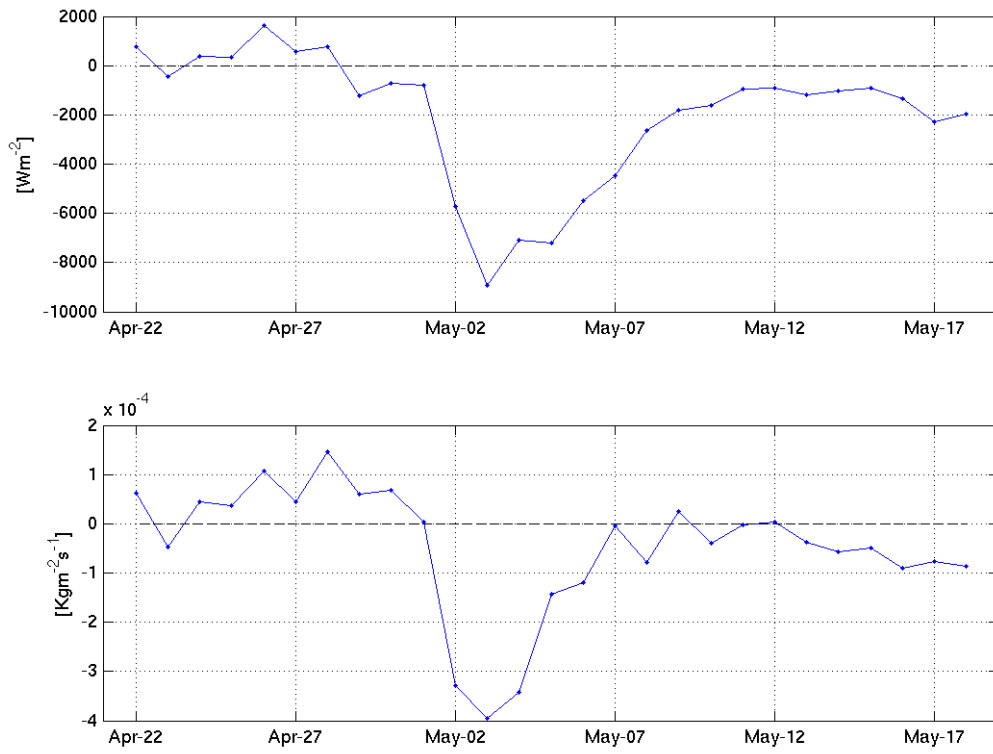


Figure 10. Cross-shelf eddy heat/salt fluxes during WCR period.

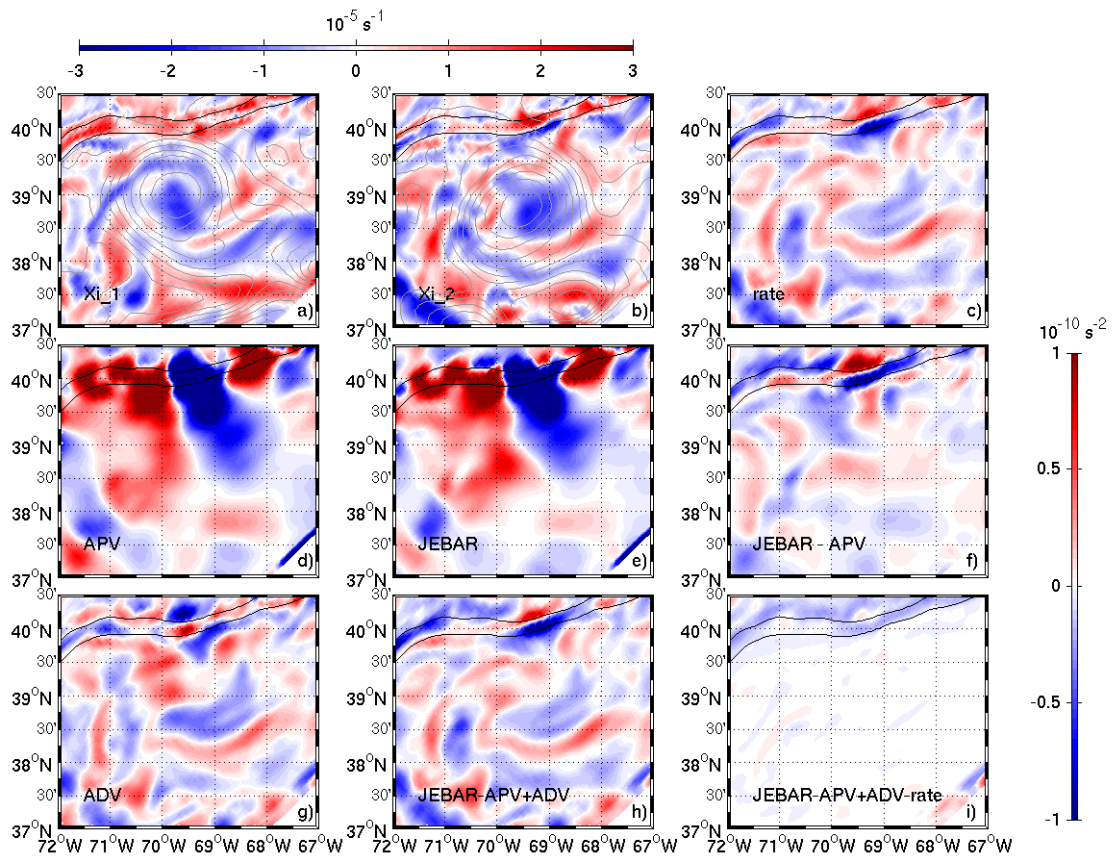


Figure 11. Depth averaged relative vorticity and its source and sink terms during the WCR impinging period. (a) and (b) Depth averaged relative vorticity on May 1<sup>st</sup> and May 7<sup>th</sup> 2006, respectively, with horizontal colorbar. Sea surface height are shown in gray contours. (c) Time rate change of depth averaged relative vorticity (rate). (d) Advection of potential vorticity (APV). (e) Joint Effect of Baroclinicity and Bottom Relief (JEBAR). (f) Residual of JEBAR and APV. (g) Nonlinear advection of relative vorticity (ADV). (h) Total effect of JEBAR, APV and ADV. (i) Residual of JEBAR, APV, ADV and rate terms. All source and sink terms are scaled with the vertical colorbar. In each panel, the 200m and 1000m isobaths are shown in black curves.

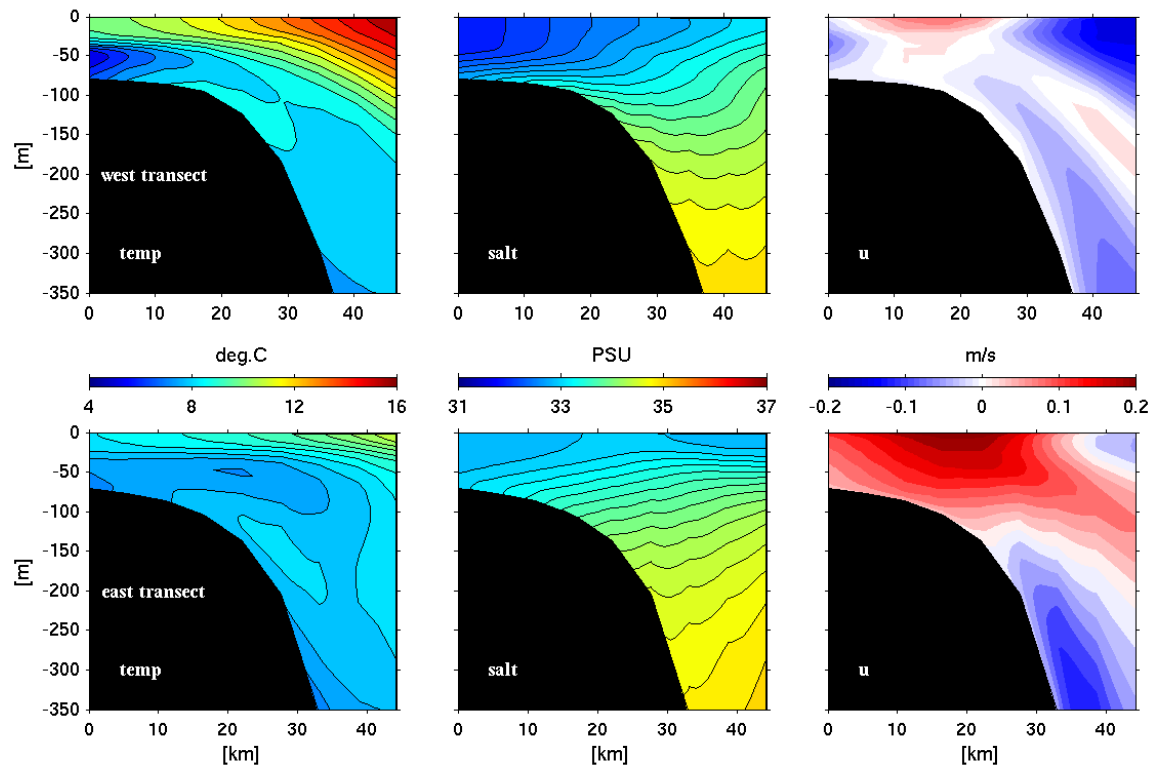


Figure 12. Cross-section view of mean temperature, salinity, along-shelf velocity along west transect and east transect from April 22<sup>nd</sup> to May 18<sup>th</sup>.

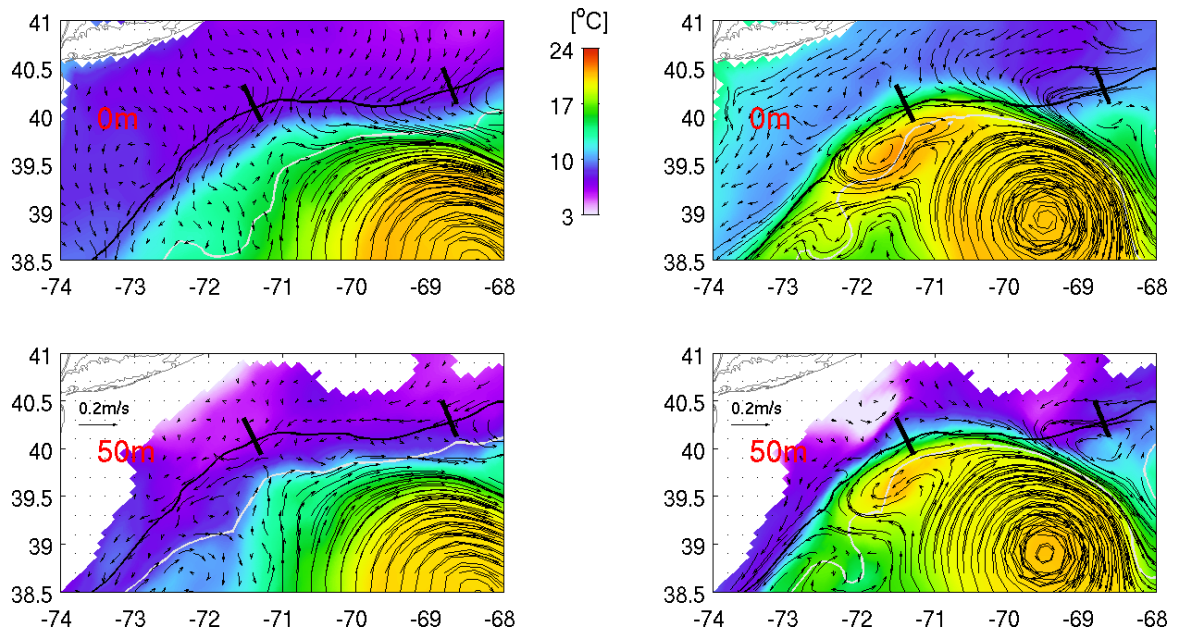


Figure 13. Mean temperature and velocity before WCR impingement (April 1<sup>st</sup> to 20<sup>th</sup>, left column) and during WCR impingement (May 1<sup>st</sup> to 7<sup>th</sup>, right column). Surface fields are shown in the first row while subsurface (50m) fields are shown in the second row. Locations of two transects in Figure 12 are also shown.

## CHAPTER 6: SUMMARY AND CONCLUSIONS

This work extensively investigated the circulation dynamics and biophysical processes at the MAB shelfbreak region by utilizing state-of-art numerical modeling techniques. Different from earlier observational studies, which are limited by available data and their spatio-temporal resolution, this work broadens the understanding of this important coastal system based on time- and space-continuous model results.

In chapter two, a 1-km resolution regional circulation model was developed to hindcast the MAB shelfbreak circulation from December 2003 to June 2008. The model considered realistic atmospheric and tidal forcing. Its subtidal open boundary conditions were specified via one-way nesting with an existing shelf-wide MABGOM circulation simulation by *He and Chen*, (submitted). Hindcast solutions were compared with satellite altimeter data, hydrographic climatology for the MAB shelfbreak, and observational based decorrelation scale estimations. General agreements were found, indicating this shelfbreak circulation model is capable of capturing essential dynamics of the MAB shelfbreak circulation. As we focused on the mean structures of the shelfbreak current and hydrography in this study, time and space continuous circulation hindcast fields from January, 2004 to December 2007 were used to construct the temporal means and bimonthly averages of shelfbreak ocean states.

Our analysis showed that the MAB shelfbreak jet is a year-around, surface intensified flow. On the average, it has characteristic width and trapping depth of 40 km and 100 m, respectively, transporting ca. 0.4 Sv equatorward. The jet reaches its maximum speed ( $0.3 \text{ ms}^{-1}$ ) in the spring, when the shelfbreak temperature and salinity fronts fully develop. Throughout the year, the foot of the shelfbreak front migrates between 80m to 150m isobaths, reaching its farthest offshore (onshore) position in April and May (November and December). The accumulated theta change (ATC) calculation within shelfbreak isopycnals suggests the bottom boundary layer detachment is most significant during winter and spring seasons. The relative vorticity analysis indicates the larger velocity shear exists seaward of the shelfbreak, and that the vorticity ratio is roughly 2:1 between the seaward portion and shoreward portion of the shelfbreak current.

Geostrophy dominates the momentum balance of the shelfbreak jet. The viscosity in the boundary layers, along with the nonlinear advection in the interior play important roles in determining the ageostrophic flow. The cross-shelf volume transport, and its associated eddy heat and salt fluxes were estimated along the 200 m isobath within the model domain. These values are characterized by small means with large standard deviations, suggesting the shelf/slope exchanges across the MAB shelfbreak are highly variable. Indeed, the EOF analysis of the velocity fields along the Nantucket transect indicates that while the shelfbreak jet is the dominant mode, the structure and intensity of the current are subject to complex interactions between stratification, wind forcing, baroclinic instabilities and eddies.

In chapter three, a size-structured ecosystem model was coupled with the high resolution shelfbreak circulation model. The shelfbreak coupled biophysical model was used to hindcast the MAB shelfbreak circulation and ecosystem variations from December 2003 to November 2007. Favorable comparisons with MODIS-AQUA chlorophyll observations indicate that the coupled model can resolve the physical and biological dynamics at the MAB shelfbreak front. Time and space continuous hindcast fields from January 2004 to November 2007 were then used to investigate the seasonal and interannual characteristics of the MAB shelfbreak frontal circulation and ecosystem variability.

Consistent with previous studies our model hindcast and EOF analysis suggest that there is a biomass enhancement at the shelfbreak. Region-wide upper water column nutrient content peaks in late winter and early spring. The phytoplankton spring bloom starts 1 - 2 months later, followed by a zooplankton bloom in early summer. Increased mixing in the fall season allows subsurface nutrient injection to the euphotic zone, stimulating a second but smaller phytoplankton bloom and subsequent zooplankton bloom.

Focusing on the early spring season (Feb-Apr), our analysis shows strong interannual variability of nutrient supply at the MAB shelfbreak. Specifically, the spring of 2004 and 2005 were relatively nutrient-rich, whereas the spring of 2006 and 2007 were relatively nutrient-poor. The cause for this feature has both atmospheric and oceanic

origins. On one hand, stronger local wind mixing in winter and spring of 2004 and 2005 deepened the oceanic mixed layer depth up to 100 m, making more deep-ocean nutrient available to the upper water column. On the other hand, the shelfbreak jet was stronger in spring 2004 and 2005, allowing more effective alongshore advection of nutrients from upstream. In addition to surface mixing and horizontal advection, vertical advection associated with the shelfbreak bottom boundary layer (BBL) convergence is another contributing factor for the upper water column nutrient content. This is confirmed by significant positive temporal correlation between the BBL convergence ( $\nabla \cdot \vec{V}_{bottom}$ ) and upper ocean nutrient content.

Nutrient budget diagnostics for spring 2004 and 2007 along the Nantucket transect highlighted not only complex vertical structures of various dynamical terms (processes), but also significant variations in magnitude between the two years. Because nutrient advection ( $-u \partial N / \partial x - v \partial N / \partial y - w \partial N / \partial z$ ) is affected by interannual variability in both nutrient concentration ( $N$ ) and shelfbreak current ( $u, v, w$ ), it is difficult to distinguish the two effects in the present study. In the future, an idealized modeling investigation using the same nutrient background state ( $N$ ) will be pursued to further quantify the relative contributions of shelfbreak jet ( $u$ ) and local shelfbreak upwelling ( $w$ ) to the variation of shelfbreak nutrient content.

In chapter four and five, in order to investigate the impact of WCR on the shelf and shelfbreak circulation, IS4DVAR data assimilation is applied. The model skill was significantly refined via data assimilation. SSH over the entire assimilation period was improved by 79%. The previous RMSE with forward model was 0.28m and decreased to 0.06m (the value of SSH observational error) after data assimilation. SST was improved by 65%, with RMSE reduced from 1.90°C to 0.68°C. The DA posterior can resolve the Gulf Stream meander and WCR more accurately in both location and intensity. Subsurface fields which are of great importance for the purpose of our study have also been improved.

The comparison of independent ECOMON data that were not assimilated into the model demonstrates good extrapolation skill of the model. The overall temperature RMSE between forward model and ECOMON observation was 1.52°C and then was

reduced to  $0.59^{\circ}\text{C}$  after data assimilation, a 62% reduction. The salinity RMSE was reduced from 0.3psu to 0.13psu, by 57%. Based on the information from observational space, model dynamics was able to adjust remote portion of circulation.

Having a life span of approximately 26 days, the WCR in this study detached from closed Gulf Stream meander on April 22<sup>nd</sup>, 2006 and re-attach Gulf on May 18<sup>th</sup>, 2006. The initial radius and depth of the WCR are estimated as 96km and 1000m. The WCR headed to the continental shelf and made contact in early May. The impinging of WCR upon the shelfbreak lasted about one week and induced dramatic exchange between the shelf and slope. Mean cross-shelf transport is estimated to be 0.28 Sv during the impinging period while the instantaneous streamer transport is as large as 2.1 Sv. The maximum heat/salt flux is  $-8900 \text{ Watt m}^{-2} / -4 \times 10^{-4} \text{ Kg m}^{-2} \text{ s}^{-1}$ , on May 3<sup>rd</sup>, 2006, indicating strong entrainment of cold/fresh shelf water offshore. During the evolution and spin-down of the WCR, the radius and intensity were reduced. The advection of potential vorticity and joint effect of baroclinicity and bottom relief are the two largest terms while the variation of relative vorticity of the WCR is largely controlled by nonlinear advection effect.

The MAB shelfbreak is a dynamic environment that has highly variable along- and cross-shelf transport. In particular, one single large WCR could completely change the annual mean cross-shelf transport of mass, heat and salt. Understanding and predicting MAB shelf/slope exchange processes have to resolve both local and deep ocean impacts. Furthermore, deterministic predictions of shelf/slope circulation processes and biogeochemical couplings clearly requires further refinements of ocean models, advanced observational infrastructure together with sophisticated techniques for data assimilation. In this regard, the emerging MAB shelfbreak Pioneer Array (as a part of Ocean Observatory Initiative of NSF) and new in-situ observations it is about to collect are most valuable and exciting.